DARK MATTER IN THE HEAVENS AND AT COLLIDERS: MODELS AND CONSTRAINTS

Reinard Primulando

Samarinda, Indonesia

Master of Science, College of William and Mary, 2009
Bachelor of Science, Institut Teknologi Bandung, 2006

A Dissertation presented to the Graduate Faculty
of the College of William and Mary in Candidacy for the Degree of
Doctor of Philosophy

Department of Physics

The College of William and Mary
August 2012

APPROVAL PAGE

This Dissertation is submitted in partial fulfillment of
the requirements for the degree of

Doctor of Philosophy

Reinard Primulando

Approved by the Committee, April, 2012

Committee Chair
Professor Christopher Carone, Physics
The College of William and Mary

Associate Professor Joshua Erlich, Physics
The College of William and Mary

Professor Marc Sher, Physics
The College of William and Mary

Assistant Professor Patricia Vahle, Physics
The College of William and Mary

Dr. Patrick J. Fox
Fermi National Accelerator Laboratory

ABSTRACT PAGE

In this dissertation, we investigate various aspects of dark matter detection and model building. Motivated by the cosmic ray positron excess observed by PAMELA, we construct models of decaying dark matter to explain the excess. Specifically we present an explicit, TeV-scale model of decaying dark matter in which the approximate stability of the dark matter candidate is a consequence of a global symmetry that is broken only by instanton-induced operators generated by a non-Abelian dark gauge group. Alternatively, the decaying operator can arise as a Planck suppressed correction in a model with an Abelian discrete symmetry and vector-like states at an intermediate scale that are responsible for generating lepton Yukawa couplings. A flavor-nonconserving dark matter decay is also considered in the case of fermionic dark matter. Assuming a general Dirac structure for the four-fermion contact interactions of interest, the cosmic-ray electron and positron spectra were studied. We show that good fits to the current data can be obtained for both charged-lepton-flavor-conserving and flavor-violating decay channels. Motivated by a possible excess of gamma rays in the galactic center, we constructed a supersymmetric leptophilic higgs model to explain the excess. Finally, we consider an improvement on dark matter collider searches using the Razor analysis, which was originally utilized for supersymmetry searches by the CMS collaboration.

TABLE OF CONTENTS

DEDICATION

I present this thesis in honor of my parents.

ACKNOWLEDGMENTS

First and foremost I offer my sincerest gratitude to my advisor, Prof. Chris Carone, who has supported me throughout my time in graduate school with his patience and knowledge.

I would also like to thank members of the High Energy Theory Group: Prof. Josh Erlich and Prof. Marc Sher for many fruitful discussions and exciting collaborations.

Special thanks to members of the Fermilab Theory Group, especially my fellowship supervisor, Patrick Fox, and other collaborators: Roni Harnik, Chiu-Tien Yu, Wolfgang Altmannshofer and Felix Yu.

My graduate school experience would not have been so fun without having great roommates: Derrin, Jeremy and Bayu, doing all-nighters playing Pinochle and AOE with Doug, Dylan, Gardner, Matt and Meg, having parties organized by Nate and Kelly, and hanging out with my Indonesian friends: Mas Agus, Kak Wirawan, Kak Zainul, Yudhis, Adit and Rony.

Finally, I want to thank my parents, my sister and my brother for their unconditional love and support.

LIST OF TABLES

LIST OF FIGURES

DARK MATTER IN THE HEAVENS AND AT COLLIDERS: MODELS AND CONSTRAINTS

CHAPTER 1

Introduction

As the data from cosmological observations accumulates, we gain a better understanding on the composition of the universe. Interestingly, baryonic matter is responsible for only 5% of the universe's energy density. Other known particles, such as electrons, photons and neutrinos make negligible contributions to the energy density. The rest of the universe is made of the presently unknown components. Their existence is inferred only by their gravitational influence on the known matter. Presently, it is understood that 22% of the universe is dark matter (DM) while the rest, 73%, is dark energy, probably in the form of a cosmological constant. This thesis focuses on understanding the nature of the DM. Before proceeding, we will review the observational evidence for the existence of DM.

1.1 Observational Evidence of Dark Matter

The observational evidence for dark matter ranges from the galactic to the cosmological scale. The earliest evidence for DM on the galactic scale comes from the 1970 measurement of the rotational velocity of the Andromeda's galaxy by Rubin and Ford [30]. They measured the spectra of 67 H II regions at distance 3-24 kpc from the galaxy center and found that the rotational velocity of these H II regions, v, remain constant. This contradicts the expectation of Keplerian velocity, $v \propto 1/\sqrt{r}$, based on the observed mass distribution. In order to explain the discrepancy, the existence of a non-luminous dark matter halo with a mass density $\rho(r) \propto 1/r^2$ needs to be introduced. The current measurements of rotation curves of several galaxies establish a lower bound of dark matter density, $\Omega_{\rm DM} \gtrsim 0.1$ [5], where $\Omega \equiv \rho/\rho_c$. We define ρ_c as the density of a flat universe.

On the galactic cluster scale, one can use weak gravitational lensing to determine the mass of the cluster. Additionally, the temperature measurement of the hot intracluster medium provides another way to estimate the mass of galaxy clusters [31]. When the baryon system is in a hydrostatic equilibrium, the outward pressure of the system balances the inward gravity pressure influenced by both baryonic and dark matter. By measuring the X-ray temperature of hot intracluster gas, the cluster mass can be inferred. Just as in the case of the galactic mass measurement, the ratio of visible to total mass in galactic clusters is significantly smaller than unity. The obtained dark matter density from this observation is $\Omega_{\rm DM} \simeq 0.2$ [5].

Finally at the cosmological scale, the analysis of the Cosmic Microwave Background (CMB) can be used to pin down the baryonic and dark matter densities. In the early universe, when baryons and photons still interact strongly, many potential wells were created from quantum-fluctuation-generated density inhomogeneities. As the matter falls into the wells, the outward radiation pressure builds and the system undergoes acoustic oscillation. The oscillation is dictated by the amount of baryons, photons and dark matter inside the well. At the time of recombination, the photon decouples from the system and the density variation caused by the oscillation is imprinted in the CMB anisotropies. The presence of CMB anisotropies have been detected by various experiments and investigated in a great detail by WMAP satellite. Fig. 1.1 shows the 7-year WMAP results expanded in the multipoles of

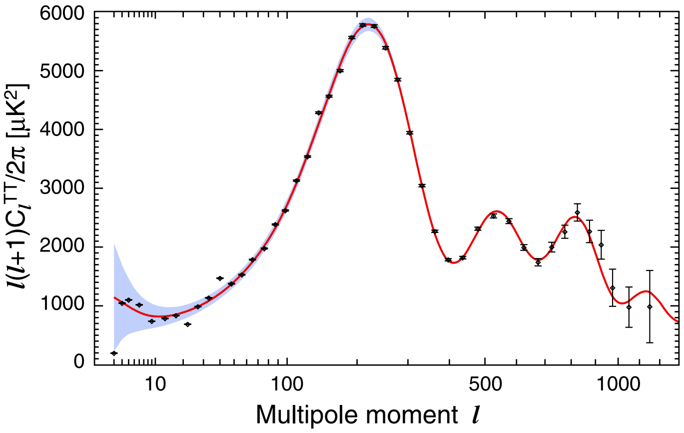

FIG. 1.1: The CMB anisotropies from WMAP 7-year data [2]. C_l is the correlation function defined as $\langle \Theta_{lm}^* \Theta_{l'm'} \rangle = \delta_{ll'}\delta_{mm'}C_l$ where $\Theta_{lm} = \int \Theta(\hat{n}) Y_{lm}^*(\hat{n}) d\Omega$ and $\Theta(\hat{n})$ is the CMB temperature at the direction of $\hat{n}$.

CMB anisotropies l [2]. The solid line shows a prediction for $\Omega_{\text{baryon}} = 0.0450$, $\Omega_{\text{DM}} = 0.220$, $\Omega_\Lambda = 0.738$, where Λ denotes the cosmological constant/dark energy. The prediction agrees remarkably well with the WMAP data. This result clearly shows that the dark matter density dominates over the baryon density on the cosmological scales.

1.2 Thermal Production of Dark Matter

Since all the evidence for the existence of DM comes only from its gravitational interaction, the other properties of dark matter are still largely unknown. In this section, we will discuss possible scenarios for producing dark matter in the early universe to get some idea of the necessary interaction between DM and Standard Model (SM) particles.

DM can be produced thermally in the early universe while the temperature of the universe is above the scale of the DM mass. SM particles then have enough energy to produce the dark matter by the reaction $f\bar{f} \to \chi\bar{\chi}$, where f is a SM particle and χ is the dark matter. The reverse process can also happen and equilibrium between DM matter and SM particles can be maintained as long as the DM-SM interaction rate is large relative to the expansion rate of the universe and the available thermal energy is enough to create the DM pairs. When the temperature and interaction rate decreases, the DM and SM particles start to decouple. This situation is called freeze-out. After freeze-out, the dark matter abundance per comoving volume is unchanged until the present day.

Quantitatively, one could write down the abundance of the DM as a function of time to be [3]:

$$\frac{dn_\chi}{dt} + 3Hn_\chi = -\langle\sigma v\rangle[n_\chi^2 - (n_\chi^{eq})^2], \tag{1.1}$$

where n_χ is the DM number density, n_χ^{eq} is the DM equilibrium density, H is the Hubble parameter, $\langle\sigma v\rangle$ is the thermally average annihilation cross section for $\chi\,\bar{\chi} \;\rightarrow\; f\;\bar{f}$. Freeze out happens when

$$\langle\sigma v\rangle n_\chi^{eq} \approx H. \tag{1.2}$$

The solution of Eq. (1.1) is plotted in Fig. 1.2. One can see that the annihilation cross section determines the dark matter relic density. The dark matter with a bigger cross section decouples later which leads to a smaller relic density.

Assuming that $\langle\sigma v\rangle$ is independent of the temperature, once can approximate the current dark matter density to be

$$\Omega_\chi \sim \frac{4\times 10^{-10}}{\langle\sigma v\rangle\ \mathrm{GeV}^2}, \tag{1.3}$$

independent of the dark matter mass. The correct dark matter density $\Omega_\chi \sim 0.1$ can be achieved with an s-channel mediator of DM-SM interaction with a mass $\mathcal{O}(100\ \mathrm{GeV})$ and a coupling $g \sim \mathcal{O}(0.1)$. The mass scale for this interaction is remarkably close to the weak scale. This coincidence suggests a possibility of incor-

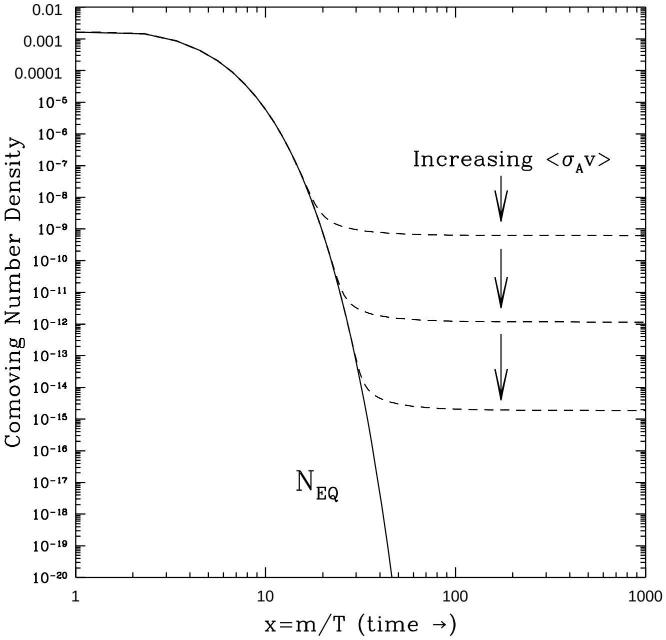

FIG. 1.2: The dark matter number density per comoving volume as a function of time. Figure taken from [3].

porating the DM into new physics at the weak scale. Some examples of weak scale models that includes a DM candidate in the particle spectrum are the Minimal Supersymmetric Standard Model (MSSM) [32], Universal Extra Dimension (UED) [33] and the Little Higgs model [34]. The possibility that DM is associated with new physics at the weak scale is known as Weakly Interaction Massive Particles (WIMP) scenario.

The WIMP scenario is not the only possible way to obtain the correct dark matter density. An alternative picture that has been explored recently is the asymmetric dark matter framework [35–38]. The relation of the current baryon and dark matter density is given by $\Omega_{\rm DM} \sim 5\,\Omega_{\rm baryon}$. The asymmetric dark matter framework offers an explanation for the relation by connecting the baryon asymmetry to an asymmetry in dark sector.

1.3 Dark Matter Detection

From the perspective of DM production in the early universe, there is a clear motivation for an interaction between the DM and SM sectors besides the gravitational interaction. This opens up possibilities of observing the DM in ways other than looking at its gravitational influence. The DM can be detected either directly or indirectly. It can also be produced in collider experiments. This section reviews these various methods for detecting or producing DM.

1.3.1 Direct Detection of Dark Matter

As the solar system circles around the galactic center, the Earth passes through the "wind" of the DM halo. Occasionally, the DM scatters off a target nuclei in an experiment located on the Earth. Based on the constructed nuclear-recoil energy and the scattering event rate, some properties of dark matter can be inferred. This method of detecting DM is called direct detection.

The typical recoil energy varies between ~ 1 to ~ 100 keV, depending on the DM and the target nucleus masses. In the standard WIMP scenario, the DM-nucleus interaction rate is about 1 event $\text{day}^{-1}\text{kg}^{-1}$. Given the low rate of DM-nucleon scattering, experimenters have to understand the backgrounds well in order to extract the DM signal.

The backgrounds for the direct detection of DM mainly come from cosmic ray muons and natural radioactivity from the surrounding materials. One could eliminate the cosmic ray muon background by locating the targets in deep underground laboratories and shielding them with materials with a muon veto capability, such as plastic scintillators. Radioactive beta and gamma ray background can be eliminated by shielding the target and vetoing the events that are most likely coming from electron recoils. A veto on multiple scattering also helps reduce backgrounds since it is expected that a weakly interacting DM particle will scatter in the target material at most once before exiting. Various experiments, such as CDMS-II and XENON100 are able to efficiently veto the background to obtain the best limits on the scattering cross section. Some other experiments, such as DAMA, are looking for an annual modulation of events. The DM-nucleon relative velocity varies annually as the Earth orbits the Sun. This annual velocity variation leads to an annual variation of the DM flux, and hence, the scattering events are modulated annually. Since the radioactive background is expected to be constant over the course of the year, an annual modulation of observed events might be a signal of DM scatterings off the target nuclei.

DM can interact with the target nucleon either through spin-independent interactions or spin-dependent interactions. For the spin-independent interactions and a typical momentum transfer between nuclei and DM, the DM interacts coherently with all nucleons inside the nuclei. Therefore target materials with bigger atomic mass number are preferred in detecting spin-independent interactions. In the spin-dependent case, the spins between paired nucleon cancel. Therefore target nuclei with unpaired protons or neutrons, such as ^{19}F and ^{131}Xe, are more desirable.

Assuming a spin-independent interaction, the exclusion regions in the $m_{\rm DM} - \sigma_{\rm SI}$ plane are shown in Fig. 1.3. Currently, the DAMA [22], CoGeNT [21] and CRESST [4] experiments have claimed to see some hints of dark matter signals with mass around 10 GeV. However, their preferred regions do not seem compatible with each other. Moreover, CDMS-II [10] and XENON100 [23] bounds severely exclude the favored signal regions. One should note that the bounds and the favored regions depends on the assumption of the dark matter halo distribution. Moreover, an $\mathcal{O}(10)$ GeV dark matter signal is near the detection threshold of the CDMS-II and XENON100 experiments, where background noise starts to dominate. Possible solutions to the tension between these results are reviewed in [39]. The spin dependent bounds is

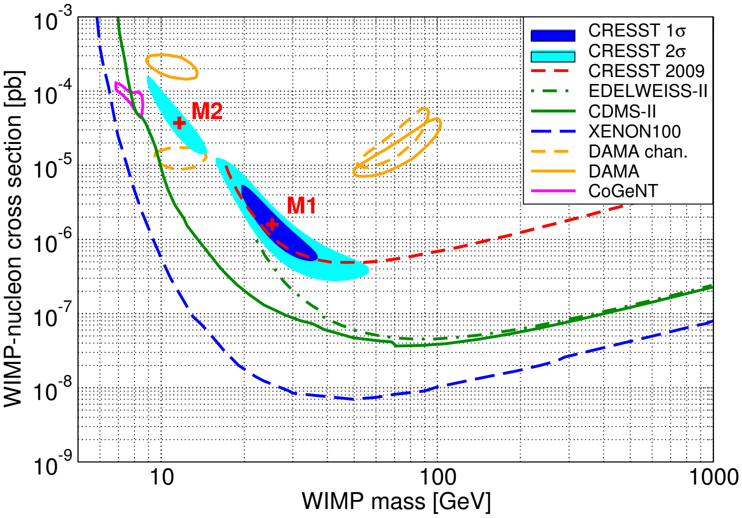

FIG. 1.3: The spin-independent exclusion by CDMS and XENON and the preferred region by CoGeNT, DAMA and CRESST in the $m_{\mathrm{DM}} - \sigma_{\mathrm{SI}}$ plane. Figure taken from [4].

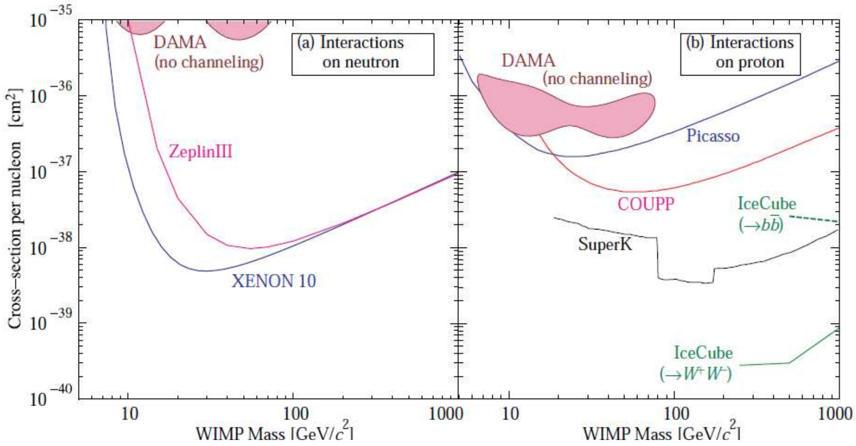

FIG. 1.4: The spin-dependent exclusion and DAMA preferred region. The figure taken from [5]

shown in Fig. 1.4. The DAMA annual modulation signals can be interpreted as DM spin-dependent scattering, and the favored region is shown in the figure. As in the case of a spin-independent interaction, the DAMA favored regions appear to be in conflict with other experimental results.

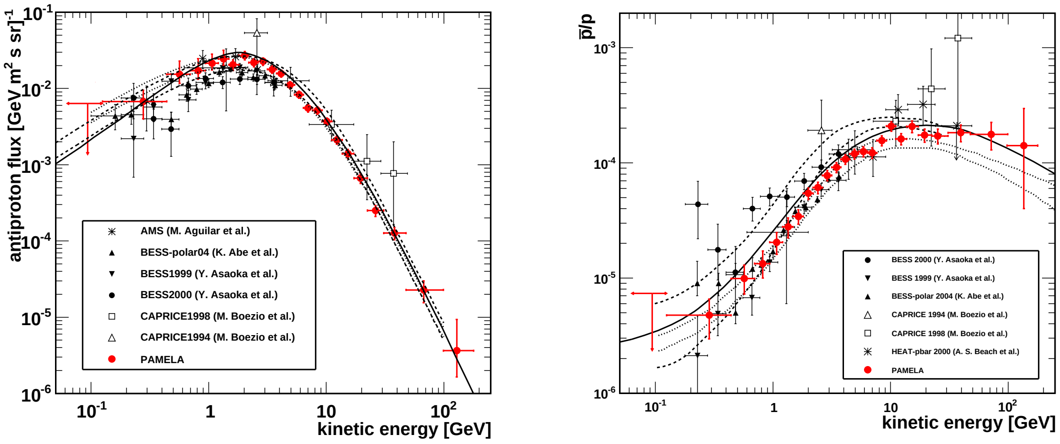

(a) (b)

FIG. 1.5: a) Cosmic ray antiprotons flux. b) Antiproton-proton fluxes ratio. Both figures are taken from Ref. [6]. The lines are various background predictions.

1.3.2 Indirect Detection of Dark Matter

Dark matter can also be detected indirectly by looking at the products of dark matter annihilations or decays in cosmic rays. Dark matter may annihilate or decay into various SM particles which become the components of the cosmic rays. Since cosmic rays propagation time is much longer than the lifetime of any unstable SM particle, the components that reach the earth mainly consist of secondary stable SM particles, such as electrons, positrons, nucleons and photons. Therefore, by looking for an excess of these particles over the expected astrophysical background, one could deduce the properties of the DM.

Various experiments have measured the cosmic-ray antiproton flux from 0.1 GeV to 100 GeV [6, 17, 40–43], shown in Fig. 1.5(a), and found no excess over the expected background. Moreover, the ratio of the antiproton to proton flux [6, 17, 40–42, 44] agrees well with the estimated background, as seen in Fig. 1.5(b).

The positron flux has also been measured by many experiments [7, 11–13]. In 2008, the PAMELA collaboration found an excess of the positron flux over the

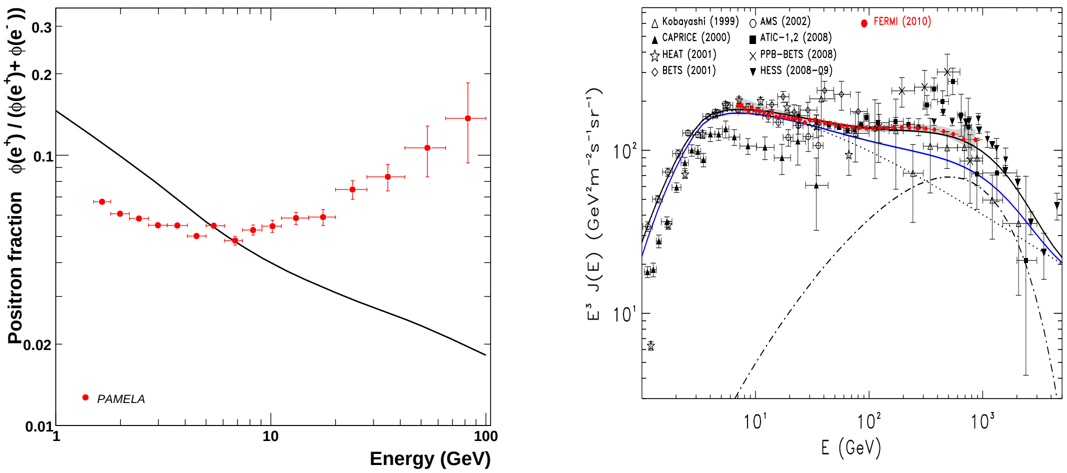

(a) (b)

FIG. 1.6: a) Cosmic ray positron flux taken from Ref. [7]. The solid line is the expected background. b) Electron and positron flux taken from Ref. [8]. The estimated background is given by the dotted line.

expected background from 7 GeV to 100 GeV [7]. Their observation is shown in Fig. 1.6(a). Their result was later confirmed by the Fermi-LAT collaboration [45]. The measurements of total electron and positron flux [8, 13–16, 43, 46–48], shown in Fig. 1.6(b), also shows and excess above background between 100 GeV and 1 TeV. A dark matter annihilation explanation of the excess requires $\langle \sigma v \rangle \sim 10^{-23}$ cm^3/s, $\mathcal{O}(10^3)$ larger than the thermal WIMP cross section. Therefore a standard WIMP annihilation scenario can not account for the anomaly. In order to explain the $\mathcal{O}(10^3)$ boost factor, some additional mechanisms need to be introduced, e.g., Sommerfeld enhancement [49] or Breit-Wigner enhancement [50]. Alternatively, the excess can be interpreted as dark matter decaying to leptons with a lifetime of $\mathcal{O}(10^{26})$ s [51]. One should also note that astrophysical sources, such as a nearby pulsar [52], have not been ruled out as the possible explanation of the excess.

Various observatories, such as EGRET, VERITAS, HESS and Fermi-LAT, are sensitive to cosmic gamma rays at the WIMP energy scale. In contrast to positrons or antiproton, gamma rays do not interact significantly with the galactic magnetic field. Therefore the direction of incoming gamma rays points out to their production source. Moreover, the photon energy is not significantly dissipated as in the case of charged particles. A signal from the region where the dark matter is expected to be denser such as the galactic center or satellite galaxies will provide an indication of the dark matter's presence. If photons are the primary products of dark matter annihilations, the photon spectrum would have be monoenergetic with the energy equal to the dark matter mass. The monoenergetic photons will show up as a sharp peak in the gamma ray spectrum over the continuous background. An observation of this peak would provide an indisputable signature of dark matter annihilations. However in the galactic center where the signal is expected to be strongest, the gamma ray emissions from the supermassive black hole Sgr A* potentially overwhelm the signal.

1.3.3 Collider Production

Dark matter production at colliders can provide a complementary way to search for DM. Unlike direct and indirect detection techniques that require uncertain astrophysical inputs, collider experiment paramaters, such as center of mass energy and beam luminosity, are accurately known. Additionally, colliders can probe smaller dark matter masses than direct detection experiments which are limited by their energy thresholds.

A simplified model of dark matter collider production was first introduced in Ref. [53]. In this model, one assume that the mediator for SM-DM interaction is heavier than the collider energy scale and can be integrated out leading to effective contact operators. This allows a more straightforward comparison between collider and direct detection bounds.

In order to be produced at a hadron collider, the DM has to couple to either quarks or gluons in the effective theory. In an electron-positron collider, such as LEP, a coupling to a positron-electron pair is required. Since the DM manifests itself as missing energy at colliders, the main signature at hadron colliders is initial state radiation jets or photons and missing transverse energy ($\not{E}_T$). The potential of obtaining a limit from the monojet + $\not{E}_T$ channel has been discussed in Refs. [54–56] for the Tevatron and in Refs. [20, 57] for the LHC. Very recently, dedicated searches in this channel have been performed by experimental groups both at the Tevatron and the LHC. In particular, the CDF collaboration has released their results from 6.7 fb^{-1} of data [58] and the CMS collaboration has presented their preliminary results for 4.7 fb^{-1} of their data [9]. A monophoton + $\not{E}_T$ dark matter signal is also present at hadron colliders for dark matter that interacts with quarks, however the cross section is lower by $\mathcal{O}(\alpha/\alpha_s)$ compared with the monojet + $\not{E}_T$ channel. A dedicated search was done by the CMS collaboration using 4.7 fb^{-1} of integrated luminosity [59]. The bound from LEP has been calculated in Refs. [60, 61]. In this case, monophoton + $\not{E}_T$ is the signature for the search.

For an illustration, the LHC results for monojet and monophoton + $\not{E}_T$ channels are shown in Fig. 1.7 for dark matter that couples to quarks [9]. For the spin-independent case, where the effective operator considered for the interaction is given by $\bar{q}\gamma^\mu q\, \bar{\chi}\gamma_\mu\chi$, the LHC has obtained a bound on light dark matter that is below the threshold of the direct detection experiments. The operator considered in the spin-dependent case is $\bar{q}\gamma^\mu\gamma^5 q\, \bar{\chi}\gamma_\mu\gamma^5\chi$. The cross section bounds coming from spin-dependent experiments is much weaker than the bounds from spin-independent experiments, because DM-nucleon spin-dependent scattering is not coherent over the whole nucleus. However, the LHC limit does not change significantly. The LHC provides the best bound for dark matter mass $\lesssim$ 1 TeV for the spin-dependent case.

This thesis explores new models for the origin of dark matter, including models that can explain the possible astrophysical indications of the existence of dark

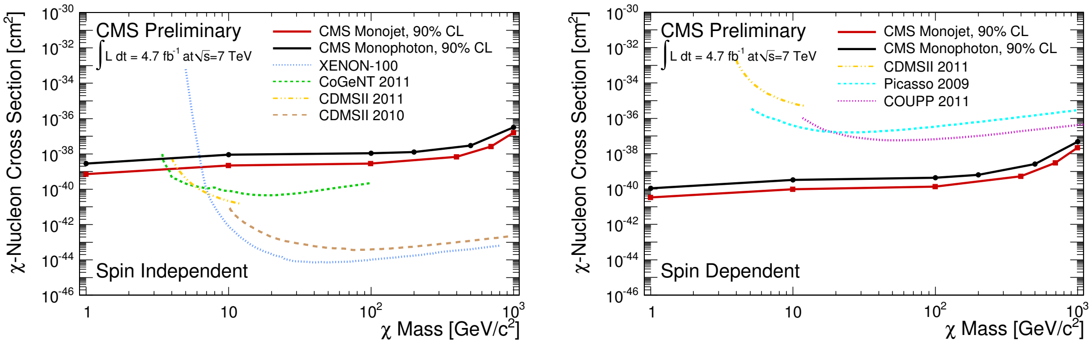

(a) spin-independent. (b) spin-dependent.

FIG. 1.7: Monojet and monophoton bounds on (a) spin-independent and (b) spin-dependent DM-nucleon scattering cross section. The figures are taken from [9].

matter. New analysis techniques for discovering dark matter at colliders is also presented. This thesis is organized as follows. The next two chapters are dedicated to constructing models of decaying dark matter. In particular, Chapter 2 discusses a model of decaying dark matter from dark instantons. In Chapter 3, a decaying dark matter model based on the Froggatt-Nielsen model is considered. Chapter 4 considers flavor-violating three-body dark matter decays. In Chapter 5, we discuss the explanation of a possible gamma ray excess at the galactic center in the supersymmetric leptophilic Higgs model framework. Finally, in Chapter 6, the possibility of improving the collider limits on dark matter production using the Razor analysis is considered.

CHAPTER 2

Decaying Dark Matter from Dark Instantons[1]

2.1 Introduction

Evidence has been accumulating for an electron and positron excess in cosmic rays compared with expectations from known galactic sources. Fermi LAT [62] and H.E.S.S. [47] have measured an excess in the flux of electrons and positrons up to a TeV or more. The PAMELA satellite is sensitive to electrons and positrons up to a few hundred GeV in energy, and is able to distinguish positrons from electrons and charged hadrons. PAMELA detects an upturn in the fraction of positron events beginning around 7 GeV [7]. This is in contrast to the expected decline in the positron fraction from secondary production mechanisms. Curiously, no corresponding excess of protons or antiprotons has been detected [63].

Although conventional astrophysical sources may ultimately prove the explanation of the anomalous cosmic ray data [52, 64], an intriguing possibility is that

---

[1] This chapter was previously published in Phys. Rev. D82 (2010) 055028.

dark matter annihilation or decay provides the source of the excess leptons. If dark matter annihilation is responsible for the excess leptons, then the annihilation cross section typically requires a large boost factor $\sim 100-1000$ to produce the observed signal [65]. Possible sources of the boost factor include Sommerfeld enchancement from additional attractive interactions in the dark sector [49], WIMP capture [66, 67] or Breit-Wigner resonant enhancement [50, 68, 69].

Alternatively, decaying dark matter can provide an explanation of the cosmic ray data if the dark matter decay channels favor leptonic over hadronic final states [70–89]. A typical scenario of this type that is consistent with PAMELA and Fermi LAT data includes dark matter with a mass of a few TeV that decays to leptons, with an anomalously long lifetime of $\sim 10^{26}$ seconds [51, 90]. From a model-building perspective, an intriguing issue is the origin of this long lifetime, and whether it can be explained with a minimum of theoretical contrivance. With this goal in mind, we present a new model of TeV-scale dark matter, one in which an anomalous global symmetry prevents dark matter decays except through instantons of a non-Abelian gauge field in the dark sector. Instanton-induced decays naturally produce the long required lifetime. Small mixings between standard model leptons and dark fermions gives rise to the leptonic final states observed in the cosmic ray data. Dark matter annihilation through the Higgs portal allows for the appropriate dark matter relic abundance, with dark matter masses consistent with the range preferred by PAMELA and Fermi-LAT data.

Superheavy dark matter decays through instantons have been considered before as a possible explanation for ultra-high energy cosmic ray signals, but those scenarios assumed superheavy dark matter with a mass of 10^{13} GeV or higher [91] which cannot simultaneously explain the lower energy electron and positron flux being considered here. Models of anomaly-induced dark matter decays without a dark gauge sector can also be constructed. For example, a supersymmetric extension

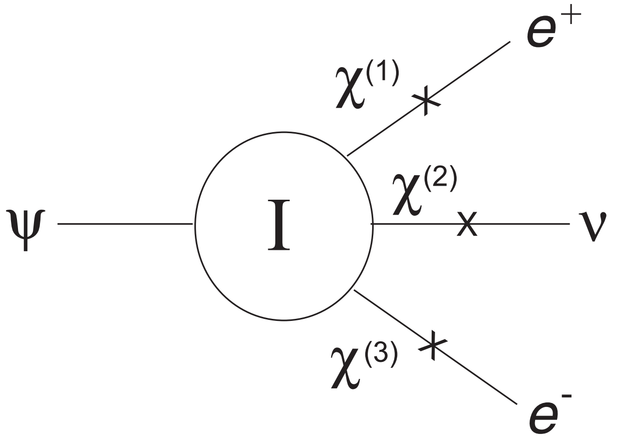

FIG. 2.1: Dark matter decay vertex. The circle represents the instanton-induced interaction, while X's represent mass mixing between the χ fields and standard model leptons. Note that e and ν represent leptons of any generation.

of the radiative seesaw model of neutrino masses can explain the PAMELA data through dark matter decays via an anomalous discrete symmetry [92]. The TeV-scale model we present, which is based on the smallest, continuous non-Abelian dark gauge group and smallest set of exotic particles necessary to implement our idea, suggests a prototypical set of new particles and interactions that could perhaps be probed at the LHC.

In Section 2.2 we present the model and describe the leptonic decay mode via instantons. In Section 2.3 we consider dark matter annihilation channels and demonstrate that annihilation through the Higgs portal can lead to the measured dark matter relic density. In Section 2.4 we consider dark matter interactions with nuclei and find that our model is safely below current direct detection bounds. We conclude in Section 2.5.

2.2 The Model

The gauge group of the dark sector is SU(2)$_D$×U(1)$_D$. The matter content consists of four sets of left-handed SU(2)$_D$ doublets and right-handed singlets:

$$\psi_L \equiv \begin{pmatrix} \psi_u \\ \psi_d \end{pmatrix}_L \quad \psi_{uR},\ \psi_{dR}\ ; \quad \chi_L^{(i)} \equiv \begin{pmatrix} \chi_u^{(i)} \\ \chi_d^{(i)} \end{pmatrix}_L \quad \chi_{uR}^{(i)},\ \chi_{dR}^{(i)} \quad (i = 1\ldots 3) \tag{2.1}$$

We include an SU(2)$_D$ doublet and singlet Higgs field, H_D and η, respectively, that are responsible for completely breaking the dark gauge group. In addition, the Higgs field H_D is responsible for giving Dirac masses to the ψ and χ fields. The model is constructed so that ψ number corresponds to an anomalous global symmetry that is violated by the $\psi\chi^{(1)}\chi^{(2)}\chi^{(3)}$ vertex generated via SU(2)$_D$ instantons, as indicated in Fig. 2.1. The χ fields are assigned hypercharges so that they mix with standard model leptons, leading to the decay $\psi \to \ell^+\ell^-\nu$. The required lifetime ($\sim 10^{26}$ s) and the appropriate dark matter relic density ($\Omega_D h^2 \sim 0.1$) constrain the free parameters of the model.

The charge assignments for these fields are summarized in Table 2.1.

TABLE 2.1: Particles charged under the dark gauge groups. The SU(2)$_D$×U(1)$_D$ charge assignments are indicated in parentheses; the subscripts +, − and 0 represent the standard model hypercharges +1, −1 and 0, respectively. Note that the ψ and χ states are fermions, while the H_D and η are complex scalars.

ψ_L	$(\mathbf{2}, -1/2)_0$	$\psi_{uR},\ \psi_{dR}$	$(\mathbf{1}, -1/2)_0$
$\chi_L^{(1)}$	$(\mathbf{2}, +1/6)_+$	$\chi_{uR}^{(1)},\ \chi_{dR}^{(1)}$	$(\mathbf{1}, +1/6)_+$
$\chi_L^{(2)}$	$(\mathbf{2}, +1/6)_0$	$\chi_{uR}^{(2)},\ \chi_{dR}^{(2)}$	$(\mathbf{1}, +1/6)_0$
$\chi_L^{(3)}$	$(\mathbf{2}, +1/6)_-$	$\chi_{uR}^{(3)},\ \chi_{dR}^{(3)}$	$(\mathbf{1}, +1/6)_-$
H_D	$(\mathbf{2}, 0)_0$	η	$(\mathbf{1}, 1/6)_0$

Let us first discuss the consistency of the charge assignments. Cancellation of the $\mathrm{SU}(2)_D^2$ U(1) anomalies requires that the sum of the U(1) charges over all the dark doublet fermion fields must vanish. As one can see from Table 2.1, this is clearly the case for the $\mathrm{U}(1)_D$ and $\mathrm{U}(1)_Y$ charges of the left-handed doublet ψ and χ fields. Since SU(2) is an anomaly free group and has traceless generators, all other $\mathrm{SU}(2)_D$ anomalies vanish trivially. Now consider the $\mathrm{U}(1)_D^p\mathrm{U}(1)_Y^q$ anomalies (where p and q are non-negative integers satisfying $p+q=3$). For each field in Table 2.1 with a given $\mathrm{U}(1)_D\times\mathrm{U}(1)_Y$ charge assignment, one notes that there is another with the same charge assignment but opposite chirality. As far as the Abelian groups are concerned, the theory is vector-like and the corresponding anomalies vanish. Finally, we note that the theory has precisely four $\mathrm{SU}(2)_D$ doublets and is free of a Witten anomaly.

The gauge symmetries of the model lead to a global $\mathrm{U}(1)_\psi$ symmetry that prevents the decay of the lightest ψ mass eigenstate at any order in perturbation theory. To confirm this statement, we need to show that all renormalizable interactions that violate this symmetry are forbidden by the dark-sector gauge symmetry. The possible problematic interactions that could violate this global symmetry fall into the following categories:

1. Terms involving $\overline{\psi^c}\psi$. Here the superscript indicates charge conjugation, $\psi^c \equiv i\gamma^0\gamma^2\overline{\psi}^T$. This combination has $\mathrm{U}(1)_\psi$ charge +2. However, it also has $\mathrm{U}(1)_D$ charge -1. Since we have no Higgs field with the $\mathrm{U}(1)_D$ charge ±1, there are no renormalizable interactions that violate ψ number by two units.

2. Terms involving a χ fermion and ψ or ψ^c. Such terms violate ψ number by ±1 unit. However, the possible bilinears involving ψ and any χ have $\mathrm{U}(1)_D$ charges $\pm1/3$ or $\pm2/3$. Again, we have no Higgs field with the necessary $\mathrm{U}(1)_D$ charge to form a renormalizable gauge invariant term of this type.

3. Terms involving a standard model fermion and ψ or ψ^c. Such an interaction would violate ψ number by ±1, but would have $\mathrm{U}(1)_D$ charge $\pm1/2$. Again,

we have no Higgs fields with charge $\pm 1/2$ that would allow the construction of a renormalizable invariant.

Since the renormalizable interactions of the theory have an unbroken $\mathrm{U}(1)_\psi$ symmetry, no perturbative process involving these interactions will violate the global symmetry. However, since the $\mathrm{SU}(2)_D^2\ \mathrm{U}(1)_\psi$ anomaly is non-zero, non-perturbative interactions due to instantons will generate operators that violate the $\mathrm{U}(1)_\psi$ symmetry.

Instantons are gauge field configurations which stationarize the Euclidean action but have a nontrivial winding number around the three-sphere at infinity. Following 't Hooft [93, 94], if there are N_f Dirac pairs of chiral fermions which transform in the fundamental representation of a gauge group, then due to the chiral anomaly a one-instanton configuration violates the axial $\mathrm{U}(1)_A$ charge by $2N_f$ units. The non-Abelian, $\mathrm{SU}(N_f)\times\mathrm{SU}(N_f)$ chiral symmetry is non-anomalous, so the instanton process must involve the $2N_f$ chiral fermions in a symmetric fashion. Fig. 2.1 shows the effective $\psi\chi^{(1)}\chi^{(2)}\chi^{(3)}$ interaction induced by the instanton configuration in our model.[2] Given the hypercharge assignments of the χ fields, these states have electric charges $+1$, 0 and -1, the same as standard model leptons, of any generation. After the dark and standard model gauge symmetries are spontaneously broken, there is no symmetry which prevents the χ states and the standard model leptons from mixing. By including a single vector-like lepton pair, we now show that mixing leading to the decay $\psi \to \ell^+\ell^-\nu$ can arise via purely renormalizable interactions.

We introduce a vector-like lepton pair, E_L, E_R, with mass M_E and the same quantum numbers as a right-handed electron; in the notation of Table 2.1:

$$E_L \sim E_R \sim (\mathbf{1}, 0)_- \ . \tag{2.2}$$

---

[2] In this model, Planck-suppressed operators of this form, if they are present, are negligible compared to the instanton-induced effects.

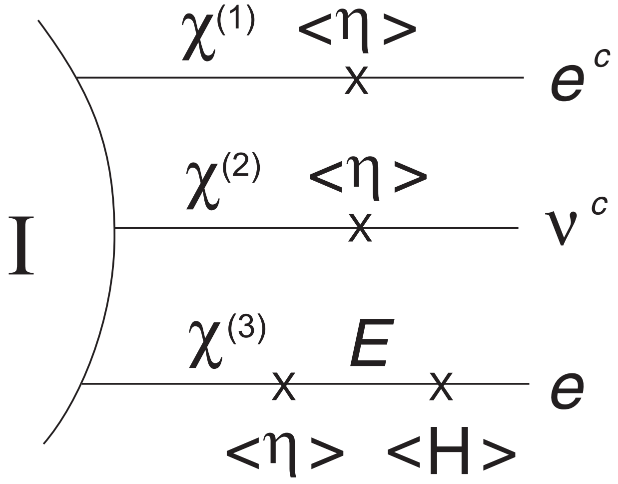

FIG. 2.2: Diagrammatic interpretation of mixing from χ states to standard model fermions, corresponding to the right-hand-side of Fig. 2.1. Here E represents the vector-like lepton described in the text, and H is the standard model Higgs.

In addition, we assume in this model that standard model neutrinos have purely Dirac masses. If the Higgs vacuum expectation values (vevs) are smaller than the masses of the heavy states, then the mixing to standard model leptons shown in Fig. 2.1 can be estimated via the diagram in Fig. 2.2. Otherwise, one has to diagonalize the appropriate fermion mass matrices. We discuss the exact diagonalization in an appendix for the reader who is interested in the details. Here, the diagrammatic approach is sufficient to establish that the mixing is present, and is no larger than order $\langle\eta\rangle/M_\chi$, $\langle\eta\rangle/M_\chi$, and $\langle\eta\rangle\langle H\rangle/(M_\chi M_E)$, where H is the standard model Higgs, for the $\chi_L^{(1)} - e_R^c$, $\chi_L^{(2)} - \nu_R^c$ and $\chi_L^{(3)} - e_L$ mixing angles, respectively. We take each mixing angle to be 0.01 in the estimates that follow, and demonstrate in the appendix how this choice can be easily obtained. Further, we assume that decays to the heavy eigenstates are not kinematically allowed, as is also illustrated in the appendix. Due to the mixing, the $\chi^{(i)}$ particles decay quickly to standard model particles via couplings to the Higgs bosons and standard model electroweak gauge bosons. The heavier ψ mass eigenstate decays to lighter states via $\mathrm{SU}(2)_D$ gauge-boson-exchange interactions.

The instanton-induced vertex in Fig. 2.1 follows from an interaction of the form

$$\begin{aligned}\mathcal{L}_I \;&=\; \frac{C}{6\,g_D^8}\exp\left(-\frac{8\pi^2}{g_D^2}\right)\left(\frac{m_\psi}{v_D}\right)^{35/6}\frac{1}{v_D^2}\left(2\,\delta_{\alpha\beta}\delta_{\gamma\sigma}-\delta_{\alpha\sigma}\delta_{\beta\gamma}\right)\\ &\cdot\left[(\overline{\chi_{L\,\beta}^{(2)\,c}}\psi_L^\alpha)(\overline{\chi_{L\,\sigma}^{(1)\,c}}\chi_L^{(3)\,\gamma})-(\overline{\chi_{L\,\beta}^{(1)\,c}}\psi_L^\alpha)(\overline{\chi_{L\,\sigma}^{(2)\,c}}\chi_L^{(3)\,\gamma})\right]+\text{ h.c.}\,, \qquad (2.3)\end{aligned}$$

where α, β, γ and σ are $\mathrm{SU}(2)_D$ indices [94, 95]. The dimensionless coefficient C can be computed using the results in Ref. [94] and one finds $C \approx 7\times 10^8$. The operators in Eq. (2.3) lead, via mixing, to operators of the form $\bar{\nu}_R\psi_L\bar{e}_R e_L$ and $\bar{e}_R\psi_L\bar{\nu}_R e_L$. Assuming that the product of mixing angles is $\approx 10^{-6}$, as discussed earlier, one may estimate the decay width:

$$\Gamma(\psi\to\ell^+\ell^-\nu)\approx\frac{1}{g_D^{16}}\exp(-16\pi^2/g_D^2)\left(\frac{m_\psi}{v_D}\right)^{47/3} m_\psi\ . \qquad (2.4)$$

For example, for $m_\psi = 3.5$ TeV and $v_D = 4$ TeV, one obtains a dark matter lifetime of 10^{26} s for

$$g_D \approx 1.15\,, \qquad (2.5)$$

where g_D is defined in dimensional regularization and renormalized at the scale m_ψ [94]. For similar parameter choices, one can slightly adjust g_D to maintain the desired lifetime. As mentioned earlier, dimension-six Planck-suppressed operators are much smaller than the operators in Eq. (2.3). Sphaleron-induced interactions are suppressed by $\sim\exp[-4\pi v_D/(g_D T)]\sim\exp(-44\ \mathrm{TeV}/T)$, and become negligible well before the temperature at which dark matter freeze out occurs.

Finally, let us consider whether the choice $v_D = 4$ TeV conflicts with other meaningful constraints on the heavy particle content of the model. In short, a spectrum of ~ 4 TeV χ and E fermions with order 0.01 mixing angles with standard model leptons presents no phenomenological problems. These states are above all direct detection bounds; they are vector-like under the standard model gauge group so that the S parameter is small; they mix weakly enough with standard model leptons so that other precision observables are negligibly affected. On this last point, we note that the correction to the muon and Z-boson decay widths due to the fermion mixing is a factor of 10^{-8} smaller than the widths predicted in the standard model, which is within the current experimental uncertainties. The dark sector gauge bosons are also phenomenologically safe. They do not have couplings that distinguish standard model lepton flavor (since they do not couple directly to standard model leptons) so that tree-level lepton-flavor violating processes are absent. The effective four-standard-model-fermion operators that are induced by dark gauge boson exchanges are suppressed by $\sim (0.01)^4/v_D^2 \sim 1/(40,000 \text{ TeV})^2$, which is consistent with the existing contact interaction bounds [5].

We now turn to the question of whether the model provides for the appropriate dark matter relic density.

2.3 Relic Density

For the regions of model parameter space considered in this section, dark matter annihilations to standard model particles proceed via mixing between the dark and ordinary Higgs bosons, often described as the Higgs portal [96]. We take into account mixing between the doublet Higgs fields, H_D and H, in our discussion below. This is consistent with a simplifying assumption that the η Higgs does not mix with the others in the scalar potential. Such an assumption is adequate for our purposes since we aim only to show that some parameter region exists in which the correct dark matter relic density is obtained. Consideration of a more general potential would likely provide additional solutions in a much larger parameter space, but would not alter the conclusion that the desired relic density can be achieved.

In this section, ψ will refer to the dark matter mass eigenstate, *i.e.*, the lightest mass eigenstate of the ψ_u-ψ_d mass matrix, which we take as diagonal, for convenience. The potential for the doublet fields has the form:

$$V = -\mu^2 H^\dagger H + \lambda (H^\dagger H)^2 - \mu_D^2 H_D^\dagger H_D + \lambda_D (H_D^\dagger H_D)^2 + \lambda_{mix} (H^\dagger H)(H_D^\dagger H_D). \quad (2.6)$$

In unitary gauge, H and H_D are given by

$$H = \frac{1}{\sqrt{2}} \begin{bmatrix} 0 \\ v + h \end{bmatrix}, \qquad H_D = \frac{1}{\sqrt{2}} \begin{bmatrix} 0 \\ v_D + h_D \end{bmatrix}, \quad (2.7)$$

where v and v_D are the H and H_D vevs, respectively. At the extrema of this potential,

$$\begin{aligned} &v\,(-\mu^2 + \lambda\, v^2 + \frac{1}{2}\lambda_{mix}\, v_D^2) = 0 \\ &v_D\,(-\mu_D^2 + \lambda_D\, v_D^2 + \frac{1}{2}\lambda_{mix}\, v^2) = 0\,. \end{aligned} \quad (2.8)$$

The h-h_D mass matrix follows from Eq. (2.6),

$$M_H^2 = \begin{pmatrix} 2\,\lambda\, v^2 & \lambda_{mix}\, v\, v_D \\ \lambda_{mix}\, v\, v_D & 2\,\lambda_D\, v_D^2 \end{pmatrix}. \quad (2.9)$$

Diagonalizing the mass matrix, one finds the mass eigenvalues

$$m_{1,2}^2 = (\lambda_D v_D^2 + \lambda\, v^2) \mp (\lambda_D v_D^2 - \lambda v^2)\sqrt{1+y^2}, \quad (2.10)$$

where

$$y = \frac{\lambda_{mix} v\, v_D}{\lambda_D v_D^2 - \lambda\, v^2}. \quad (2.11)$$

The mass eigenstates h_1 and h_2 are related to h and h_D by a mixing angle

$$\begin{aligned} h_1 &= h\cos\theta - h_D \sin\theta \\ h_2 &= h\sin\theta + h_D \cos\theta, \end{aligned} \tag{2.12}$$

where

$$\tan 2\,\theta = y \ . \tag{2.13}$$

Dark matter annihilations proceed via exchanges of the physical Higgs states h_1 and h_2. We take into account the final states W^+W^-, ZZ, h_1h_1 and $t\bar{t}$, where t represents the top quark. For the parameter choices considered later, final states involving h_2 will be subleading. The relevant annihilation cross sections are given by

$$\begin{aligned} \sigma_{W^+W^-} &= \frac{g^2 m_\psi^2 \sin^2\theta\cos^2\theta}{128\pi m_W^2 v_D^2} s^2 \left| \frac{1}{s-m_1^2+im_1\Gamma_1} - \frac{1}{s-m_2^2+im_2\Gamma_2} \right|^2 \\ &\times \sqrt{1-\frac{4m_\psi^2}{s}} \sqrt{1-\frac{4m_W^2}{s}} \left(1-\frac{4m_W^2}{s}+\frac{12m_W^4}{s^2}\right) \ , \end{aligned} \tag{2.14}$$

$$\begin{aligned} \sigma_{ZZ} &= \frac{g^2 m_\psi^2 \sin^2\theta\cos^2\theta}{256\pi m_W^2 v_D^2} s^2 \left| \frac{1}{s-m_1^2+im_1\Gamma_1} - \frac{1}{s-m_2^2+im_2\Gamma_2} \right|^2 \\ &\times \sqrt{1-\frac{4m_\psi^2}{s}} \sqrt{1-\frac{4m_Z^2}{s}} \left(1-\frac{4m_Z^2}{s}+\frac{12m_Z^4}{s^2}\right) \ , \end{aligned} \tag{2.15}$$

$$\begin{aligned} \sigma_{h_1h_1} &= \frac{m_\psi^2}{16\pi v_D^2} \left| \frac{3g_{111}\sin\theta}{s-m_1^2+im_1\Gamma_1} + \frac{g_{112}\cos\theta}{s-m_2^2+im_2\Gamma_2} \right|^2 \\ &\times \sqrt{1-\frac{4m_\psi^2}{s}} \sqrt{1-\frac{4m_{h_1}^2}{s}} \ , \end{aligned} \tag{2.16}$$

$$\begin{aligned}\sigma_{t\bar{t}} &= \frac{3m_\psi^2 m_t^2 \sin^2\theta\cos^2\theta}{16\pi v_D^2 v^2} s \left| \frac{1}{s-m_1^2+im_1\Gamma_1} - \frac{1}{s-m_2^2+im_2\Gamma_2} \right|^2 \\ &\times \left(1-\frac{4m_t^2}{s}\right)\left(1-\frac{4m_\psi^2}{s}\right) \ . \end{aligned} \tag{2.17}$$

In Eqs. (2.14) and (2.15), g is the standard model SU(2) gauge coupling. In Eq. (2.16), g_{111} and g_{112} represent the h_1^3 and $h_2 h_1^2$ couplings, respectively:

$$\begin{aligned} g_{111} &= (\lambda\cos^3\theta + \frac{1}{2}\lambda_{mix}\cos\theta\sin^2\theta)\, v - (\lambda_D \sin^3\theta + \frac{1}{2}\lambda_{mix}\sin\theta\cos^2\theta)\, v_D \ , \\ g_{112} &= [3\lambda\cos^2\theta\sin\theta - \lambda_{mix}(\cos^2\theta\sin\theta - \frac{1}{2}\sin^3\theta)]\, v \\ &\qquad + [3\lambda_D\sin^2\theta\cos\theta - \lambda_{mix}(\sin^2\theta\cos\theta - \frac{1}{2}\cos^3\theta)]\, v_D \, . \end{aligned} \tag{2.18}$$

Finally, in all our annihilation cross sections, Γ_1 (Γ_2) represents the decay width of the Higgs field h_1 (h_2). The width Γ_1 is comparable to that of a standard model Higgs boson and can be neglected without noticeably affecting our numerical results. However, since our eventual parameter choices will place the mass of the heavier Higgs field around $2m_\psi$, we must retain Γ_2; the leading contributions to Γ_2 come from the same final states relevant to the ψ annihilation cross section:

$$\begin{aligned} \Gamma_{h_2\to W^+W^-} &= \frac{g^2 m_2^3}{64\pi m_W^2}\sin^2\theta\sqrt{1-\frac{4m_W^2}{m_2^2}}\left(1-\frac{4m_W^2}{m_2^2}+\frac{12m_W^4}{m_2^4}\right) \\ \Gamma_{h_2\to ZZ} &= \frac{g^2 m_2^3}{128\pi m_W^2}\sin^2\theta\sqrt{1-\frac{4m_Z^2}{m_2^2}}\left(1-\frac{4m_Z^2}{m_2^2}+\frac{12m_Z^4}{m_2^4}\right) \\ \Gamma_{h_2\to h_1 h_1} &= \frac{g_{112}^2}{32\pi m_2}\sqrt{1-\frac{4m_1^2}{m_2^2}} \\ \Gamma_{h_2\to t\bar{t}} &= \frac{3m_2 m_t^2}{8\pi v^2}\sin^2\theta\left(1-\frac{4m_t^2}{m_2^2}\right)^{3/2} \ . \end{aligned} \tag{2.19}$$

The evolution of the ψ number density, n_ψ, is governed by the Boltzmann

TABLE 2.2: Examples of viable parameter sets for $v_D = 4$ TeV. For each point listed, $\Omega_D h^2 \approx 0.1$ and the Higgs masses are consistent with the LEP bound.

m_ψ(TeV)	$\sqrt{2\lambda v^2}$(TeV)	$\sqrt{2\lambda_D v_D^2}$(TeV)	λ_{mix}	m_1(GeV)	m_2(TeV)
1.0	0.19	1.98	0.30	117	1.99
1.5	0.22	2.98	0.40	175	2.98
2.0	0.26	3.97	0.56	220	3.97
2.5	0.27	4.97	0.65	237	4.97
3.0	0.29	5.96	0.80	258	5.96
3.5	0.31	6.96	0.90	283	6.96
4.0	0.35	7.95	1.10	322	7.95

equation

$$\frac{dn_\psi}{dt} + 3H(t)n_\psi = -\langle\sigma v\rangle[n_\psi^2 - (n_\psi^{EQ})^2], \tag{2.20}$$

where $H(t)$ is the Hubble parameter and n_ψ^{EQ} is the equilibrium number density. The thermally-averaged annihilation cross section times relative velocity $\langle\sigma v\rangle$ is given by [97]

$$\langle\sigma v\rangle = \frac{1}{8m_\psi^4 T K_2^2(m_\psi/T)} \int_{4m_\psi^2}^{\infty} (\sigma_{tot})\,(s - 4m_\psi^2)\sqrt{s}\,K_1(\sqrt{s}/T)\,ds \ , \tag{2.21}$$

where σ_{tot} is the total annihilation cross section, and the K_i are modified Bessel functions of order i. We evaluate the freeze-out condition [3]

$$\frac{\Gamma}{H(t_F)} \equiv \frac{n_\psi^{EQ}\langle\sigma v\rangle}{H(t_F)} \approx 1 \ , \tag{2.22}$$

to find the freeze-out temperature T_f, or equivalently $x_f \equiv m_\psi/T_f$. We assume the non-relativistic equilibrium number density

$$n_\psi^{EQ} = 2\left(\frac{m_\psi T}{2\pi}\right)^{3/2} e^{-m_\psi/T} \ , \tag{2.23}$$

and the Hubble parameter $H = 1.66\, g_*^{1/2}\, T^2/m_{Pl}$, appropriate to a radiation-dominated universe. The symbol g_* represents the number of relativistic degrees of freedom and $m_{Pl} = 1.22 \times 10^{19}$ GeV is the Planck mass. For the parameter choices in Tables 2.2 and 2.3, we find $x_f \sim 27$–28. We approximate the relic abundance using [97]

$$\frac{1}{Y_0} = \frac{1}{Y_f} + \sqrt{\frac{\pi}{45}} m_{Pl} m_\psi \int_{x_f}^{x_0} \frac{g_*^{1/2}}{x^2} \langle \sigma v \rangle \, dx \tag{2.24}$$

where Y is the ratio of the number to entropy density and the subscript 0 indicates the present time. The ratio of the dark matter relic density to the critical density ρ_c is given by $\Omega_D = Y_0 s_0 m_\psi / \rho_c$, where s_0 is the present entropy density, or equivalently

$$\Omega_D h^2 \approx 2.8 \times 10^8 \text{ GeV}^{-1}\, Y_0\, m_\psi \ \ . \tag{2.25}$$

In our numerical analysis, we assume that the heavy states are sufficiently non-degenerate, so that we do not have to consider co-annihilation processes [98]. In Tables 2.2 and 2.3, we show representative points in the model's parameter space, spanning a range of ψ masses, in which we obtain the correct dark matter relic abundance, $\Omega_D h^2 \approx 0.1$, and in which the masses m_1 and m_2 are consistent with the LEP bound $m_{1,2} > 114.4$ GeV [5].

It is common wisdom that weakly interacting dark matter candidates with masses of a few hundred GeV typically yield relic densities in the correct ballpark. We have assumed masses above 1 TeV since most fits to the positron excess in PAMELA and Fermi LAT indicate that a decaying dark matter candidate should have a mass in this range. One would therefore expect that $\Omega_D h^2$ in our model should be larger than desirable. The reason this is not the case is that we have chosen parameters for which the heavier Higgs h_2 is within 1% of $2m_\psi$, leading to a resonant enhancement in the annihilation rate. While we would be happier without

TABLE 2.3: Examples of viable parameter sets for $v_D = 4$ TeV, with m_1 below 130 GeV. For each point listed, $\Omega_D h^2 \approx 0.1$ and the Higgs masses are consistent with the LEP bound.

m_ψ(TeV)	$\sqrt{2\lambda v^2}$(TeV)	$\sqrt{2\lambda_D v_D^2}$(TeV)	λ_{mix}	m_1(GeV)	m_2(TeV)
1.0	0.19	1.98	0.30	117	1.99
1.5	0.18	2.98	0.40	122	2.98
2.0	0.19	3.97	0.57	127	3.97
2.5	0.18	4.97	0.65	125	4.97
3.0	0.18	5.96	0.80	122	5.96
3.5	0.18	6.96	0.90	127	6.96
4.0	0.18	7.95	1.10	117	7.95

this tuning, it is no larger than tuning that exists in, for example, the Higgs sector of the minimal supersymmetric standard model. It is also worth pointing out that this tuning is related to the portal that connects the dark to standard model sectors of the theory and is not strictly tied to the mechanism that we have proposed for dark matter decay. Other portals are possible. For example, one might study the limit of the model in which the U$(1)_D$ gauge boson is lighter and kinetically mixes with hypercharge, a possibility that would lead to other annihilation channels. Finally, we point out that Tables 2.2 and 2.3 includes $m_\psi = 3.5$ TeV, which naively corresponds to the value preferred by a fit to the PAMELA and Fermi-LAT data, assuming a spin-1/2 dark matter candidate that decays to $\ell^+\ell^-\nu$ [51]. However, other masses should not be discounted since astrophysical sources may also contribute to the observed positron excess [52, 64].

2.4 Direct Detection

We now consider whether the parameter choices described in the previous section are consistent with the current bounds from direct detection experiments. The most relevant constraints come from experiments that search for spin-independent,

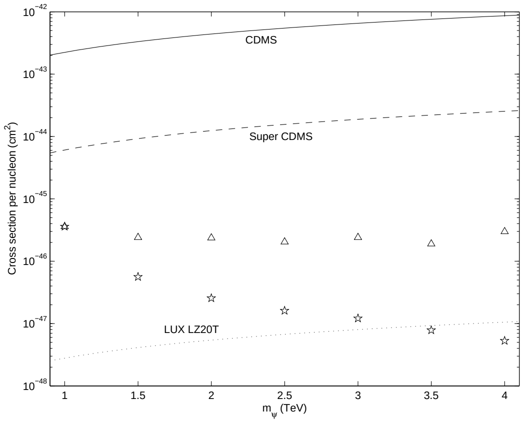

FIG. 2.3: Dark matter-nucleon elastic scattering cross section for the parameter sets in Table 2.2 (stars) and Table 2.3 (triangles). The solid line is the current bound from CDMS Soudan 2004-2009 Ge [10]. The dashed line represents the projected bound from SuperCDMS Phase A. The dotted line represents the projected reach of the LUX LZ20T experiment, assuming 1 event sensitivity and 13 ton-kilodays. The graph is obtained using the DM Tools software available at http://dmtools.brown.edu.

elastic scattering of dark matter off target nuclei. The relevant low-energy effective interaction from t-channel exchanges of the Higgs mass eigenstates is given by

$$\mathcal{L}_{int} = \sum_q \alpha_q \, \bar{\psi}\psi \, \bar{q}q \ , \tag{2.26}$$

where

$$\alpha_q = \frac{m_q m_\psi \sin\theta \cos\theta}{v \, v_D} \left(\frac{1}{m_1^2} - \frac{1}{m_2^2} \right) . \tag{2.27}$$

This interaction is valid for momentum exchanges that are small compared to $m_{1,2}$, which is always the case given that typical dark matter velocities are non-relativistic. Following the approach of Ref. [99], Eq. (2.26) leads to an effective interaction with nucleons

$$\mathcal{L}_{eff} = f_p \, \bar{\psi}\psi \, \bar{p}p + f_n \, \bar{\psi}\psi \, \bar{n}n \ , \tag{2.28}$$

where f_p and f_n are related to α_q through the relation [99]

$$\frac{f_{p,n}}{m_{p,n}} = \sum_{q=u,d,s} \frac{f_{Tq}^{(p,n)} \alpha_q}{m_q} + \frac{2}{27} f_{Tg}^{(p,n)} \sum_{q=c,b,t} \frac{\alpha_q}{m_q}, \tag{2.29}$$

where $\langle n|m_q \bar{q} q|n\rangle = m_n f_{Tq}^n$. Numerically, the $f_{Tq}^{(p,n)}$ are given by [100]

$$f_{Tu}^p = 0.020 \pm 0.004,\ f_{Td}^p = 0.026 \pm 0.005,\ f_{Ts}^p = 0.118 \pm 0.062 \tag{2.30}$$

and

$$f_{Tu}^n = 0.014 \pm 0.003,\ f_{Td}^n = 0.036 \pm 0.008,\ f_{Ts}^n = 0.118 \pm 0.062\ , \tag{2.31}$$

while $f_{Tg}^{(p,n)}$ is defined by

$$f_{Tg}^{(p,n)} = 1 - \sum_{q=u,d,s} f_{Tq}^{(p,n)}\ . \tag{2.32}$$

We can approximate $f_p \approx f_n$ since f_{Ts} is larger than other f_{Tq}'s and f_{Tg}. For the purpose of comparing the predicted cross section with existing bounds, we evaluate the cross section for scattering off a single nucleon, which can be approximated

$$\sigma_n \approx \frac{m_r^2 f_p^2}{\pi} \tag{2.33}$$

where m_r is nucleon-dark matter reduced mass $1/m_r = 1/m_n + 1/m_\psi$. Our results are shown in Fig. 2.3, for the parameter sets given in Tables 2.2 and 2.3. The predicted cross sections are far below the current CDMS bounds [10] for dark matter masses between 1 and 4 TeV. However, there is hope that the model can be probed by the future LUX LZ20T experiment [101, 102].

2.5 Conclusions

We have presented a new TeV-scale model of decaying dark matter. The approximate stability of the dark matter candidate, ψ, is a consequence of a global U(1) symmetry that is exact at the perturbative level, but is violated by instanton-induced interactions of a non-Abelian dark gauge group. The instanton-induced vertex couples the dark matter candidate to heavy, exotic states that mix with standard model leptons; the dark matter then decays to $\ell^+\ell^-\nu$ final states, where the leptons can be of any generation desired. We have shown that a lifetime of $\sim 10^{26}$ s, which is desirable in decaying dark matter scenarios, can be obtained for perturbative values of the non-Abelian dark gauge coupling. In addition, by studying dark matter annihilations through the Higgs portal, we have provided examples of parameter regions in which the appropriate dark matter relic density may be obtained, assuming dark matter masses that are consistent with fits to the results from the PAMELA and Fermi-LAT experiments. The nucleon-dark matter cross section in our model is lower than the present bound from CDMS, but may be probed in future experiments. It might also be possible to probe the spectrum of our model at the LHC.

The model in this chapter provides a concrete, TeV-scale scenario in which dark matter decay is mediated by instantons, and gives a new motivation for the study of non-Abelian dark gauge groups [103–107]. However, it is by no means the only possible model of this type. One might study variations of the model in which different annihilation channels are dominant, or the dark matter is lighter, or the standard model leptons are directly charged under the new non-Abelian gauge group. It may also be worthwhile to consider how low-scale leptogenesis and baryogenesis might be accommodated in this type of scenario. While we have assumed parameter choices motivated by the observed cosmic ray positron excess, one might incorporate the present model in a multi-component dark matter scenario if this were required to explain new results from ongoing and future direct detection experiments.

CHAPTER 3

A Froggatt-Nielsen Model for Leptophilic Scalar Dark Matter Decay[3]

3.1 Introduction

A number of earth-, balloon-, and satellite-based experiments have observed anomalies in the spectra of cosmic ray electrons and positrons. Fermi-LAT [62] and H.E.S.S. [47] have measured an excess in the flux of electrons and positrons up to, and beyond 1 TeV, respectively. PAMELA [7], which is sensitive to electrons and positrons up to a few hundred GeV in energy, detects an upturn in the positron fraction beginning around 7 GeV, in disagreement with the expected decline from secondary production mechanisms. Recent measurements at Fermi-LAT support this result [45]. In contrast, current experiments observe no excess in the proton or antiproton flux [63]. Although astrophysical explanations are possible [52, 64], these

---

[3] This chapter was previously published in Phys. Rev. D84 (2011) 035002.

observations can be explained if the data includes a contribution from the decays of unstable dark matter particles that populate the galactic halo [51, 84, 90, 108–119]. The dark matter candidate must be TeV-scale in mass, have a lifetime of order 10^{26} seconds, and decay preferentially to leptons. A number of scenarios have been proposed to explain the desired dark matter lifetime and decay properties [70, 71, 73, 75, 77–79, 81, 85, 87, 92, 120–145].

To be more quantitative, consider a scalar dark matter candidate χ which (after the breaking of all relevant gauge symmetries) has an effective coupling g_{eff} to some standard model fermion f given by $g_{eff}\chi\bar{f}_L f_R + \text{h.c.}$ To obtain a lifetime of 10^{26} seconds, one finds $g_{eff} \sim 10^{-26}$ if $m_\chi \sim 3$ TeV. From the perspective of naturalness, the origin of such a small dimensionless number requires an explanation. One possibility is that physics near the dark matter mass scale is entirely responsible for the appearance of a small number, as is the case in models where a global symmetry, that would otherwise stabilize the dark matter candidate, is broken by instanton effects of a new non-Abelian gauge group G_D. A leptophilic model of fermionic dark matter along these lines was presented in Ref. [120]: the new gauge group is broken not far above the dark matter mass scale and the effective coupling is exponentially suppressed, $g_{eff} \propto \exp(-16\pi^2/g_D^2)$, where g_D is the G_D gauge coupling. (An example of a supersymmetric model with anomaly-induced dark matter decays can be found in Ref. [92].) On the other hand, the appearance of a small effective coupling can arise if the breaking of the stabilizing symmetry is communicated to the dark matter via higher-dimension operators suppressed by some high scale M. Then it is possible that g_{eff} is suppressed by $(m_\chi/M)^p$, for some power p; it is well known that for $m_\chi \sim \mathcal{O}(1)$ TeV and $p = 2$, the correct lifetime can be obtained for $M \sim \mathcal{O}(10^{16})$ GeV, remarkably coincident with the grand unification (GUT) scale in models with TeV-scale supersymmetry (SUSY) [77, 121]. If the LHC fails to find SUSY in the coming years, however, then the association of 10^{16} GeV with a fundamental mass scale will no longer be strongly preferred. Exploring other alternatives is well motivated from this perspective and, in any event, may provide valuable insight into the range of possible decaying dark matter scenarios.

The very naive estimate for g_{eff} discussed above presumes that the result is determined by a TeV-scale dark matter mass m_χ, a single high scale M and no small dimensionless factors. Given these assumption, the choice $M = M_*$, where $M_* = 2 \times 10^{18}$ GeV is the reduced Planck mass, would not be viable: the dark matter decay rate is much too large for $p = 1$ (*i.e.*, there would be no dark matter left at the present epoch) and is much too small for $p = 2$ (*i.e.*, there would not be enough events to explain the cosmic ray $e^\pm$ excess). However, Planck-suppressed effects arise so generically that we should be careful not to discount them too quickly. What we show in the present chapter is that Planck-suppressed operators can lead to the desired dark matter lifetime if they correct new physics at an intermediate scale. In the model that we present, this is the scale at which Yukawa couplings of the standard model charged leptons are generated via the integrating out of vector-like states. This sector will have the structure of a Froggatt-Nielsen model [146]: an Abelian discrete symmetry will restrict the couplings of the standard model leptons and the vector-like states, but will be spontaneously broken by the vacuum expectation values (vevs) of a set of scalar fields $\{\phi\}$. Integrating out the heavy states will not only lead to the standard model charged lepton Yukawa couplings, but also to dark matter couplings that are naturally leptophilic and lead to dark matter decay. Aside from setting the overall scale of the charged lepton masses, the symmetry structure of our model will not restrict the detailed textures of the standard model Yukawa matrices. This feature is not automatic; symmetries introduced to guarantee dark matter leptophilia may also make it difficult to obtain the correct lepton mass matrices, at least without additional theoretical assumptions (for example, the addition of electroweak Higgs triplets, as in the model of Ref. [145]).

Our framework is free of such complications and is compatible, in principle, with many possible extensions that might address the full flavor structure of the standard model.

This chapter is organized as follows. In the next section, we present a model that illustrates our proposal. In Section 3.3, we compute the predicted $e^{\pm}$ flux, $\Phi(e^{\pm})$, and the positron fraction $\Phi(e^{+})/[\Phi(e^{+})+\Phi(e^{-})]$ for some points in the parameter space of our model and compare our results to the relevant cosmic ray data. It is worth noting that this analysis has applicability to any model that leads to similar dark matter decay operators. In Section 3.4, we comment on the relic density and dark matter direct detection in our example model. In Section 3.5, we summarize our conclusions.

3.2 A Model

We assume that the right-handed charged leptons of the standard model, e_R, and four sets of heavy vector-like charged leptons are constrained by the discrete symmetry

$$G = \mathbb{Z}_p \times \mathbb{Z}_q \,, \tag{3.1}$$

with p and q to be determined shortly. We assume that the vector-like leptons have the same electroweak quantum numbers as e_R

$$E_R^{(i)} \sim E_L^{(i)} \sim e_R, \quad (i = 1 \ldots 4) \,. \tag{3.2}$$

All the fields shown are assumed to be triplets in generation space, with their generation indices suppressed. Under the discrete symmetry, the fields in Eq. (3.2) are taken to transform as

$$e_R \rightarrow \omega^{-4}\, e_R \,, \tag{3.3}$$

$$E_{L,R}^{(i)} \to \omega^{1-i}\, E_{L,R}^{(i)}, \quad (i = 1 \ldots 4)\,. \tag{3.4}$$

We will take ω and η to be elements of $\mathbb{Z}_p$ and $\mathbb{Z}_q$, respectively, with $\omega^p = 1$ and $\eta^q = 1$. In addition, we assume the presence of a heavy right-handed neutrino, ν_R, that is a singlet under G. We note that the fields that are charged under G do not transform under any of the non-Abelian standard model gauge group factors, so that G satisfies the consistency conditions of a discrete gauge symmetry in the low-energy theory [147]; such discrete symmetries are not violated by quantum gravitational effects[4]. The Yukawa couplings of the standard model charged leptons arise when the symmetry G is spontaneously broken and the vector-like leptons are integrated out of the theory. Symmetry breaking is accomplished via the vacuum expectation values of two scalar fields ϕ_E and ϕ_D, which transform as

$$\begin{aligned} &\phi_E \to \omega\, \phi_E\,, \\ &\phi_D \to \eta\, \phi_D\,. \end{aligned} \tag{3.5}$$

The following renormalizable Lagrangian terms involving the charged lepton fields are allowed by the discrete symmetry:

$$\begin{aligned} \mathcal{L}_E &= \overline{L}_L H E_R^{(1)} + \sum_{i=1}^{3} \overline{E}_L^{(i)} \phi_E E_R^{(i+1)} + \overline{E}_L^{(4)} \phi_E\, e_R \\ &+ \sum_{i=1}^{4} M^{(i)}\, \overline{E}_L^{(i)} E_R^{(i)} + \text{ h.c.} \end{aligned} \tag{3.6}$$

---

[4] The consistency conditions require that anomalies involving the non-Abelian gauge groups that are linear in a continuous group that embeds G must vanish, as is automatic above. Ref. [147] indicates that no rigorous proof exists that the cancellation of the linear gravitational anomalies is a necessary condition for the consistency of the low-energy theory. Nonetheless, such a cancellation can be achieved here by including a singlet, left-handed fermion, N_L, that transforms in the same way as e_R under G. For the choice $p = 8$, adopted later in this section, N_L can develop a Majorana mass somewhat below M_* and decay rapidly to lighter states via Planck-suppressed operators. Including such a state does not affect the phenomenology of the model otherwise.

While it is not our goal to produce a theory of flavor, we note that the terms in Eq. (3.6) are of the type one expects in flavor models based on the Froggatt-Nielsen mechanism. Hence, integrating out the E fields leads to a higher-dimension operator

$$\mathcal{L} \supset \frac{1}{M^4} \overline{L}_L H \phi_E^4 e_R + \text{ h.c.}\,, \tag{3.7}$$

which provides an origin for the charged lepton Yukawa couplings. Choosing $\langle \phi_E \rangle / M \sim 0.3$ gives the correct scale for the tau lepton Yukawa coupling; the smaller, electron and muon Yukawa couplings may be accommodated by suitable choices of the undetermined couplings in Eq. (3.6). One might imagine that the remaining Yukawa hierarchies could be arranged by the imposition of additional symmetries, though we will not explore that possibility here.

We now introduce our dark matter candidate χ, a complex scalar field that transforms as

$$\chi \to \omega^4 \chi \quad \text{and} \quad \chi \to \eta^{-2} \chi \tag{3.8}$$

under $\mathbb{Z}_p \times \mathbb{Z}_q$. We assume that all the nonvanishing powers of ω and η shown in Eqs. (3.3), (3.4) and (3.8) are nontrivial, which requires that $p > 4$ and $q > 2$. Then, there are no renormalizable interactions involving a single χ field (or its conjugate) and two fermionic fields that could lead to dark matter decay. However, non-renormalizable, Planck-suppressed operator provide the desired effect. The lowest-order, Planck-suppressed correction to Eqs. (3.6) that involves a single χ field is the unique dimension-six operator

$$\Delta\mathcal{L}_e = \frac{1}{M_*^2} \chi\, \overline{E}_L^{(1)} \phi_D^2\, e_R + \text{ h.c.} \tag{3.9}$$

Including Eq. (3.9) and again integrating out the heavy, vector-like states, one obtains a new higher-dimension operator,

$$\mathcal{L}_{decay} = \frac{\phi_D^2}{M M_*^2}\,\chi \overline{L}_L H e_R + \text{ h.c.}, \tag{3.10}$$

which leads to dark matter decay. For $m_\chi \sim 3$ TeV (compatible qualitatively with fits to the PAMELA and Fermi-LAT data), a lifetime of 10^{26} seconds is obtained when

$$\frac{\langle \phi_D \rangle^2}{M_*^2}\frac{\langle H \rangle}{M} \sim 1 \times 10^{-26}\,. \tag{3.11}$$

For our operator expansion to be sensible, we require $\langle \phi_D \rangle < M$; however, we also do not want a proliferation of wildly dissimilar physical scales, if this can be avoided. Interestingly, if we choose M to be the geometric mean of $\langle H \rangle$ and M_*, one finds

$$M = 2 \times 10^{10}\text{ GeV}, \quad \langle \phi_E \rangle = 0.3\,M, \quad \langle \phi_D \rangle = 0.1\,M\,, \tag{3.12}$$

which meets our aesthetic requirements. Standard model quark and neutral lepton masses are unaffected by the discrete symmetry of our model, by construction. Light neutrino masses arise via a conventional see-saw mechanism, and it is possible to obtain a right-handed neutrino mass scale $M_R \approx M$, so that all the heavy leptons appear at a comparable scale. Assuming that the largest neutrino squared mass is comparable to $\Delta m_{32}^2 = 2.43 \times 10^{-3}$ eV^2, as suggested by atmospheric neutrino oscillations [5], then this possibility is obtained if the overall scale of the Yukawa coupling matrix that appears in the neutrino Dirac mass term is of the same order as the charm quark Yukawa coupling. This scenario is depicted in Fig. 3.1. In this case, the theory is characterized by three fundamental scales: the Planck scale, an intermediate scale (associated with charged lepton flavor and right-handed neutrino masses), and the TeV-scale. Symmetry-breaking vevs appear within a factor of $\lesssim 10$ below the latter two. Of course, the right-handed neutrino scale need not be linked

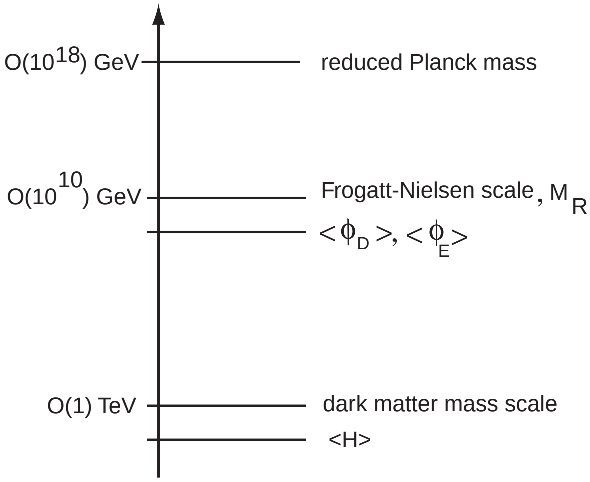

FIG. 3.1: A possible choice for the mass scales in the theory. Symmetry breaking vevs appear within approximately an order of magnitude of the lower two scales.

with the scale at which the charged lepton Yukawa couplings are generated; this is simply one of many viable possibilities that depend on choices of the free parameters of the model.

Finally, we return to the discrete symmetry group $G = \mathbb{Z}_p \times \mathbb{Z}_q$. We have noted that the structure of the theory that we have described is obtained for $p > 4$ and $q > 2$, but this does not take into account an important additional constraint: there must be no Planck-suppressed operators involving couplings between the various scalar fields in the theory that can lead to other dark matter decay channels that are either (i) too fast or (ii) too hadronic. For example, the choice $p = 5$ and $q = 3$, allows the renormalizable G-invariant operator $\chi \phi_E \phi_D^\dagger$, which leads to mixing, for example, between the χ and ϕ_E fields; the latter couples to two standard model leptons via the operator in Eq. (3.7), leading to a disastrously large decay rate. We find that all unwanted operators are sufficiently suppressed if we take $p = 8$ and $q = 4$, that is

$$G_I = \mathbb{Z}_8 \times \mathbb{Z}_4 \, . \tag{3.13}$$

The lowest-order combination of scalar fields that is invariant under G_I, as well as the standard model gauge group, is

$$\frac{1}{M_*^3}\chi\,\phi_D^2\,\phi_E^4\,, \tag{3.14}$$

Suppression by *three* factors of the Planck scale is more than sufficient to suppress any operators that are generated when the ϕ_E and ϕ_D fields are integrated out of the theory, or that may be constructed from products of Eq. (3.14) with any G_I-singlet, gauge-invariant combination of standard model fields. It is straightforward to confirm that the alternative choice

$$G_{II} = \mathbb{Z}_8 \times \mathbb{Z}_5\,, \tag{3.15}$$

is also viable, by similar arguments. The difference between the symmetry groups G_I and G_{II} is that the former allows two types of dark matter mass terms: $\chi^2 + \text{h.c.}$ and $\chi^\dagger\chi$. This leads to a mass splitting between the two real scalar components of χ, so that the lighter is the dark matter candidate. The choice G_{II} forbids the χ^2 mass terms, so that the dark matter consists of particles and anti-particles associated with the original complex scalar field. We note that in this theory, the renormalizable interactions involving χ have an accidental $\text{U}(1)_\chi$ global symmetry which would lead to dark matter stability in the absence of the Planck-suppressed effects. The analysis that we present in the following sections is somewhat simplified by the choice of G_{II}, which we adopt henceforth.

3.3 Cosmic Ray Spectra

In this section, we investigate the cosmic ray $e^\pm$ and proton/antiproton spectra of our model. Our treatment of cosmic ray propagation follows that of Ref. [51]. We show that model parameters may be chosen to accommodate the positron excess and the rising electron-positron flux observed by the PAMELA and Fermi-LAT experiments, respectively.

In Eq. (3.10), we identified the operator responsible for dark matter decays. More explicitly, this operator may be written

$$\mathcal{L}_{decay} = c_{ij} \frac{\langle \phi_D \rangle^2}{M M_*^2} \, \chi \overline{L}_L^i H e_R^j + \text{ h.c.}, \tag{3.16}$$

where i and j are generation indices, and c_{ij} represents unknown order-one coefficients. Different choices for the couplings c_{ij} will lead, in principle, to different cosmic ray spectra. To simplify the analysis, we focus on two possibilities: In the lepton mass eigenstate basis, the fermions appearing in the decay operators are either (*i*) muons exclusively, or (*ii*) taus exclusively. We will find that either of these choices is consistent with the data, even though we have not fully exploited the parametric freedom available in the c_{ij}. This is sufficient to demonstrate the viability of our model. The remaining factors in the operator coefficient are chosen to obtain the desired dark matter lifetime, as we discussed in the previous section.

In unitary gauge, the operator (3.16) can be be expanded

$$\mathcal{L}_{decay} = \frac{1}{\sqrt{2}} g_{ij} (v_{ew} + h) \, \chi \overline{e}_L^i \, e_R^j + \text{ h.c.}, \tag{3.17}$$

where h is the standard model Higgs field, which we will assume has a mass of 117 GeV, $v_{ew} = 246$ GeV, and $g_{ij} \equiv c_{ij} \langle \phi_D \rangle^2 / (M M_*^2)$. The term proportional to the Higgs vev leads to the two-body decay $\chi \to \ell^+ \ell^-$, for $\ell = \mu$ or τ, while the remaining term contributes to $\chi \to \ell^+ \ell^- h$. We take both of these decay channels into account in our numerical analysis. The final state particles in these primary decays will subsequently decay. The electrons, positrons, protons and antiprotons that are produced must be added to expected astrophysical backgrounds to predict the spectra at experiments like PAMELA and Fermi-LAT.

Electrons and positrons that are produced in dark matter decays must propagate through the Milky Way before reaching the Earth. In order to determine the observed fluxes, one must model this propagation. The transport equation for electron and positrons is given by

$$0 = \nabla \cdot [K(E,\vec{r})\nabla f_{e^\pm}] + \frac{\partial}{\partial E}[b(E,\vec{r}) f_{e^\pm}] + Q_{e^\pm}(E,\vec{r}), \tag{3.18}$$

where $f_{e^\pm}(E,\vec{r},t)$ is the number density of electron or positrons per unit energy, $K(E,\vec{r})$ is the diffusion coefficient and $b(E,\vec{r})$ is the energy loss rate. We assume the MED propagation model described in Ref. [148]. The diffusion coefficient and the energy loss rate are assumed to be spatially constant throughout the diffusion zone and are given by

$$K(E,\vec{r}) = 0.0112\epsilon^{0.70}\ \mathrm{kpc}^2/\mathrm{Myr} \tag{3.19}$$

and

$$b(E,\vec{r}) = 10^{-26}\epsilon^2\ \mathrm{GeV/s}\,, \tag{3.20}$$

where $\epsilon = E/1$ GeV. The last term in Eq. (3.18) is the source term given by

$$Q(E,\vec{r}) = \frac{\rho(\vec{r})}{M_\chi \tau_\chi}\frac{dN}{dE}, \tag{3.21}$$

where M_χ is the dark matter mass and τ_χ is the dark matter lifetime. In models like ours, where the dark matter can decay via more than one channel, the energy spectrum dN/dE is given by

$$\frac{dN}{dE} = \sum_i \frac{\Gamma_i}{\Gamma} \left(\frac{dN}{dE}\right)_i , \tag{3.22}$$

where Γ_i/Γ is the branching fraction and $(dN/dE)_i$ is the electron-positron energy spectrum of the i^{th} decay channel. We use PYTHIA [149] to determine the $(dN/dE)_i$. For the dark matter density, $\rho(\vec{r})$, we adopt the spherically symmetric Navarro-Frenk-White halo density profile [150]

$$\rho(r) = \frac{\rho_0}{(r/r_c)[1 + (r/r_c)]^2} , \tag{3.23}$$

with $\rho_0 \simeq 0.26$ GeV/cm^3 and $r_c \simeq 20$ kpc. The solutions to the transport equation are subject to the boundary condition $f_{e^\pm} = 0$ at the edge of the diffusion zone, a cylinder of half-height $L = 4$ kpc and radius $R = 20$ kpc measured from the galactic center.

The solution of the transport equation can be written

$$f_{e^\pm}(E) = \frac{1}{M_\chi \tau_\chi} \int_0^{M_\chi} dE' G_{e^\pm}(E, E') \frac{dN_{e^\pm}(E')}{dE'}, \tag{3.24}$$

where $G_{e^\pm}(E, E')$ is a Green's function, whose explicit form can be found in Ref. [151]. The interstellar flux then follows immediately from

$$\Phi_{e^\pm}^{DM} = \frac{c}{4\pi} f_{e^\pm}(E). \tag{3.25}$$

We adopt a parameterization of the interstellar background fluxes given in Ref. [51]:

$$\Phi_{e^-}^{bkg}(E) = \left(\frac{82.0\epsilon^{-0.28}}{1 + 0.224\epsilon^{2.93}}\right) \text{ GeV}^{-1}\text{m}^{-2}\text{s}^{-1}\text{sr}^{-1}, \tag{3.26}$$

$$\Phi^{bkg}_{e^+}(E) = \left(\frac{38.4\epsilon^{-4.78}}{1+0.0002\epsilon^{5.63}} + 24.0\epsilon^{-3.41}\right)\ \mathrm{GeV}^{-1}\mathrm{m}^{-2}\mathrm{s}^{-1}\mathrm{sr}^{-1}. \tag{3.27}$$

Finally, the flux at the top of the earth's atmosphere, $\Phi^{TOA}_{e^\pm}$, is corrected by solar modulation effects [51],

$$\Phi^{TOA}_{e^\pm}(E_{TOA}) = \frac{E^2_{TOA}}{E^2_{IS}}\Phi^{IS}_{e^\pm}(E_{IS})\,, \tag{3.28}$$

where $E_{IS} = E_{TOA} + |e|\phi$, and $|e|\phi = 550$ MeV. E_{IS} and E_{TOA} are the energy of positron/electron at the heliospheric boundary and at the top of atmosphere, respectively.

The total electron and positron flux is determined by

$$\Phi^{tot}(E) = \Phi^{DM}_{e^-}(E) + \Phi^{DM}_{e^+}(E) + k\Phi^{bkg}_{e^-}(E) + \Phi^{bkg}_{e^+}(E), \tag{3.29}$$

where k is a free parameter that determines the normalization of the primary electron flux background. The positron excess is given by

$$PF(E) = \frac{\Phi^{DM}_{e^+}(E) + \Phi^{bkg}_{e^+}(E)}{\Phi^{tot}(E)}. \tag{3.30}$$

The results of our analysis are presented in Figs. 3.2 and 3.3. In the case where the dark matter decays only to $\mu^+\mu^-$ and $\mu^+\mu^- h$, we find good agreement with the data for $\tau_\chi = 1.8 \times 10^{26}$ s and $M_\chi = 2.5$ TeV. In this case, the branching fraction to the two-body decay mode is 90.2%. In the case where the decay is to $\tau^+\tau^-$ and $\tau^+\tau^- h$ only, our best results are obtained for $\tau_\chi = 9.0 \times 10^{25}$ s and $M_\chi = 5$ TeV, corresponding to a two-body branching fraction of 69.6%. In all these results, the background electron flux parameter k is set to 0.88, following Ref. [151].

Since the dark matter decays in our model include the production of standard model Higgs bosons in the final state, it is worthwhile to check that subsequent

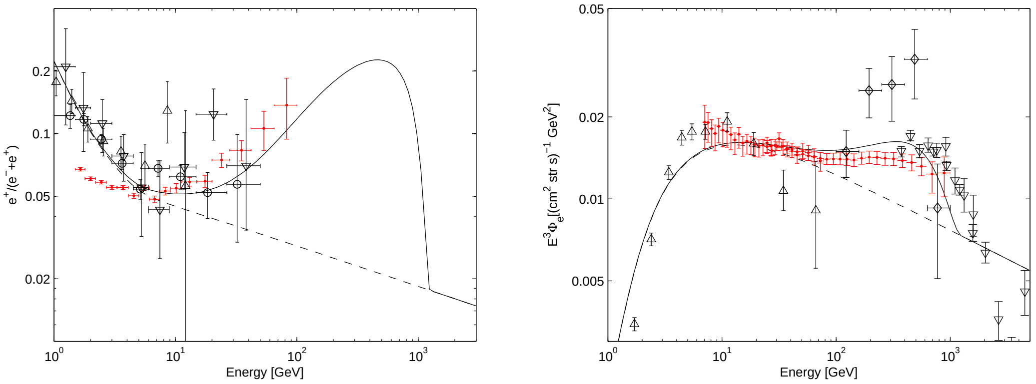

FIG. 3.2: *Left panel*: The positron excess for dark matter decaying into $\mu^+\mu^-$ and $\mu^+\mu^- h$. The dark matter mass is 2.5 TeV and lifetime 1.8×10^{26} s; the branching fraction to the two-body decay mode is 90.2%. The dashed line represents the background and the solid line represents the background plus dark matter signal. Data from the following experiments are shown: PAMELA [7] (solid dots), HEAT [11] (○), AMS-01 [12] (▽), and CAPRICE [13] (△). *Right panel*: The corresponding graph for the total electron and positron flux. Data from the following experiments are shown: Fermi-LAT [8] (solid dots), HESS [14] (▽), PPB-BETS [15] (◇), HEAT [16] (△).

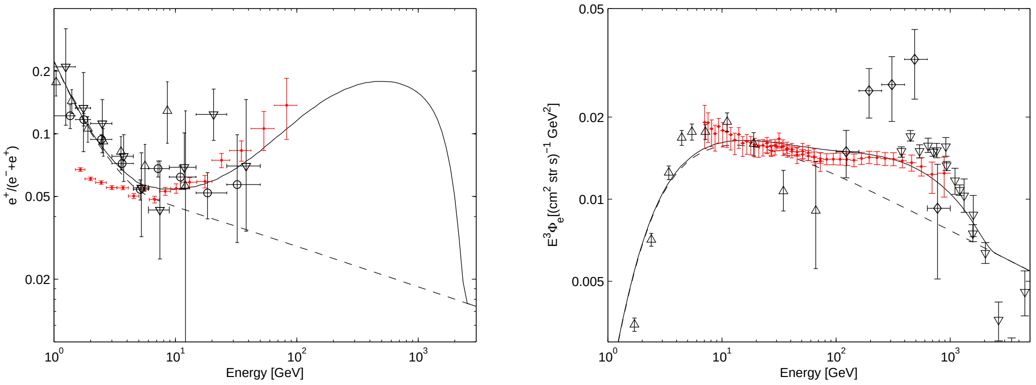

FIG. 3.3: *Left panel*: The positron excess for dark matter decaying into $\tau^-\tau^+$ and $\tau^-\tau^- h$. The dark matter mass is 5.0 TeV and lifetime 9.0×10^{25} s; the branching fraction to the two-body decay mode is 69.6% . *Right panel*: The corresponding graph for the total electron and positron flux.

Higgs decays do not lead to an excess of cosmic ray antiprotons, in conflict with the experimental data. This will not be the case at our two benchmark parameter choices since the branching fraction to the three-body decay mode is suppressed compared to the two-body mode. The procedure for computing the cosmic ray antiproton flux is similar to that of the cosmic ray electrons and positrons. The transport equation for antiproton propagation within the Milky Way is given by

$$0 = \nabla \cdot \Big[K(T,\vec{r})\nabla f_{\bar{p}} - \vec{V}_c(\vec{r}) f_{\bar{p}}\Big] + Q_{\bar{p}}(T,\vec{r}) \tag{3.31}$$

where T is the antiproton kinetic energy, $\vec{V}_c(\vec{r})$ is the convection velocity, and the source term $Q_{\bar{p}}$ has the same form as Eq. (3.21). As in the case of $e^{\pm}$ propagation, the antiproton number density can be expressed in terms of a Green's function

$$f_{\bar{p}}(T) = \frac{1}{M_\chi \tau_\chi} \int_0^{T_{max}} dT' G_{\bar{p}}(T,T') \frac{dN_{\bar{p}}(T')}{dT'}, \tag{3.32}$$

where $G_{\bar{p}}(T,T')$ can be found in Ref. [151]. The relation between the antiproton number density and the interstellar flux of antiproton is given by

$$\Phi_{\bar{p}}^{DM}(T) = \frac{v}{4\pi} f_{\bar{p}}(T)\,, \tag{3.33}$$

where v is the antiproton velocity. We also take account the solar modulation effect on the antiproton flux at the top of atmosphere, $\Phi_{\bar{p}}^{TOA}$, which is given by

$$\Phi_{\bar{p}}^{TOA}(T_{TOA}) = \left(\frac{2m_p T_{TOA} + T_{TOA}^2}{2m_p T_{IS} + T_{IS}^2}\right) \Phi_{\bar{p}}^{IS}(T_{IS}), \tag{3.34}$$

where T_{IS} and T_{TOA} are the antiproton kinetic energies at the heliospheric boundary and at the top of atmosphere, respectively, with $T_{IS} = T_{TOA} + |e|\phi$. For the proton and antiproton flux, we adopt the background given in Ref. [152].

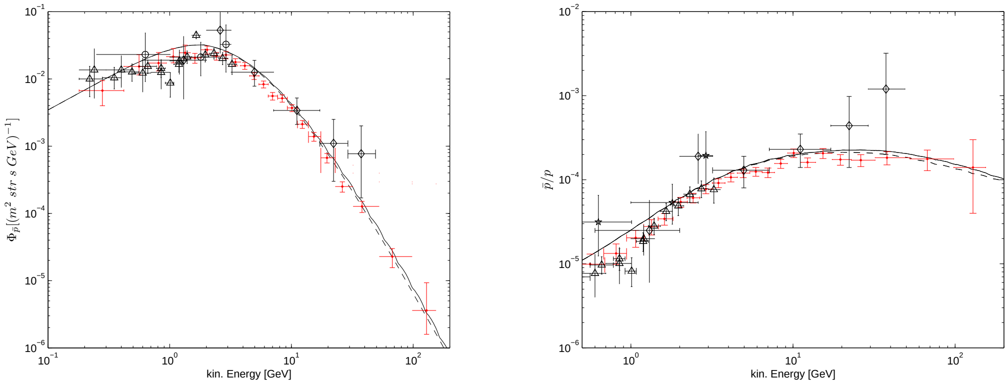

FIG. 3.4: *Left panel*: The antiproton flux for dark matter decaying into $\mu^+\mu^-$ and $\mu^+\mu^- h$. The dark matter mass is 2.5 TeV and lifetime 1.8×10^{26} s; the branching fraction to the two-body decay mode is 90.2%. The dashed line represents the background and the solid line represents the background plus dark matter signal. Data from the following experiments are shown: PAMELA [6] (solid dots), WiZard/CAPRICE [17] ($\diamond$), and BESS [18] ($\triangle$). *Right panel*: The corresponding graph for the antiproton to proton ratio. Data from the following experiments are shown: PAMELA [6] (solid dots), IMAX [19] ($\star$), CAPRICE [17] ($\diamond$) and BESS [18] ($\triangle$).

Again assuming the MED propagation model Ref. [148], we compute the antiproton flux and the antiproton to proton ratio for dark matter decays to $\mu^-\mu^+$ and $\mu^-\mu^+ h$, shown in Fig. 3.4, and for decays to $\tau^-\tau^+$ and $\tau^-\tau^- h$, shown in Fig. 3.5. We see that in both cases, the antiproton excess above the predicted background curves is small and consistent with the data shown from a variety of experiments.

3.4 Relic Density and Direct Detection

In this section, we show that the model we have presented can provide the correct dark matter relic density while remaining consistent with the direct detections bounds. The part of the Lagrangian that is relevant for computing the relic density, as well as the dark matter-nucleon elastic scattering cross section, is the coupling between χ and standard model Higgs

$$\mathcal{L} \supset \lambda \chi^\dagger \chi H^\dagger H. \tag{3.35}$$

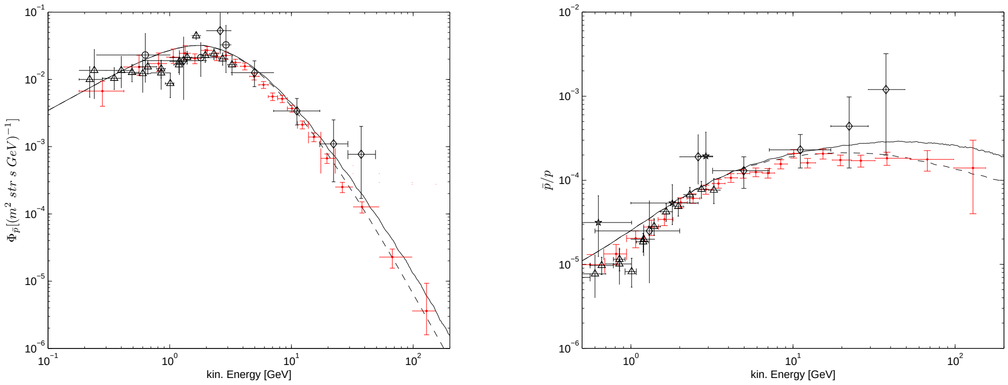

FIG. 3.5: *Left panel*: The antiproton flux for dark matter decaying into $\tau^-\tau^+$ and $\tau^-\tau^- h$. The dark matter mass is 5.0 TeV and lifetime 9.0×10^{25} s; the branching fraction to the two-body decay mode is 69.6%. *Right panel*: The corresponding graph for the antiproton to proton ratio.

In unitary gauge, this can be expanded

$$\mathcal{L} \supset \frac{\lambda}{2}\left(\chi^\dagger\chi\, h^2 + 2\, v_{ew}\, \chi^\dagger\chi\, h\right). \tag{3.36}$$

As a consequence of Eq. (3.36), χ and $\overline{\chi}$ pairs may annihilate into a variety of standard model particles. The leading diagrams are shown in Fig. 3.6. The cross section for annihilations into fermions is given by

$$\sigma_{\chi\bar{\chi}\to f\bar{f}} = \frac{N_c}{8\pi}\frac{\lambda^2 m_f^2}{s\,(s-m_h^2)^2}\sqrt{\frac{\left(s-4m_f^2\right)^3}{s-4m_\chi^2}}, \tag{3.37}$$

where N_c is the number of fermion colors ($N_c = 1$ for leptons and $N_c = 3$ for quarks) and m_f is the fermion mass. The cross sections for annihilations into W and Z bosons are given by

$$\sigma_{\chi\bar{\chi}\to ZZ} = \frac{\lambda^2}{8\pi}\frac{m_Z^4}{s\,(s-m_h^2)^2}(3 - \frac{s}{m_Z^2} + \frac{s^2}{4m_Z^4})\sqrt{\frac{s-4m_Z^2}{s-4m_\chi^2}}, \tag{3.38}$$

$$\sigma_{\chi\bar{\chi}\to W^+W^-} = \frac{\lambda^2}{4\pi}\frac{m_W^4}{s\,(s-m_h^2)^2}(3 - \frac{s}{m_W^2} + \frac{s^2}{4m_W^4})\sqrt{\frac{s-4m_W^2}{s-4m_\chi^2}}, \tag{3.39}$$

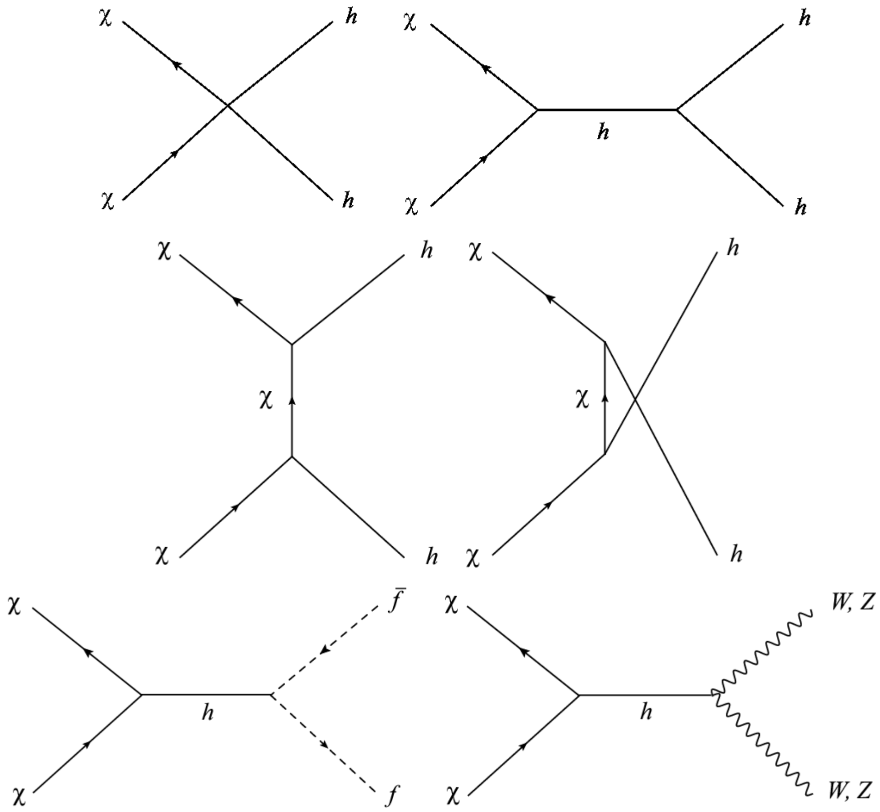

FIG. 3.6: Dark matter annihilation diagrams.

where m_W (m_Z) is the mass of W (Z) boson. In the case where the dark matter annihilates into a pair of standard model Higgs bosons, we can safely ignore the t- and u-channel diagrams since the typical momenta are much smaller than m_χ at temperatures near freeze out. Hence, the cross section is given by

$$\sigma_{\chi\bar{\chi}\to hh} = \frac{\lambda^2}{32\pi\, s}\sqrt{\frac{s-4m_h^2}{s-4m_\chi^2}}\left(1+\frac{6m_h^2}{s-m_h^2}+\frac{9m_h^4}{(s-m_h^2)^2}\right). \tag{3.40}$$

The evolution of dark matter number density, n_χ, is governed by the Boltzmann equation

$$\frac{dn_\chi}{dt} + 3H(t)n_\chi = -\langle\sigma v\rangle[n_\chi^2 - (n_\chi^{EQ})^2], \tag{3.41}$$

where $H(t)$ is the Hubble parameter as a function of time and n_χ^{EQ} is the equilibrium number density. The thermally-averaged annihilation cross section, $\langle\sigma v\rangle$, can be calculated by evaluating the integral [97]

$$\langle\sigma v\rangle = \frac{1}{8m_\chi^4 T K_2^2(m_\chi/T)}\int_{4m_\chi^2}^{\infty}(\sigma_{tot})\,(s-4m_\chi^2)\sqrt{s}\,K_1(\sqrt{s}/T)\,ds\ , \tag{3.42}$$

where σ_{tot} is the total annihilation cross section and the K_i are modified Bessel functions of order i. We find the freeze out temperature, T_f, using the freeze-out condition [3]

$$\frac{\Gamma}{H(t_F)} \equiv \frac{n_\chi^{EQ}\langle\sigma v\rangle}{H(t_F)} \approx 1\ , \tag{3.43}$$

where equilibrium number density as a function of temperature is given by

$$n_\chi^{EQ} = \left(\frac{m_\chi T}{2\pi}\right)^{3/2} e^{-m_\chi/T}\,. \tag{3.44}$$

The Hubble parameter may be re-expressed as a function of temperature T

$$H = 1.66\, g_*^{1/2}\, T^2/m_{Pl}\,. \tag{3.45}$$

where g_* is the number of relativistic degrees of freedom and $m_{Pl} = 1.22 \times 10^{19}$ GeV is the Planck mass. It is customary to normalize the temperature with the dark matter mass, $x = m_\chi / T$. For the points in parameter space discussed below, we found that the freeze out happens when $x_f \approx 28$. The present dark matter density can be calculated using the relation

$$\frac{1}{Y_0} = \frac{1}{Y_f} + \sqrt{\frac{\pi}{45}} m_{Pl}\, m_\chi \int_{x_f}^{x_0} \frac{g_*^{1/2}}{x^2} \langle \sigma v \rangle \, dx \; , \tag{3.46}$$

where Y is the ratio of number to entropy density and the subscript 0 denotes the present time. The ratio of the dark matter relic density to the critical density ρ_c is given by $\Omega_D = 2\, Y_0 s_0 m_\chi / \rho_c$, where s_0 is the present entropy density, or equivalently

$$\Omega_D h^2 \approx 5.6 \times 10^8 \ \text{GeV}^{-1} \, Y_0 \, m_\chi \ \ . \tag{3.47}$$

Note that the factor of 2 included in the expression for Ω_D takes into account the contribution from χ particles and $\bar{\chi}$ antiparticles.

In the case $m_\chi = 2.5$ TeV, we find numerically that the dark matter-Higgs coupling $\lambda = 0.9$ in order that $\Omega_D h^2 = 0.1$. For $m_\chi = 5$ TeV, we find $\lambda = 1.8$. These order-one couplings are perturbative. One should keep in mind that the physics responsible for dark matter annihilations is not directly linked to the mechanism that we have proposed to account for dark matter decay; other contributions to the total annihilation cross section can easily be arranged. For example, if the Higgs sector includes mixing with a gauge singlet scalar S such that there is a scalar mass eigenstate near $2m_\chi$, then the annihilation through the s-channel exchange of this state can lead to a resonantly enhanced annihilation channel, as in the model of Ref. [120]. In this case, the correct relic density could be obtained for smaller λ than the values quoted above.

Finally, we confirm that the model does not conflict with bounds from searches for dark matter-nuclear recoil. In this case, the most relevant contribution comes from the interaction between the dark matter and quarks mediated by a t-channel Higgs exchange. The effective Lagrangian is given by

$$\mathcal{L} = -\frac{\lambda\, m_q}{m_h^2}\chi^\dagger \chi \bar{q} q. \tag{3.48}$$

Following Refs [100, 153], we can write an effective interaction between the nucleons and dark matter,

$$\mathcal{L} = -(f_p \chi^\dagger \chi \overline{p}\, p + f_n \chi^\dagger \chi \overline{n}\, n)\,, \tag{3.49}$$

where $f_N = m_N \mathcal{A}_N \lambda / m_h^2$, for $N = p$ or n. The coefficient $\mathcal{A}_N$ can be evaluated using the results of Ref. [100]; numerically, one finds $f_p \approx f_n \approx \mathcal{A}_N m_N \lambda / m_h^2$ with $\mathcal{A}_N \approx 0.35$. Given the effective dark matter-nucleon interaction, we find that the spin-independent cross section is given by

$$\sigma_{SI} = \frac{\lambda^2 \mathcal{A}_N^2}{4\pi} \frac{m_N^4}{m_h^4 (m_\chi + m_N)^2}. \tag{3.50}$$

For both of the cases discussed earlier, ($m_\chi = 2.5$ TeV, $\lambda = 0.9$) and ($m_\chi = 5$ TeV, $\lambda = 1.8$), we find $\sigma_{SI} \sim \mathcal{O}(10^{-45})$ cm^2. This is two orders of magnitude smaller than the strongest bounds, from CDMS [10], which range from $\sim 2 \times 10^{-43}$ cm^2 at $m_\chi = 1$ TeV to 2×10^{-42} cm^2 at $m_\chi = 10$ TeV.

3.5 Conclusions

Models of decaying dark matter require a plausible origin for the higher-dimension operators that lead to dark matter decays. The data from cosmic ray experiments like PAMELA and Fermi-LAT require that these operators involve lepton fields preferentially. We have shown how the desired higher-dimension operators may originate from Planck-suppressed couplings between a TeV-scale scalar dark matter particle χ and vector-like states at a mass scale M that is intermediate between the weak and Planck scales. The vector-like sector has the structure of a Froggatt-Nielsen model: charged lepton Yukawa couplings arise only after these states are integrated out and a discrete gauged Abelian flavor symmetry is broken. Couplings between χ and the standard model gauge-invariant combination $\bar{L}_L H e_R$ are then also generated, with coefficients of order $\langle\phi\rangle^2/(M_*^2\, M)$, where $\langle\phi\rangle$ is the scale at which the flavor symmetry is broken. Taking M and $\langle\phi\rangle$ near the geometric mean of the reduced Planck scale and the weak scale, $O(10^{10})$ GeV, leads to the desired dark matter lifetime. Neutrino masses can be generated via a conventional see-saw mechanism with the mass scale of right-handed neutrinos also near M. We pointed out that the symmetry structure of our model leads to an overall suppression factor multiplying the charged lepton Yukawa matrix, but does not constrain the standard model Yukawa textures otherwise. Hence, our framework is potentially compatible with a wide range of possible solutions to the more general problem of quark and lepton flavor in the standard model.

We presented the necessary PYTHIA simulations to confirm that our model can account for the anomalies observed in the cosmic ray experiments discussed earlier. The leading contribution to the primary cosmic ray electron and positron flux in our model comes from two-body decays, in which the Higgs field is set equal to its vev in the operator described above; the subleading three body decays, $\chi \to \ell^+\ell^- h^0$, are also possible. We have checked that these decay channels do not lead to an observable excess in the spectrum of cosmic ray antiprotons, since the cosmic ray antiproton flux is in agreement with astrophysical predictions.

Our model demonstrates that the desired lifetime and decay channels of TeV-scale scalar dark matter candidate can be the consequence of renormalizable physics at an intermediate lepton flavor scale and gravitational physics at M_*. This presents an alternative scenario to the one in which dark matter decay is a consequence of physics at a unification scale located somewhere between M and M_*.

CHAPTER 4

On the Cosmic-Ray Spectra of Three-Body Lepton-Flavor-Violating Dark Matter Decays[5]

4.1 Introduction

Cosmic rays have been studied extensively at various earth-, balloon- and satellite-based experiments. Recently, the PAMELA satellite has observed an unexpected rise in the cosmic-ray positron fraction from approximately 7 to 100 GeV [7]. This feature is not explained by the expected background from the secondary production of cosmic-rays positrons. Moreover, observations of the total flux of electrons and positrons by Fermi-LAT [62] and H.E.S.S. [47] also show an excess over the predicted background, up to an energy of $\sim$ 1 TeV. The presence of nearby pulsars

---

[5] This chapter was previously published in Phys. Lett. B704 (2011) 541.

could provide an astrophysical explanation for these observations [52, 64]. Nevertheless, more exotic scenarios remain possible. The annihilation of dark matter in the galactic halo to electrons and positrons provides one such possibility, though generic annihilation cross sections must be enhanced by a large boost factor in order to describe the data [65, 154]. Alternatively, the excess could be explained by a TeV-scale decaying dark matter candidate. (For example, see Ref. [84]; for a recent review, see Ref. [155].) In this scenario, fits to the cosmic-ray data indicate that the dark matter must decay primarily to leptons with a lifetime of $\mathcal{O}(10^{26})$ s.

While the thermal freeze-out of weakly-interacting, electroweak-scale dark matter can naturally lead to the desired relic density, this is not the only possible framework that can account for the present dark matter abundance. Recently proposed asymmetric dark matter models relate the baryon or lepton number densities to the dark matter number density, motivated by the fact that these quantities are not wildly dissimilar [35–38]. TeV-scale asymmetric dark matter models have been constructed, for example, in Refs. [36–38]. The asymmetry between dark matter particles and antiparticles can lead to differences in the primary cosmic-ray spectra of electrons and positrons, with potentially measurable consequences [156, 157]. Evidence for such charge asymmetric dark matter decays would disfavor the pulsar explanation of the $e^\pm$ excess [157]. In addition, charge asymmetric dark matter decays may allow one to discern whether dark matter decays are lepton-flavor-violating [158]. For example, the cosmic-ray spectra that one expects if dark matter decays symmetrically to $e^+\mu^-$ and $e^-\mu^+$ are indistinguishable from those obtained by assuming flavor-conserving decays to e^+e^- and $\mu^+\mu^-$ with equal branching fraction; the same is not true if the dark matter decays asymmetrically to $e^+\mu^-$ alone, 100% of the time.

Refs. [157] and [158] study the cosmic-ray $e^\pm$ spectra assuming a number of two-body charge-asymmetric dark matter decays, with the latter work focusing on lepton-flavor-violating modes. In this chapter, we extend this body of work to charge-asymmetric three-body decays and, in particular, to modes that violate lepton flavor. We assume a spin-1/2 dark matter candidate that decays via four-fermion contact interactions to two charged leptons and a light, stable neutral particle. For the present purposes, the latter could either be a standard model neutrino or a lighter dark matter component. Four-fermion interactions have a long history in the development of the weak interactions, and one can easily imagine that dark matter decays could be the consequence of operators of this form, generated by higher-scale physics. Moreover, the possible presence of a neutrino in the primary decay may lead to interesting signals at neutrino telescopes [159, 160]. Unlike the two-body decays already considered in the literature, the precise energy distribution of the decay products is affected by the Dirac matrix structure of these contact interactions, which is not known (unless a model is specified). By considering the most general possibilities, we show that different choices for the Dirac structure of the decay operators defined in Sec. 4.2 can be substantially compensated by different choices for the dark matter mass m_ψ and lifetime τ_ψ; while the best fit values of these parameters change, the predicted spectra are not dramatically altered. On the other hand, we find that the flavor structure of the decay operator has a more significant effect. Assuming various lepton-flavor-conserving and flavor-violating decay modes, we compute the resulting cosmic-ray spectra, performing χ^2 fits to the data to determine the optimal dark matter masses and lifetimes. Like Refs. [157, 158], we obtain predictions for these spectra at $e^\pm$ energies that are higher than those than can be probed accurately now. Future data from experiments like AMS-02 [161] may provide the opportunity to test these predictions, and evaluate them relative to other interpretations of the cosmic-ray positron excess.

This chapter is organized as follows. In the next section, we discuss the assumed form of the dark matter operators. In Sec. 4.3, we present the results of our numerical analysis and in Sec. 4.4, we discuss our results and directions for future work.

4.2 Four-Fermion Operators

We consider a spin-1/2 dark matter candidate ψ that decays to $\ell_i^+\ell_j^-\nu$ where i and j are generation indices and ν represents a light, neutral particle. We assume that ν is either a standard model neutrino or a secondary dark matter component that is much lighter than ψ and contributes negligibly to the relic density. In the present analysis, the exact nature of the light neutral state will be irrelevant since its effect on our results will come solely from kinematics. We focus on the simplest scenario, in which there are no additional decay channels involving the charge conjugate of ν, and consider the possible four-fermion operators that contribute to the decays of interest. We work directly with the operators that may appear after the standard model electroweak gauge symmetry is spontaneously broken; for any operator found to have phenomenologically desirable properties, one may easily construct a gauge-invariant origin after the fact. Note that the production of a neutrino in the primary decay may have interesting phenomenological consequences (see, for example, Ref. [159, 160]), which provides a separate motivation for our three-fermion final state. Once this choice is made, the dark matter spin must be 1/2 if the underlying theory is renormalizable [6].

The problem of parametrizing an unknown decay amplitude of one spin-1/2 particle to three distinct spin-1/2 decay products was encountered in the study of muon decay, before the standard model was well established. The most general

---

[6] For a model with flavor-conserving, three-body decays involving a final-state gravitino, see Ref. [162].

decay amplitude $\mathcal{M}$ can be parametrized by [163]

$$i\mathcal{M} = ig\sum_i \left[\overline{u}(p_0)O_i u_\psi\right]\,\left[\overline{u}(p_-)O_i(c_i + c_i'\gamma^5)v(p_+)\right]\;, \tag{4.1}$$

where $p_\pm$ and p_0 are the momenta of the decay products, labeled according to their electric charge, and the O_i, $i = 1\cdots 5$ are elements of the set of linearly independent matrices

$$O = \{1,\, \gamma^\mu,\, \sigma^{\mu\nu},\, \gamma^\mu\gamma^5,\, \gamma^5\}\,. \tag{4.2}$$

The c_i and c_i' are complex coefficients. Terms involving the contraction of spinor indices that link different pairs of spinor wave functions can be recast in the form of Eq. (4.1) via Fierz transformations. Since the final state particles are much lighter than the dark matter candidate (which is at the TeV scale), we can safely neglect their masses.

Since the neutral final state particle is stable, the energy spectra of electrons and positrons that are observed at cosmic-ray observatories are determined by the energy spectra of the the charged leptons, ℓ^+ and ℓ^-, that are produced in the primary decay; this follows from the differential decay distribution

$$\frac{1}{\Gamma}\frac{d^2\Gamma}{dE_0 dE_\pm} = \frac{1}{64\pi^3 m_\psi}\langle|\mathcal{M}|^2\rangle\,, \tag{4.3}$$

where $\langle|\mathcal{M}|^2\rangle$ is the spin-summed/averaged squared amplitude. We evaluate this quantity exactly from Eq. (4.1) using FeynCalc [164], and compute the $\ell^\pm$ energy distribution by integrating over the neutral lepton energy E_0. We find that the result contains terms quadratic and cubic in $E_\pm$; however, since the distribution must be normalized to unity, the result has the following simple parametrization:

$$\frac{1}{\Gamma}\frac{d\Gamma}{dE_\pm} = \frac{1}{m_\psi}\frac{E_\pm^2}{m_\psi^2}\left[\xi_\pm + \left(64 - \frac{8}{3}\xi_\pm\right)\frac{E_\pm}{m_\psi}\right]\,. \tag{4.4}$$

The requirement that this expression remains positive over the kinematically accessible range $0 \leq E_\pm \leq m_\psi/2$ restricts the parameters ξ_+ and ξ_- to fall within the range

$$0 \leq \xi_\pm \leq 96\,. \tag{4.5}$$

The $\xi_\pm$ are generally complicated functions of the operator coefficients c_i and c_i'; we provide these in the appendix. In the present analysis, however, the exact relations are not particularly important; by leaving m_ψ and τ_ψ as fitting parameters, one obtains very similar predicted spectra, independent of the choice of the $\xi_\pm$. The fact that *some* solution exists for any desired Dirac structure of the underlying four-fermion operator makes it potentially easier to construct explicit models. Though we reserve the task of model-building to future work, it is worth noting, for example, that the operator

$$O_{ij}^{RR} \equiv \overline{\nu}\gamma^\mu(1+\gamma^5)\psi\bar{\ell}_i\gamma_\mu(1+\gamma^5)\ell_j\,, \tag{4.6}$$

corresponding to $\xi_+ = 96$ and $\xi_- = 48$, is a particularly interesting choice, since it is already gauge invariant under the standard model gauge group and may provide a simple starting point for constructing a plausible ultraviolet completion.

We computed the electron and positron spectra using PYTHIA [165], taking into account the energy distributions of the primary leptons ℓ^+ and ℓ^-. As a cross check, we have written code that incorporates Eq. (4.3), computed directly from a choice of the underlying four-fermion operator, as well as code that incorporates only the distributions Eq. (4.4), for the corresponding values of ξ_+ and ξ_-. We have also compared output from different versions of our code, based on PYTHIA 6.4 and PYTHIA 8.1, respectively[7]. Results from these different approaches were found to be agreement.

---

[7] Note that PYTHIA 6.4 does not automatically take into account neutron decay, which we include by modifying the program's decay table.

4.3 Cosmic-Ray Spectra

To compute the relevant cosmic-ray fluxes, one must take into account that electrons and positrons produced in dark matter decays must propagate through the galaxy before reaching earth. While modeling this propagation is now standard in the literature on decaying dark matter scenarios, we briefly summarize our approach so that our discussion is self contained and our assumptions are manifest.

4.3.1 Cosmic-Ray Propagation

Let $\mathbf{r}$ be a position with respect to the center of the Milky Way Galaxy. We assume the spherically symmetric Navarro-Frenk-White dark matter halo density profile [150]

$$\rho(r) = \rho_0 \frac{r_c^3}{r(r+r_c)^2} \,, \tag{4.7}$$

where $\rho_o \simeq 0.26\ \mathrm{GeV/cm^3}$ and $r_c \simeq 20$ kpc. The production rate of electrons/positrons per unit energy and per unit volume is then given by

$$Q(E,r) = \frac{\rho(r)}{m_\psi}\left(\frac{1}{\tau_\psi}\frac{dN_{e^\pm}}{dE}\right) \,, \tag{4.8}$$

where m_ψ and τ_ψ are the dark matter mass and lifetime, respectively, and $dN_{e^\pm}/dE$ is the energy spectrum of electrons/positrons produced in the dark matter decay. Let $f_{e^\pm}(E,\mathbf{r})$ be the number density of electrons/positrons per unit energy. Then, $f_{e^\pm}(E,\mathbf{r})$ satisfies the transport equation [166, 167]

$$0 = K(E)\nabla^2 f_{e^\pm}(E,\mathbf{r}) + \frac{\partial}{\partial E}\left[b(E) f_{e^\pm}(E,\mathbf{r})\right] + Q(E,r). \tag{4.9}$$

We assume the MED propagation model described in Ref. [148, 168] for which

$$K(E) = 0.0112\epsilon^{0.70}\,\mathrm{kpc}^2/\mathrm{Myr} \tag{4.10}$$

and

$$b(E) = 10^{-16}\epsilon^2\,\mathrm{GeV/s}\,, \tag{4.11}$$

where $\epsilon = E/(1\,\mathrm{GeV})$. The diffusion zone is approximated as a cylinder with half-height $L = 4$ kpc and radius $R = 20$ kpc. We require $f_{e^\pm}(E, \mathbf{r})$ to vanish at the boundary of this zone. The solution at the heliospheric boundary is then given by [151]

$$f_{e^\pm}(E) = \frac{1}{m_\psi \tau_\psi} \int\limits_0^{m_\psi} dE'\, G_{e^\pm}(E, E') \frac{dN_{e^\pm}(E')}{dE'}. \tag{4.12}$$

The Green's function, $G_{e^\pm}(E, E')$, can be found in Ref. [151]. The interstellar flux of electrons/positrons created in dark matter decays is then given by

$$\Phi_{e^\pm}^{\mathrm{DM}}(E) = \frac{c}{4\pi} f_{e^\pm}(E)\,, \tag{4.13}$$

where c is the speed of light.

For the background fluxes, we assume the Model 0 proposed by the Fermi collaboration [51, 169]:

$$\Phi_{e^-}^{\mathrm{bkg}}(E) = \left(\frac{82.0\epsilon^{-0.28}}{1 + 0.224\epsilon^{2.93}}\right)\,\mathrm{GeV}^{-1}\mathrm{m}^{-2}\mathrm{s}^{-1}\mathrm{sr}^{-1} \tag{4.14}$$

and

$$\Phi_{e^+}^{\mathrm{bkg}}(E) = \left(\frac{38.4\epsilon^{-4.78}}{1 + 0.0002\epsilon^{5.63}} + 24.0\epsilon^{-3.41}\right)\,\mathrm{GeV}^{-1}\mathrm{m}^{-2}\mathrm{s}^{-1}\mathrm{sr}^{-1}\,, \tag{4.15}$$

where, as before, $\epsilon = E/(1\,\mathrm{GeV})$.

At the top of the Earth's atmosphere, these fluxes must be corrected to account for the effects of solar modulation [51]. The flux at the top of the atmosphere (TOA) is related to the interstellar (IS) flux by

$$\Phi_{e^\pm}^{\mathrm{TOA}}(E_{\mathrm{TOA}}) = \frac{E_{\mathrm{TOA}}^2}{E_{\mathrm{IS}}^2} \Phi_{e^\pm}^{\mathrm{IS}}(E_{\mathrm{IS}})\,, \tag{4.16}$$

where $E_{\mathrm{IS}} = E_{\mathrm{TOA}} + |e|\phi_F$ and $|e|\phi_F = 550\,\mathrm{MeV}$.

The total electron-positron flux is given by

$$\Phi_e^{\mathrm{tot}} = \Phi_{e^-}^{\mathrm{DM}}(E) + \Phi_{e^+}^{\mathrm{DM}}(E) + k\Phi_{e^-}^{\mathrm{bkg}}(E) + \Phi_{e^+}^{\mathrm{bkg}}(E)\,, \tag{4.17}$$

where k is a free parameter which determines the normalization of the background electron flux. In our numerical analysis, we find that the best fit values of k never deviate by more that two percent from 0.84 and that fixing k at this value has a negligible effect on the goodness of fits and our predicted spectra. Therefore, we set $k = 0.84$ henceforth to reproduce the cosmic-ray spectra at low energies. The positron fraction is given by

$$\mathrm{PF}(E) = \frac{\Phi_{e^+}^{\mathrm{DM}}(E) + \Phi_{e^+}^{\mathrm{bkg}}(E)}{\Phi_e^{\mathrm{tot}}}. \tag{4.18}$$

4.3.2 Results

In the propagation model described above, the only remaining undetermined quantities are m_ψ, τ_ψ, dN_{e^+}/dE and dN_{e^-}/dE. The electron and positron energy spectra, dN_{e^+}/dE and dN_{e^-}/dE, are determined by m_ψ and by a set of parameters which we describe in the following paragraph.

We consider dark matter decays of the form $\psi \to \ell_i^+ \ell_j^- \nu$ where $\ell_i^\pm$ is a charged lepton of the i^{th} generation. There are nine such decay channels, and we require

$$\sum_{i,j} B(\ell_i^+ \ell_j^- \nu) = 1\,, \tag{4.19}$$

where the $B(\ell_i^+ \ell_j^- \nu)$ are branching fractions. For decays involving more than one channel,

$$\frac{dN_{e^\pm}}{dE} = \sum_{i,j} B(\ell_i^+ \ell_j^- \nu) \left(\frac{dN_{e^\pm}}{dE} \right)_{ij}\,, \tag{4.20}$$

where $(dN_{e^\pm}/dE)_{ij}$ is the electron/positron energy spectrum for $\psi \to \ell_i^+ \ell_j^- \nu$. In Sec. 4.2, we showed that the energy spectra of the charged leptons in the decay $\psi \to \ell_i^+ \ell_j^- \nu$ are characterized by the ordered pair (ξ_+, ξ_-), where $0 \leq \xi_\pm \leq 96$. We also showed that $(dN_{e^\pm}/dE)_{ij}$ is entirely determined by m_ψ and (ξ_+, ξ_-). For decays involving more than one decay channel (e.g., $\psi \to e^+ \mu^- \nu$ and $\psi \to \mu^+ \tau^- \nu$), we assume a constant (ξ_+, ξ_-). Then, since the branching fractions are subject to Eq. (4.19), we can determine dN_{e^+}/dE and dN_{e^-}/dE by specifying m_ψ, ξ_+, ξ_- and eight of the nine branching fractions.

To summarize, when we use the cosmic-ray propagation model described in the previous subsection, the resulting positron fraction and total electron-positron flux measured at the top of the Earth's atmosphere are determined by 12 parameters: m_ψ, τ_ψ, ξ_+, ξ_- and eight of the nine branching fractions.

For each of the decay scenarios considered below, we fixed (ξ_+, ξ_-) and the branching fractions and then performed a χ^2 fit to the PAMELA, Fermi LAT, H.E.S.S. 2008 and H.E.S.S. 2009 data with m_ψ and τ_ψ as fitting parameters. We allowed m_ψ to vary in increments of 500 GeV, and we allowed τ_ψ to vary in increments of 0.1×10^{26} s. We consider the range $E > 10$ GeV, where the effects of a TeV-scale dark matter candidate are relevant. Where the high-energy and low-energy Fermi data overlap, we have plotted only the high-energy data. (We omit from our figures

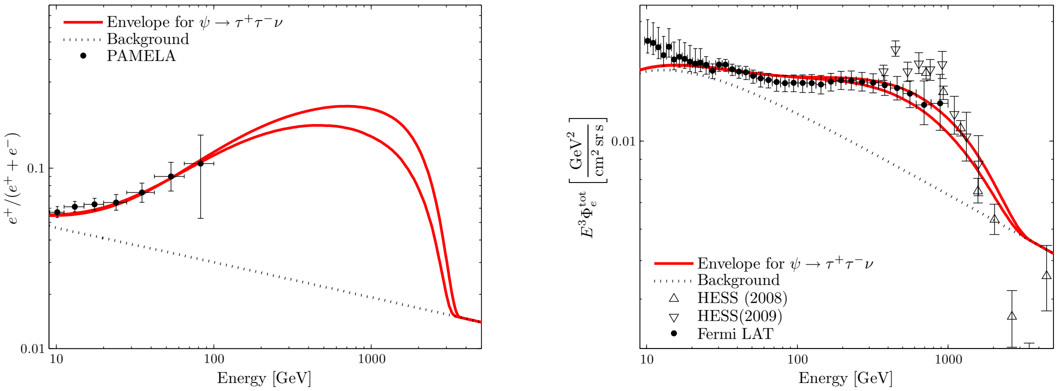

FIG. 4.1: The envelope of possible cosmic-ray spectra for $\psi \to \tau^+\tau^-\nu$. Ranges of the fit parameters are given in the text.

the H.E.S.S. bands of systematic uncertainty.)

Leaving m_ψ and τ_ψ as free variables, we find that our results are relatively insensitive to the choice of (ξ_+, ξ_-). This is demonstrated for the pure decay $\psi \to \tau^+\tau^-\nu$ in Fig. 4.1 where we show the envelope of possible cosmic-ray spectra; that is, when we sample the (ξ_+, ξ_-) parameter space, we find that all of the resulting curves fall between those plotted in Fig. 4.1. For the example shown, m_ψ varies between 6.5 and 8.5 TeV while τ_ψ varies between 0.5×10^{26} s and 0.7×10^{26} s; the χ^2 per degree of freedom (χ^2/d.o.f.) remains between 0.5 and 0.6. We performed the same analysis on the other decay scenarios discussed below and found a similar behavior. As such, we take $(\xi_+, \xi_-) = (48, 48)$ for the remaining results that we present.

As a starting point, we show the cosmic-ray spectra for some charged-lepton-flavor-conserving decays in Fig. 4.2. We consider the pure decays $\psi \to \mu^+\mu^-\nu$ and $\psi \to \tau^+\tau^-\nu$, and we also consider the flavor-democratic decay for which $B(\ell_i^+\ell_i^-\nu) = 1/3$ for all i. For $\psi \to \mu^+\mu^-\nu$, we have a χ^2/d.o.f. of approximately 0.9. For $\psi \to \tau^+\tau^-\nu$, we have $\chi^2/\text{d.o.f.} \approx 0.6$. And for the flavor-democratic $\psi \to \ell^+\ell^-\nu$, we have $\chi^2/\text{d.o.f.} \approx 0.8$. These are to be contrasted with the flavor-violating decays

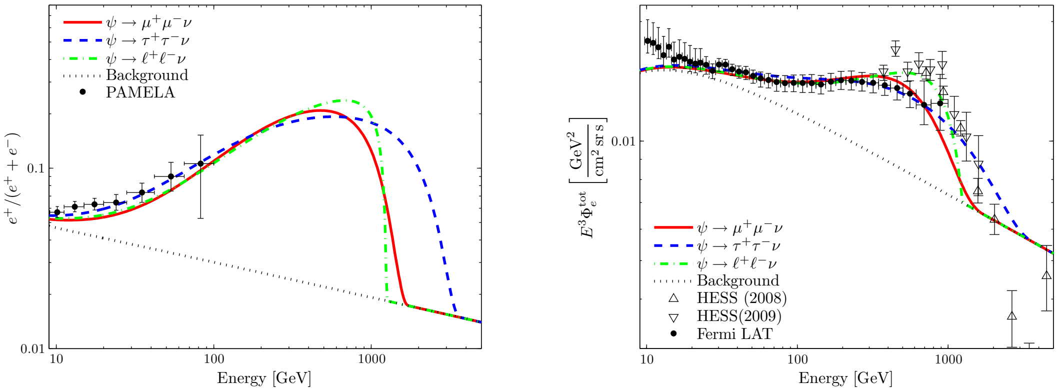

FIG. 4.2: Positron fraction and total electron-positron flux for some charged-lepton-flavor-conserving decays. Best fits are shown, corresponding to the following masses and lifetimes: for $\psi \to \mu^+\mu^-\nu$, $m_\psi = 3.5$ TeV and $\tau_\psi = 1.5 \times 10^{26}$ s; for $\psi \to \tau^+\tau^-\nu$, $m_\psi = 7.5$ TeV and $\tau_\psi = 0.6 \times 10^{26}$ s; for the flavor-democratic decay $\psi \to \ell^+\ell^-\nu$, $m_\psi = 2.5$ TeV and $\tau_\psi = 1.9 \times 10^{26}$ s.

of Fig. 4.3.

We consider three classes of flavor-violating decays:

$$\psi \to e^\pm\mu^\mp\nu, \qquad \psi \to e^\pm\tau^\mp\nu, \qquad \text{and} \qquad \psi \to \mu^\pm\tau^\mp\nu. \tag{4.21}$$

Each class contains two decay channels (e.g., $\psi \to e^+\mu^-\nu$ and $\psi \to e^-\mu^+\nu$). We consider all six of the pure decays, i.e., decays involving only one channel. We also consider mixtures of decay channels belonging to the same class; some representative choices are shown in Fig. 4.3. Note that, for fixed m_ψ and τ_ψ, the total electron-positron flux – which does not distinguish between the two electric charges – is the same for any two decays belonging to the same class. For this reason, we require only one plot of the total flux in Fig. 4.3. We find that the χ^2 is relatively flat as a function of the branching fraction within each class of decays: over the range of possible branching fractions, we find that the χ^2/d.o.f. varies by no more than ±10% from 1.2, 1.1 and 0.6, for $\psi \to e^\pm\mu^\mp\nu$, $\psi \to e^\pm\tau^\mp\nu$, and $\psi \to \mu^\pm\tau^\mp\nu$, respectively. Different choices for the branching fraction within a given class describe the existing data well,

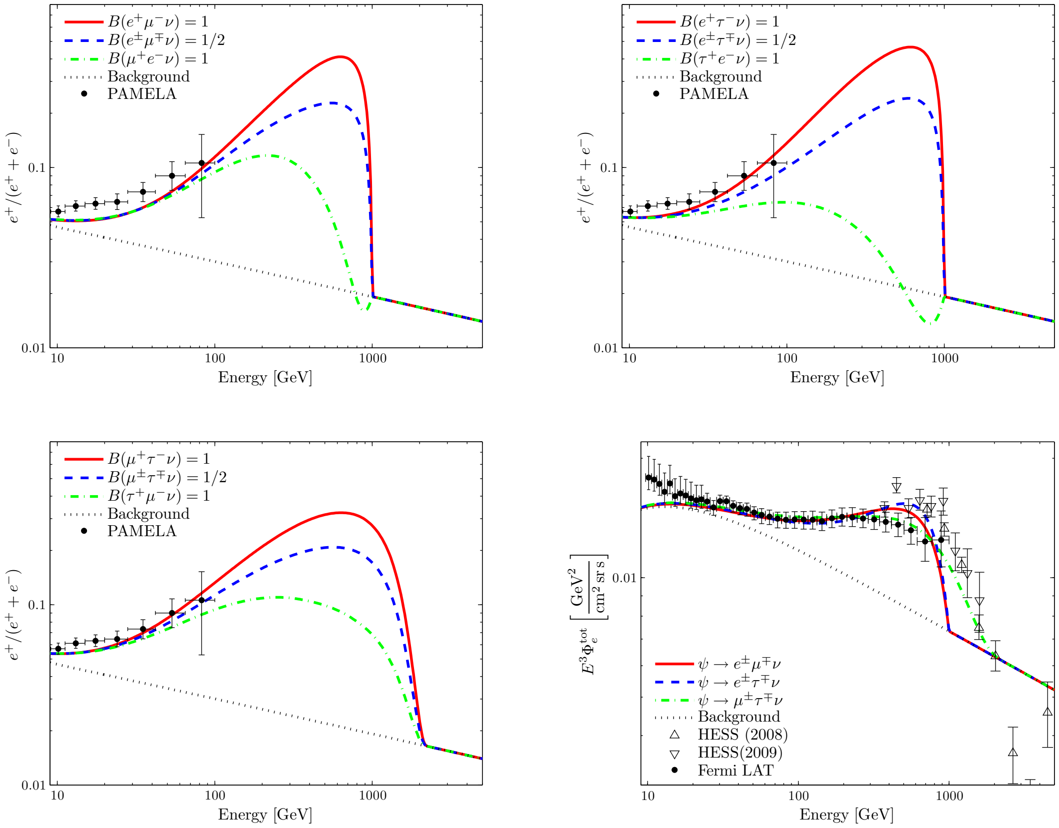

FIG. 4.3: Positron fraction and total electron-positron flux for some charged-lepton-flavor-violating decays with various sets of branching fractions. Best fits are shown, corresponding to the following masses and lifetimes: for $\psi \to e^\pm\mu^\mp\nu$, $m_\psi = 2.0$ TeV and $\tau_\psi = 2.9 \times 10^{26}$ s; for $\psi \to e^\pm\tau^\mp\nu$, $m_\psi = 2.0$ TeV and $\tau_\psi = 2.4 \times 10^{26}$ s; for $\psi \to \mu^\pm\tau^\mp\nu$, $m_\psi = 4.5$ TeV and $\tau_\psi = 1.0 \times 10^{26}$ s.

but provide different predicted spectra that interpolate between the curves shown. Note that the distinctive dip in the $\mu^+e^-\nu$ and $\tau^+e^-\nu$ positron fractions around 1 TeV is due to the hard electron produced in the initial decay; this greatly enhances the electron to positron ratio in the high energy bins, leading to a suppression in the positron fraction for fixed total flux.

4.4 Discussion

The results presented in the previous section show that a variety of possible lepton-flavor-violating decay modes for a spin-1/2, charge asymmetric dark matter candidate can describe existing data well, as quantified by the χ^2 per degree of freedom for the best fits to the data. Significantly, the results for the predicted positron fraction differ substantially for energies above ~ 100 GeV, the maximum for which the PAMELA experiment is sensitive. In some case, more precise measurement of the total electron-postron flux around 1 TeV may also provide a means of distinguishing these scenarios. Future data from experiments like AMS-02 [161], which can probe these energy ranges of the predicted spectra, may determine whether the possibilities discussed in this chapter present viable descriptions of the cosmic-ray spectrum.

In the meantime, the present work suggests a number of directions for further study: In the case where the stable, neutral particle in the final state is a standard model neutrino, one could study whether the decays of asymmetric dark matter that we have considered could be probed at neutrino observatories like IceCube [159, 160] . One could also study additional astrophysical bounds on the scenarios described, for example, from the extragalactic gamma ray flux [157]. One can also attempt to find preferred forms of the underlying four-fermion operators (whose effects were parametrized in the present analysis by $\xi_{\pm}$) by studying the simplest and best-motivated models that provide for their origin. Work in these directions is in progress and will be described in a longer publication.

CHAPTER 5

The Galactic Center Region Gamma Ray Excess from A Supersymmetric Leptophilic Higgs Model[8]

5.1 Introduction

Recently, Hooper and Goodenough examined the first two years of Fermi Gamma Ray Space Telescope (FGST) data from the inner 10° around the Galactic Center [170]. They found that the gamma ray emissions coming from between 1.25° and 10° of the Galactic Center is consistent with what is expected from known emission mechanisms such as cosmic rays colliding with gas to produce subsequently decaying pions, inverse Compton scattering of cosmic ray electrons, and known gamma ray point sources. In order to model the gamma ray background within 2° of the

---

[8] This chapter was previously published in JHEP 1105 (2011) 026.

Galactic Center, Hooper and Goodenough model the emission of the Galactic black hole Sgr A* as a power-law extrapolated from higher energy HESS observations. Comparing the FGST measurements to this background, Hooper and Goodenough found that it agrees very well with FGST data between $1.25° - 2°$ but found an excess in the observed gamma ray intensity within 1.25°. It has been pointed out by Ref. [171] however, that a simple power-law extrapolation of HESS data may understate the flux of the central point source Sgr A* as the slope of its spectrum may deviate from the constant HESS results below an energy of 100 GeV.

The authors of Ref. [170] showed that the increased gamma ray emissions are well described by annihilating dark matter that has a cusped halo profile ($\rho \propto r^{-\gamma}$, with $\gamma = 1.18$ to 1.33) provided that the dark matter satisfies three basic conditions. The conditions required of the dark matter are 1) that it have a mass between $7 - 10$ GeV, 2) that it annihilate into τ-pairs most of the time, but into hadronic channels $15 - 40\%$ of the time, and 3) that its total annihilation cross section yield a thermal average within the range $\langle \sigma v \rangle = 4.6 \times 10^{-27} - 5.3 \times 10^{-26}$ cm^3/s. It should be noted that the results of Hooper and Goodenough are controversial, and the Fermi-LAT collaboration itself has not yet published official results. In addition, other background related explanations for the gamma ray excess have been proposed such as the existence of a pulsar near the Galactic Center [172]. In this chapter we proceed with the assumption that the analysis of Hooper and Goodenough is correct. The astrophysical and particle physics implications of this finding are discussed in Refs. [173, 174].

In this chapter we construct a dark matter model satisfying the above conditions by adding a singlet to the supersymmetric leptophilic Higgs model (SLHM) [175]. In the SLHM the up quarks, down quarks, and leptons, each receive mass from a separate Higgs doublet. For our purposes, the salient characteristic of the SLHM is that it endows the leptons with an enhanced coupling to one of the scalars. This provides a natural mechanism for dark matter particles to annihilate predominantly into τ-pairs. This model of dark matter is able to successfully account for the FGST observations, yields the correct relic density, and evades relevant collider bounds such as measurements of the Z width and direct production at LEP. The idea of a leptophilic Higgs has been studied as a possible explanation for the $e^{\pm}$ excess observed by PAMELA and ATIC in Ref. [122]. However, this entails a 100 GeV - 1 TeV dark matter particle, while our model requires a light, $\mathcal{O}(10)$ GeV dark matter particle. There also exist some other models that can explain the Galactic Center gamma ray excess [176].

In addition to explaining the FGST observations, such a model of light dark matter is also capable of describing observations by the CoGeNT [21] and DAMA collaborations [22]. CoGeNT has recently reported direct detection signals that hint at the presence of $\mathcal{O}(10)$ GeV dark matter compatible with the light dark matter interpretation of DAMA's annual event rate modulation. Ref. [28] showed that dark matter with a mass between $7 - 8$ GeV that has a spin independent cross section approximately between $\sigma_{SI} = 1 \times 10^{-40} - 3 \times 10^{-40}$ cm^2 is consistent with both CoGeNT and DAMA signals. Although the XENON [177] and CDMS [178] collaborations challenge this report, Ref. [174] has pointed out that "zero-charge" background events lie in the signal region. The authors suggest that the bound could possibly be loosened if a modest uncertainty or systematic error is introduced in the energy scale calibration near the energy threshold. Although our model is able to explain the reported observations of the CoGeNT and DAMA collaborations, it is not dependent upon their validity. By simply moving to another region of parameter space our model can coexist with the absolute refutation of CoGeNT and DAMA while continuing to explain the FGST results and avoiding collider bounds.

This chapter is organized as follows. In Section 5.2 we introduce the setup of the model and calculate the mass matrices for the scalars and the neutralinos.

In Section 5.3 we describe the process by which the dark matter annihilates into Standard model particles and calculate the relevant cross sections for a benchmark point in parameter space. We also show that the resultant relic density is consistent with current cosmological measurements. In Section 5.4 we discuss possible direct detection and in Section 5.5 we discuss relevant bounds for this model and show that it is currently viable. Lastly, we conclude with Section 5.6 and summarize the results of the chapter.

5.2 The Model

In this model the quark and lepton content is that of the MSSM. To this we add four Higgs doublets, $\widehat{H}_u$, $\widehat{H}_d$, $\widehat{H}_0$, and $\widehat{H}_\ell$, with weak hypercharge assignment $+1/2$, $-1/2$, $+1/2$, and $-1/2$ respectively. The third Higgs doublet is necessary to achieve a leptonic structure, while the fourth doublet is required for anomaly cancelation. In order to avoid problems with the Z decay width, we introduce a singlet $\widehat{S}$ that acts as $\mathcal{O}(10)$ GeV dark matter. The idea of adding a light singlet to the MSSM to act as dark matter was also considered in [179], while the use of a singlet for other purposes such as solving the μ problem was first developed in [180–182]. The superpotential is given by

$$\begin{aligned} W = {} & y_u \widehat{U}\widehat{Q}\widehat{H}_u - y_d \widehat{D}\widehat{Q}\widehat{H}_d - y_\ell \widehat{E}\widehat{L}\widehat{H}_\ell + \mu_q \widehat{H}_u \widehat{H}_d + \mu_\ell \widehat{H}_0 \widehat{H}_\ell \\ & + \kappa_q \widehat{S}\widehat{H}_u\widehat{H}_d + \kappa_\ell \widehat{S}\widehat{H}_0\widehat{H}_\ell + \lambda_1^2 \widehat{S} + \frac{1}{2}\,\lambda_2 \widehat{S}^2 + \frac{1}{3}\,\kappa_s \widehat{S}^3, \end{aligned} \tag{5.1}$$

where the hats denote superfields. In the superpotential we introduced a $\mathbb{Z}_2$ symmetry under which $\widehat{H}_0$, $\widehat{H}_\ell$ and $\widehat{E}$ are odd while all other fields are even. The symmetry enforces a Yukawa structure in which $\widehat{H}_u$ gives mass to up-type quarks, $\widehat{H}_d$ to down-type quarks, and $\widehat{H}_\ell$ to leptons, while $\widehat{H}_0$ does not couple to the quarks or leptons and is called the inert doublet. It is introduced to ensure anomaly cancellation. The $\mathbb{Z}_2$ symmetry is broken in V_{soft} so that we have: [9]

$$\begin{aligned}
V_{\text{soft}} = {} & m_u^2|H_u|^2 + m_d^2|H_d|^2 + m_0^2|H_0|^2 + m_\ell^2|H_\ell|^2 + m_s^2|S|^2 \\
& + \Big(\mu_1^2 H_u H_d + \mu_2^2 H_0 H_\ell + \mu_3^2 H_u H_\ell + \mu_4^2 H_0 H_d \\
& + \mu_a S H_u H_d + \mu_b S H_0 H_\ell + \mu_c S H_u H_\ell + \mu_d S H_0 H_d \\
& + m_{u0}^2 H_u^\dagger H_0 + m_{d\ell}^2 H_d^\dagger H_\ell + t^3 S + b_s^2 S^2 + a_s S^3 + \text{h.c.}\Big).
\end{aligned} \tag{5.2}$$

The breaking of the $\mathbb{Z}_2$ symmetry is discussed in greater detail in Appendix C. The Higgs sector potential is given by $V = V_D + V_F + V_{\text{soft}}$. Letting σ^a denote the Pauli matrices for $a = 1, 2, 3$, the D-term is simply

$$\begin{aligned}
V_D = {} & \frac{g^2}{8}\sum_a \Big| H_u^\dagger \sigma^a H_u + H_d^\dagger \sigma^a H_d + H_0^\dagger \sigma^a H_0 + H_\ell^\dagger \sigma^a H_\ell \Big|^2 \\
& + \frac{g'^2}{8}\Big| |H_u|^2 - |H_d|^2 + |H_0|^2 - |H_\ell|^2 \Big|^2,
\end{aligned} \tag{5.3}$$

where g and g' are the $SU(2)$ and $U(1)$ gauge couplings respectively. The F-term

---

[9] In Ref. [175] the soft breaking terms $m_{u0}^2 H_u^\dagger H_0 + m_{d\ell}^2 H_d^\dagger H_\ell + \text{h.c.}$ were omitted.

and V_{soft} combine with the D-term to yield the following potential

$$\begin{aligned}
V = {} & \big(\mu_q^2 + m_u^2\big)|H_u|^2 + \big(\mu_q^2 + m_d^2\big)|H_d|^2 + \big(\mu_\ell^2 + m_0^2\big)|H_0|^2 + \big(\mu_\ell^2 + m_\ell^2\big)|H_\ell|^2 \\
& + \Big[\big(\mu_1^2 + \kappa_q\lambda_1^2\big)H_uH_d + \big(\mu_2^2 + \kappa_\ell\lambda_1^2\big)H_0H_\ell + \mu_3^2H_uH_\ell + \mu_4^2H_0H_d + \text{h.c.}\Big] \\
& + \Big|\kappa_qH_uH_d + \kappa_\ell H_0H_\ell\Big|^2 + \Big(m_{u0}^2H_u^\dagger H_0 + m_{d\ell}^2H_d^\dagger H_\ell + \text{h.c.}\Big) + \big(m_s^2 + \lambda_2^2\big)|S|^2 \\
& + \Big[\big(t^3 + \lambda_1^2\lambda_2\big)S + \big(b_s^2 + \kappa_s\lambda_2^2\big)S^2 + a_sS^3 + \text{h.c.}\Big] + \kappa_s\lambda_2|S|^2\big(S + S^*\big) + \kappa_s^2|S|^4 \\
& + \Big[\mu_a\big(H_uH_d\big)S + \mu_b\big(H_0H_\ell\big)S + \mu_c\big(H_uH_\ell\big)S + \mu_d\big(H_0H_d\big)S + \text{h.c.}\Big] \\
& + \Big\{\lambda_2\Big[\kappa_q\big(H_uH_d\big) + \kappa_\ell\big(H_0H_\ell\big)\Big]S^* + \kappa_s\Big[\kappa_q\big(H_uH_d\big) + \kappa_\ell\big(H_0H_\ell\big)\Big](S^2)^* + \text{h.c.}\Big\} \\
& + \Big\{\kappa_q\mu_q\Big(|H_u|^2 + |H_d|^2\Big) + \kappa_\ell\mu_\ell\Big(|H_0|^2 + |H_\ell|^2\Big)\Big\}\big(S + S^*\big) \\
& + \kappa_q^2\Big(|H_u|^2 + |H_d|^2\Big)|S|^2 + \kappa_\ell^2\Big(|H_0|^2 + |H_\ell|^2\Big)|S|^2 + V_D.
\end{aligned} \tag{5.4}$$

The singlet S acquires the vev $\langle S\rangle = v_s/\sqrt{2}$ while the Higgs doublets acquire the vevs:

$$\langle H_u\rangle = \frac{1}{\sqrt{2}}\begin{pmatrix} 0 \\ v_u \end{pmatrix}, \quad \langle H_d\rangle = \frac{1}{\sqrt{2}}\begin{pmatrix} v_d \\ 0 \end{pmatrix}, \langle H_0\rangle = \frac{1}{\sqrt{2}}\begin{pmatrix} 0 \\ v_0 \end{pmatrix}, \quad \langle H_\ell\rangle = \frac{1}{\sqrt{2}}\begin{pmatrix} v_\ell \\ 0 \end{pmatrix}. \tag{5.5}$$

Letting $v_{\text{ew}}^2 = v_u^2 + v_d^2 + v_0^2 + v_\ell^2$ so that $v_{\text{ew}}^2 = 4M_Z^2/(g^2 + g'^2) \approx (246\text{ GeV})^2$, we define the mixing angles α, β, and β_ℓ by the relations $\tan\beta = v_u/v_d$, $\tan\beta_\ell = v_0/v_\ell$, and $\tan^2\alpha = (v_u^2 + v_d^2)/(v_0^2 + v_\ell^2)$. These definitions lead to the following parameterization of the Higgs vevs:

$$\begin{aligned}
v_u &= v_{\text{ew}}\sin\alpha\sin\beta, \quad & v_d &= v_{\text{ew}}\sin\alpha\cos\beta, \\
v_0 &= v_{\text{ew}}\cos\alpha\sin\beta_\ell, \quad & v_\ell &= v_{\text{ew}}\cos\alpha\cos\beta_\ell.
\end{aligned} \tag{5.6}$$

In order to avoid increasing the Z width or violating other known bounds, we want the light dark matter to separate from the other neutralinos and be mostly singlino $\tilde{s}$, the fermionic component of the singlet $\widehat{S}$. This is accomplished by taking the parameters κ_q and κ_ℓ to be small, which eliminates most of the mixing between the singlino and the Higgsinos [see Eq. (5.10)]. It can then be easily arranged to have the singlino be the lightest of the neutralinos. A possible mechanism for explaining the small size of κ_q and κ_ℓ is discussed in Appendix C. Small values of κ_q and κ_ℓ also leads to reduced mixing between the scalar singlet and the Higgs doublets as can be seen from Eq. (5.4). A small amount of mixing is of course required since we desire the lightest scalar, which is mostly singlet, to couple to τ-pairs in order for the dark matter to annihilate to $\tau^+\tau^-$ and other Standard Model particles. This mixing is generated by the soft supersymmetry-breaking parameters μ_a, μ_b, μ_c, and μ_d.

It is sufficient for κ_q and κ_ℓ to be $\mathcal{O}(10^{-2})$, which is what we use in our numerical calculations (see Table 5.1 and 5.2). Though the scalar mass matrices are quite complicated in general, they simplify considerably in the limit of vanishing κ_q and κ_ℓ. The numerical calculations in the sections that follow have been determined using the general matrices, but for compactness we present only the simplified matrices here. In the $\{h_u, h_d, h_0, h_\ell, h_s\}$ basis, the neutral scalar mass matrix is given by

$$M_N^2 = \begin{pmatrix} M^2 & \overrightarrow{m}^2 \\ \overrightarrow{m}^{2\,T} & M_{SS}^2 \end{pmatrix}, \tag{5.7}$$

where the matrix M^2 is given by $M^2 = M^2_{\text{SLHM}} + \Delta M_1^2 + \Delta M_2^2$ and the terms $\overrightarrow{m}^2$ and M_{SS} are given by

$$\overrightarrow{m}^{2\,T} = -\frac{1}{\sqrt{2}}\left(\mu_a v_d + \mu_c v_\ell,\ \mu_a v_u + \mu_d v_0,\ \mu_b v_\ell + \mu_d v_d,\ \mu_b v_0 + \mu_c v_u\right)$$

and

$$M_{SS}^2 = \frac{3\big(a_s + \kappa_s\lambda_2\big)v_s^2 + 2\sqrt{2}\kappa_s^2 v_s^3 - 2t^3 - 2\lambda_1^2\lambda_2 + \big(\mu_a v_u v_d + \mu_b v_0 v_\ell + \mu_c v_u v_\ell + \mu_d v_0 v_d\big)}{\sqrt{2}\, v_s}.$$

The matrix M^2_{SLHM} is the neutral scalar mass matrix from the ordinary SLHM, which can be found in [175], while the matrices ΔM_1^2 and ΔM_2^2 are given by

$$\Delta M_1^2 = \begin{pmatrix} -m_{u0}^2 \frac{v_0}{v_u} & 0 & m_{u0}^2 & 0 \\ 0 & -m_{d\ell}^2 \frac{v_\ell}{v_d} & 0 & m_{d\ell}^2 \\ m_{u0}^2 & 0 & -m_{u0}^2 \frac{v_u}{v_0} & 0 \\ 0 & m_{d\ell}^2 & 0 & -m_{d\ell}^2 \frac{v_d}{v_\ell} \end{pmatrix},$$

and

$$\Delta M_2^2 = \frac{1}{\sqrt{2}} \begin{pmatrix} \frac{v_s}{v_u}\left(\mu_a v_d + \mu_c v_\ell\right) & -v_s\mu_a & 0 & -v_s\mu_c \\ -v_s\mu_a & \frac{v_s}{v_d}\left(\mu_a v_u + \mu_d v_0\right) & -v_s\mu_d & 0 \\ 0 & -v_s\mu_d & \frac{v_s}{v_0}\left(\mu_b v_\ell + \mu_d v_d\right) & -v_s\mu_b \\ -v_s\mu_c & 0 & -v_s\mu_b & \frac{v_s}{v_\ell}\left(\mu_b v_0 + \mu_c v_u\right) \end{pmatrix}.$$

The pseudoscalar mass matrix, in the $\{a_u, a_d, a_0, a_\ell, a_s\}$ basis, is similarly given by

$$M_A^2 = \begin{pmatrix} \widetilde{M}^2 & -\overrightarrow{m}^2 \\ -\overrightarrow{m}^{2\,T} & \widetilde{M}_{SS}^2 \end{pmatrix}, \tag{5.8}$$

where $\widetilde{M}^2 = \widetilde{M}^2_{\mathrm{SLHM}} + \Delta M_1^2 + \Delta\widetilde{M}_2^2$. The matrix $\widetilde{M}^2_{\mathrm{SLHM}}$ is the pseudoscalar mass matrix from the ordinary SLHM while $\Delta\widetilde{M}_2^2$ is the matrix obtained from ΔM_2^2 by changing the sign of every off-diagonal entry. Lastly, $\widetilde{M}^2_{SS}$ is given by

$$\begin{aligned}\widetilde{M}^2_{SS} = \frac{1}{\sqrt{2}\,v_s}\Big[&\mu_a v_u v_d + \mu_b v_0 v_\ell + \mu_c v_u v_\ell + \mu_d v_0 v_d - 2\lambda_1^2\lambda_2 \\ &- 2t^3 - \big(9a_s + \kappa_s\lambda_2\big)v_s^2 - 4\sqrt{2}\,(b_s^2 + \kappa_s\lambda_2^2)v_s\Big].\end{aligned}$$

The chargino mass matrix, on the other hand, is rather simple even with nonvanishing κ_q and κ_ℓ. Letting $\tilde{h}_u$, $\tilde{h}_d$, $\tilde{h}_0$, and $\tilde{h}_\ell$ denote the Higgsino gauge eigenstates, the chargino mass matrix, in the $\{\widetilde{W}^+, \tilde{h}_u^+, \tilde{h}_0^+, \widetilde{W}^-, \tilde{h}_d^-, \tilde{h}_\ell^-\}$ basis, is given by

$$M_{\chi^\pm} = \begin{pmatrix} 0 & 0 & 0 & M_2 & gv_d & gv_\ell \\ 0 & 0 & 0 & gv_u & \mu_q + \frac{\kappa_q}{\sqrt{2}}v_s & 0 \\ 0 & 0 & 0 & gv_0 & 0 & \mu_\ell + \frac{\kappa_\ell}{\sqrt{2}}v_s \\ M_2 & gv_u & gv_0 & 0 & 0 & 0 \\ gv_d & \mu_q + \frac{\kappa_q}{\sqrt{2}}v_s & 0 & 0 & 0 & 0 \\ gv_\ell & 0 & \mu_\ell + \frac{\kappa_\ell}{\sqrt{2}}v_s & 0 & 0 & 0 \end{pmatrix}. \tag{5.9}$$

Like the chargino mass matrix, the neutralino mass matrix is simple. The neutralino mass matrix, in the $\{\widetilde{B}^0, \widetilde{W}^0, \tilde{h}_u, \tilde{h}_d, \tilde{h}_0, \tilde{h}_\ell, \tilde{s}\}$ basis, is given by

$$M_\chi = \begin{pmatrix} M_1 & 0 & \frac{1}{2}g'v_u & -\frac{1}{2}g'v_d & \frac{1}{2}g'v_0 & -\frac{1}{2}g'v_\ell & 0 \\ 0 & M_2 & -\frac{1}{2}gv_u & \frac{1}{2}gv_d & -\frac{1}{2}gv_0 & \frac{1}{2}gv_\ell & 0 \\ \frac{1}{2}g'v_u & -\frac{1}{2}gv_u & 0 & \mu_q + \frac{\kappa_q}{\sqrt{2}}v_s & 0 & 0 & \frac{\kappa_q}{\sqrt{2}}v_d \\ -\frac{1}{2}g'v_d & \frac{1}{2}gv_d & \mu_q + \frac{\kappa_q}{\sqrt{2}}v_s & 0 & 0 & 0 & \frac{\kappa_q}{\sqrt{2}}v_u \\ \frac{1}{2}g'v_0 & -\frac{1}{2}gv_0 & 0 & 0 & 0 & \mu_\ell + \frac{\kappa_\ell}{\sqrt{2}}v_s & \frac{\kappa_\ell}{\sqrt{2}}v_\ell \\ -\frac{1}{2}g'v_\ell & \frac{1}{2}gv_\ell & 0 & 0 & \mu_\ell + \frac{\kappa_\ell}{\sqrt{2}}v_s & 0 & \frac{\kappa_\ell}{\sqrt{2}}v_0 \\ 0 & 0 & \frac{\kappa_q}{\sqrt{2}}v_d & \frac{\kappa_q}{\sqrt{2}}v_u & \frac{\kappa_\ell}{\sqrt{2}}v_\ell & \frac{\kappa_\ell}{\sqrt{2}}v_0 & \lambda_2 + \sqrt{2}\kappa_s v_s \end{pmatrix}. \tag{5.10}$$

When κ_q and κ_ℓ are small, the singlino part of the above matrix separates from the

TABLE 5.1: Benchmark Point A

κ_q	=	0.01	v_ℓ	=	1.2 GeV	μ_2^2	=	(200 GeV)^2
κ_ℓ	=	0.01	μ_q	=	125 GeV	μ_3^2	=	(200 GeV)^2
κ_s	=	0.6	μ_ℓ	=	125 GeV	μ_4^2	=	(400 GeV)^2
$\tan\alpha$	=	20	λ_1^2	=	(100 GeV)^2	μ_a	=	100 GeV
$\tan\beta$	=	50	λ_2	=	-35 GeV	μ_b	=	200 GeV
$\tan\beta_l$	=	10	M_1	=	500 GeV	μ_c	=	200 GeV
v_s	=	50 GeV	M_2	=	500 GeV	μ_d	=	200 GeV
v_u	=	245.6 GeV	m_{u0}^2	=	$-$(100 GeV)^2	t^3	=	(60.6 GeV)^3
v_d	=	4.9 GeV	$m_{d\ell}^2$	=	(100 GeV)^2	b_s^2	=	(63.4 GeV)^2
v_0	=	12.2 GeV	μ_1^2	=	(400 GeV)^2	a_s	=	-42.4 GeV

wino, bino, and higgsinos, and the singlino mass can be well approximated by

$$m_{\chi_1} \approx \lambda_2 + \sqrt{2}\kappa_s v_s. \tag{5.11}$$

The $\mathcal{O}(10)$ GeV LSP can be arranged with some tuning of the parameters in order to achieve a cancelation between λ_2 and the product $\kappa_s v_s$ in Eq. (5.11). Though the smallness of κ_q and κ_ℓ is technically unnatural, we remind the reader that a possible mechanism to make them small is discussed in Appendix C.

In the following sections, we calculate the relevant cross sections and quantities of interest using benchmark points A and B, found in Tables 5.1 and 5.2 respectively. While both of these benchmark points can explain the Galactic Central region gamma ray excess, the spin independent direct detection cross section corresponding to benchmark point A lies within the region favored by CoGeNT and DAMA. In contrast, we will show that benchmark point B satisfies CDMS bounds that exclude CoGeNT and DAMA. Relevant quantities have been calculated for several additional benchmark points as well, and their values are summarized in Table D.1 of Appendix D.

TABLE 5.2: Benchmark Point B

κ_q	$=$	0.01	v_ℓ	$=$	1.2 GeV	μ_2^2	$=$	$(200\ \text{GeV})^2$
κ_ℓ	$=$	0.01	μ_q	$=$	125 GeV	μ_3^2	$=$	$(200\ \text{GeV})^2$
κ_s	$=$	0.6	μ_ℓ	$=$	125 GeV	μ_4^2	$=$	$(400\ \text{GeV})^2$
$\tan\alpha$	$=$	20	λ_1^2	$=$	$(100\ \text{GeV})^2$	μ_a	$=$	100 GeV
$\tan\beta$	$=$	50	λ_2	$=$	-35 GeV	μ_b	$=$	200 GeV
$\tan\beta_l$	$=$	10	M_1	$=$	500 GeV	μ_c	$=$	200 GeV
v_s	$=$	50 GeV	M_2	$=$	500 GeV	μ_d	$=$	200 GeV
v_u	$=$	245.6 GeV	m_{u0}^2	$=$	$-(100\ \text{GeV})^2$	t^3	$=$	$(55.0\ \text{GeV})^3$
v_d	$=$	4.9 GeV	$m_{d\ell}^2$	$=$	$(100\ \text{GeV})^2$	b_s^2	$=$	$(66.3\ \text{GeV})^2$
v_0	$=$	12.2 GeV	μ_1^2	$=$	$(400\ \text{GeV})^2$	a_s	$=$	-42.2 GeV

5.3 Annihilation to Fermions

In this section, we will show that this model can achieve the conditions needed to explain the gamma ray excess in the Galactic Center region. In order to calculate the dark matter cross section, we need the interactions between Higgs and fermions:

$$
\begin{aligned}
\mathcal{L} \supset &-\frac{\kappa_s}{\sqrt{2}}\left[h_s\bar{\tilde{s}}\tilde{s} - i a_s\bar{\tilde{s}}\gamma^5\tilde{s}\right] \\
&-\frac{\kappa_q}{2\sqrt{2}}\left[h_u\bar{\tilde{s}}\tilde{h}_d - i a_u\bar{\tilde{s}}\gamma^5\tilde{h}_d + h_d\bar{\tilde{s}}\tilde{h}_u - i a_d\bar{\tilde{s}}\gamma^5\tilde{h}_u + h.c.\right] \\
&-\frac{\kappa_\ell}{2\sqrt{2}}\left[h_0\bar{\tilde{s}}\tilde{h}_\ell - i a_0\bar{\tilde{s}}\gamma^5\tilde{h}_\ell + h_\ell\bar{\tilde{s}}\tilde{h}_0 - i a_\ell\bar{\tilde{s}}\gamma^5\tilde{h}_0 + h.c.\right] \\
&-\sum_{f=\{u,d,\ell\}}\sum_j \frac{m_{f_j}}{v_f}\left(h_f\bar{f}_j f_j - i a_f\bar{f}_j\gamma^5 f_j\right),
\end{aligned}
\tag{5.12}
$$

where m_{f_j} is the mass of the fermion f_j, v_f is the vev of f-type scalars, and j runs over the fermion generations. In the limit $\kappa_q, \kappa_\ell \to 0$, the higgs-higgsino-singlino interactions vanish.

We can expand $\langle\sigma v\rangle$ in powers of the dark matter velocity squared v^2:

$$
\langle\sigma v\rangle = a + bv^2 + \ldots . \tag{5.13}
$$

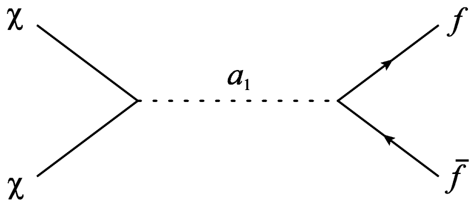

FIG. 5.1: The dominant diagram of dark matter annihilation into fermions. Here a_1 is the lightest pseudoscalar.

Only the s-wave contribution to a is relevant in discussing the gamma ray excess coming from dark matter annihilation since the velocity of the dark matter in the Galactic Center region is relatively low. An exception to this is within the sphere of influence of the Milky Way supermassive black hole, but this region corresponds to only a fraction of an arc second and is below FGST accuracy. As we see later, a_1 is mostly singlet for benchmark points A and B. Therefore the s-wave contribution to dark matter annihilation to fermions comes mostly from the s-channel diagram involving an exchange of the lightest pseudoscalar a_1 given in Fig. 5.1. It is approximately given by

$$a \approx \frac{N_c \kappa_s^2 \, U_{1f}^2}{4\pi} \frac{m_f^2}{v_f^2} \frac{m_{\chi_1}^2}{(4m_{\chi_1}^2 - m_{a_1}^2)^2} \sqrt{1 - \frac{m_f^2}{m_{\chi_1}^2}}, \tag{5.14}$$

where N_c is the number of fermion colors, U_{1f} is the $(1, f)$ element of the pseudoscalar diagonalizing matrix and m_{a_1} is the mass of the lightest pseudoscalar. The s-wave contributions from heavier pseudoscalars are suppressed by larger masses as well as smaller mixings with the singlet. Moreover, s-channel scalar exchange diagrams are s-wave suppressed, i.e. $a\,(\chi_1\chi_1 \to h_i \to \bar{f}f) = 0$.

For benchmark point A, the dark matter mass is $m_{\chi_1} = 7.4$ GeV. The physical dark matter can be expressed in terms of gauge eigenstates as:

$$\chi_1 = 0.0017\,\widetilde{B}^0 - 0.0031\,\widetilde{W}^0 - 0.0141\,\tilde{h}_u - 0.0046\,\tilde{h}_d - 0.0001\,\tilde{h}_0 - 0.0008\,\tilde{h}_\ell + 0.9999\,\tilde{s}.$$

We need a light pseudoscalar, $\mathcal{O}(10)$ GeV, to get a sizeable annihilation cross section. This requires 1% tuning in the parameter space in addition to the tuning needed to make the singlino the LSP. The lightest pseudoscalar in the benchmark point is mostly singlet with a mixing with other types of pseudoscalar given by

$$a_1 = -0.000002\, a_u - 0.002193\, a_d - 0.001203\, a_0 - 0.003679\, a_\ell + 0.999990\, a_s,$$

with its mass is $m_{a_1} = 18.7$ GeV.

Having the masses and mixing, we can calculate the total annihilation cross section into fermion pairs which gives

$$\langle \sigma v \rangle \ = \ 4.0 \times 10^{-26}\ \mathrm{cm}^3/\mathrm{s} \tag{5.15}$$

where the hadronic final states cross section is 23% of the total cross section and τ pairs final state makes up the rest. For benchmark point B given in Table 5.2, the mass of dark matter is $m_{\chi_1} = 7.4$ GeV and $\langle \sigma v \rangle = 3.0 \times 10^{-26}$ cm^3/s, with the hadronic final states make up 23% of it. The annihillation cross sections given above are within the range of suggested cross section for explaining the gamma ray excess in the Galactic Center region given in Ref. [170].

In this model, dark matter annihilation into SM fermions given in Fig. 5.1 is also responsible for giving the dark matter the correct thermal relic abundance. To show this, we calculate the relic abundance which is given by [32]

$$\Omega_{\chi_1} h^2 \approx 2.82 \times 10^8\, Y_\infty (m_{\chi_1}/\mathrm{GeV}), \tag{5.16}$$

where

$$Y_\infty^{-1} = 0.264\, \sqrt{g_*} m_P m_{\chi_1} \left\{ a/x_f + 3(b - \tfrac{1}{4}a)/x_f^2 \right\}. \tag{5.17}$$

In the equation above, m_P is the Planck mass and g_* is the number of relativistic degrees of freedom at freeze-out. The freeze-out epoch x_f is related to the freeze-out temperature T_f by $x_f = m_{\chi_1}/T_f$, and x_f is determined by [32]

$$x_f = \ln\left[0.0764\, m_P(a + 6b/x_f)c(2+c)m_{\chi_1}/\sqrt{g_* x_f}\right]. \tag{5.18}$$

The value of c is usually taken as $c = \frac{1}{2}$. Approximating g_* to be a ladder function, we get that, for both of our benchmark points, the freeze-out epoch is $x_f = 21$ and the relic abundance is

$$\Omega_{\chi_1} h^2 \approx 0.1, \tag{5.19}$$

which agrees with the cosmologically measured abundance [183]. Since the freeze-out temperature happens to be around the QCD phase transition temperature, g_* varies significantly over the change of temperature [97] and the result (5.19) can change up to $\mathcal{O}(1)$. However the relic density is in the correct ballpark, therefore we do not expect that the correction will invalidate our result. An adjustment of parameters can be done when taking into account of the variation of g_* to get the correct density and annihilation cross section.

The benchmark points A and B serve as examples to show that in principle this model can explain the gamma ray excess in the Galactic Center region. However, the excess could also be obtained by some other regions in the parameter space as shown in the Appendix D. One could do a scan on the parameter space to find the favored region of the model.

Note that in our relic density calculation, we have neglected possible chargino and sfermion contributions coming from resonance and coannihilation effects. This is because the charginos have masses $\mathcal{O}(100)$ GeV for all of our benchmark points, and we assume that the sfermion masses are at least $\mathcal{O}(100)$ GeV, which is consistent with current LEP bounds.

5.4 Direct Detection

Having shown that this model can account for the gamma ray excess in the Galactic Center region, we now discuss direct detection of dark matter of this model. In this section, we will consider constraints from the search for spin independent, elastic scattering of dark matter off target nuclei. The most relevant contribution for the cross section is given by the t-channel scalar exchange diagram with the effective Lagrangian:

$$\mathcal{L}_{int} = \sum_q \alpha_q \bar{\chi}_1 \chi_1 \bar{q} q. \tag{5.20}$$

In our benchmark points, the only relevant contribution to dark matter detection comes from the lightest scalar and α_q can be approximated by

$$\alpha_q \approx \frac{\kappa_s m_q V_{1q}}{\sqrt{2} v_q m_{h_1}^2}, \tag{5.21}$$

where m_q is the mass of quark q, v_q is the scalar vev associated with quark flavor q, V_{1q} is the $(1, q)$ element of the scalar diagonalizing matrix, and m_{h_1} is the mass of the lightest scalar. Given the partonic interaction between dark matter and quarks, we can follow Ref. [99] to get the effective interaction with nucleons:

$$\mathcal{L}_{eff} = f_p \, \bar{\chi}_1 \chi_1 \, \bar{p} p + f_n \, \bar{\chi}_1 \chi_1 \, \bar{n} n, \tag{5.22}$$

where f_p and f_n are related to α_q through the relation [99]

$$\frac{f_{p,n}}{m_{p,n}} = \sum_{q=u,d,s} \frac{f_{Tq}^{(p,n)} \alpha_q}{m_q} + \frac{2}{27} f_{Tg}^{(p,n)} \sum_{q=c,b,t} \frac{\alpha_q}{m_q}, \tag{5.23}$$

and $\langle n|m_q\bar{q}q|n\rangle = m_n f^n_{Tq}$. Numerically, the $f^{(p,n)}_{Tq}$ are given by [100]

$$\begin{aligned} f^p_{Tu} &= 0.020 \pm 0.004,\ f^p_{Td} = 0.026 \pm 0.005,\ f^p_{Ts} = 0.118 \pm 0.062 \\ f^n_{Tu} &= 0.014 \pm 0.0043,\ f^n_{Td} = 0.036 \pm 0.008,\ f^n_{Ts} = 0.118 \pm 0.062, \end{aligned} \tag{5.24}$$

while $f^{(p,n)}_{Tg}$ is defined by

$$f^{(p,n)}_{Tg} = 1 - \sum_{q=u,d,s} f^{(p,n)}_{Tq}\ . \tag{5.25}$$

We can approximate $f_p \approx f_n$ since f_{Ts} is larger than other f_{Tq}'s and f_{Tg}. For the purpose of comparing the predicted cross section with existing bounds, we evaluate the cross section for scattering off a single nucleon. The result can be approximated as

$$\sigma_{SI} \approx \frac{4m_r^2 f_p^2}{\pi} \tag{5.26}$$

where m_r is nucleon-dark matter reduced mass $1/m_r = 1/m_n + 1/m_{\chi_1}$.

We are now ready to show that benchmark point A can explain signals reported by CoGeNT [21] and DAMA [22]. For this benchmark point, the lightest scalar mass is $m_{h_1} = 11.3$ GeV. This lightest scalar is mostly singlet and its mixing with other scalars is given by

$$h_1 = 0.089\, h_u + 0.004\, h_d + 0.010\, h_0 + 0.004\, h_\ell + 0.996\, h_s.$$

As in the case of pseudoscalar, contributions from higher mass scalars are suppressed by their masses and their mixings with the singlet. The spin independent cross section for the benchmark point now can be calculated and is given by

$$\sigma_{SI} = 1.7 \times 10^{-40}\ \text{cm}^2, \tag{5.27}$$

which is inside the CoGeNT and DAMA favored region [28].

Similarly, we can show that benchmark point B given in Table 5.2 has the lightest scalar mass $m_{h_1} = 41.5$ GeV and spin independent cross section $\sigma_{SI} = 1.2 \times 10^{-42}$ cm^2. This cross section is two orders of magnitude lower than the present CDMS and XENON bound [177, 178].

5.5 Bounds on the Model

In this section we discuss various collider bounds that apply to the model. We will spend most of the discussions in this section for the benchmark point A given in Table 5.1. The bounds for benchmark point B as well as the summary of the bounds for benchmark point A are given in Table 5.3.

In this model, the decays $Z \to \chi_1\chi_1$ and $Z \to h_1a_1$ are allowed kinematically. The Z decay width has been measured precisely and is given by $\Gamma = 2.4952 \pm 0.0023$ GeV [5]. Corrections to the decay width can be used as a bound on the mixing between the singlet and the Higgs sector. The partial decay width of $Z \to \chi_1\chi_1$ is given by

$$\Gamma_{Z\to\chi_1\chi_1} = \frac{G_F\theta_\chi^2}{48\sqrt{2}\pi} m_Z^3 \left(1 - \frac{4m_{\chi_1}^2}{m_Z^2}\right)^{\frac{3}{2}}, \tag{5.28}$$

where G_F is the Fermi constant, m_Z is Z mass, and θ_χ is given by

$$\theta_\chi = |W_{u1}|^2 - |W_{d1}|^2 + |W_{01}|^2 - |W_{\ell 1}|^2 . \tag{5.29}$$

In the equation above, W_{f1} is the $(f, 1)$ element of the neutralino diagonalizing matrix. The decay width of $Z \to h_1a_1$ is given by

$$\Gamma_{Z\to h_1a_1} = \frac{G_F|\theta_{ha}|^2}{3\sqrt{2}\pi} p^3, \tag{5.30}$$

TABLE 5.3: Mass spectrum and bounds for benchmark points A and B. The variable k is given by $k = \sigma_{hZ}/\sigma_{hZ}^{SM}$ and $S_{model} = \sigma_{h_i a_j}/\sigma_{ref}$, where $\sigma_{h_i a_j}$ is the $h_i a_j$ production cross section and σ_{ref} is the reference cross section defined in Ref. [1].

Benchmark point	A	B
m_{χ_1} (GeV)	7.4	7.4
$m_{\chi_1^\pm}$ (GeV)	118	118
m_{h_1} (GeV)	11.3	41.5
m_{a_1} (GeV)	18.7	19.3
$\Gamma_{Z\to\chi_1\chi_1}$ (GeV)	1.4×10^{-9}	1.4×10^{-9}
$\Gamma_{Z\to h_1 a_1}$ (GeV)	1.1×10^{-11}	4.9×10^{-12}
k	8.0×10^{-3}	1.3×10^{-2}
$S_{model}(e^+e^- \to h_1 a_1)$	1×10^{-10}	1×10^{-10}
$S_{model}(e^+e^- \to h_2 a_1)$	1×10^{-12}	2×10^{-12}
$\sigma_{e^+e^-\to\chi_1\chi_2}$ (pb)	1×10^{-5}	1×10^{-5}

where

$$\theta_{ha} = U_{u1}V_{u1} - U_{d1}V_{d1} + U_{01}V_{01} - U_{\ell 1}V_{\ell 1}, \tag{5.31}$$

and

$$p^2 = \frac{1}{4m_Z^2}\left[\left(m_Z^2 - (m_{h_1} + m_{a_1})^2\right)\left(m_Z^2 - (m_{h_1} - m_{a_1})^2\right)\right]. \tag{5.32}$$

For the benchmark point, the partial decay widths in both cases are given by

$$\begin{aligned} \Gamma_{Z\to\chi_1\chi_1} &= 1.4 \times 10^{-9}\ \text{GeV}, \\ \Gamma_{Z\to h_1 a_1} &= 1.1 \times 10^{-11}\ \text{GeV}, \end{aligned} \tag{5.33}$$

which is well within the measurement error.

Another bound on the model comes from scalar and pseudoscalar direct production at LEP. At LEP a light scalar can be produced by Higgsstrahlung process $e^+e^- \to Z \to Zh_1$. Ref. [184] gives a bound on the coupling strength of Z pairs to scalars regardless of the scalar's decay mode. The bound is given in terms of the quantity

$$k(m_h) = \frac{\sigma_{hZ}}{\sigma_{hZ}^{SM}}. \tag{5.34}$$

In our model, $k(m_h)$ is given by

$$k(m_{h_i}) = \frac{1}{v_{\rm ew}^2} \left| v_u V_{ui} + v_d V_{di} + v_0 V_{0i} + v_\ell V_{\ell i} \right|^2 , \tag{5.35}$$

and its value for the lightest scalar at our benchmark point is

$$k(m_{h_1}) = 8.0 \times 10^{-3}. \tag{5.36}$$

The bound on $k(m_h)$ for the benchmark point h_1 mass is given by

$$k(11.3 \text{ GeV}) \leq 0.09. \tag{5.37}$$

Therefore $k(m_{h_1})$ does not exceed the bound from Higgsstrahlung process in our benchmark point. The pseudoscalar can also be produced at LEP by the process $e^+e^- \to Z \to ha$. In the benchmark point, both h_1a_1 and h_2a_1 production are kinematically allowed. LEP bounds on scalar and pseudoscalar production for various final states are given in Ref. [1]. The bound is given in term of $S_{95} = \sigma_{max}/\sigma_{ref}$ where σ_{max} is the largest cross section compatible with data and σ_{ref} is the standard model hZ production cross section multiplied by a kinematic scaling factor. Defining $S_{model} = \sigma_{h_ia_j}/\sigma_{ref}$, where $\sigma_{h_ia_j}$ is the model's h_ia_j production cross section, the bound on the model is given by $S_{model} < S_{95}$. For our benchmark point, S_{model} is given by

$$\begin{aligned} S_{model}(e^+e^- \to h_1a_1) &= 1 \times 10^{-10}, \\ S_{model}(e^+e^- \to h_2a_1) &= 1 \times 10^{-12}, \end{aligned} \tag{5.38}$$

which is lower than the bound, $S_{95} \sim \mathcal{O}(10^{-2})$, in both cases.

We note that the lightest chargino mass is 118 GeV for the benchmark point, which exceeds the PDG bound of 94 GeV [5]. In the case of a long lived chargino however, the bound can be made much stronger and is currently at 171 GeV. We have calculated the lifetime of the chargino in our model assuming a stau mass of 110 GeV and have found that it is short lived, thus this latter bound is not of concern. We should point out however, that our analysis has been done at tree level. Loop corrections could change these results but are beyond the scope of this dissertation.

Finally, we need to calculate the bound on neutralino productions. Ref. [185] discusses the bound on production of the lightest and second to lightest neutralinos at LEP, $e^+e^- \to \chi_1\chi_2$, where χ_2 decays into $\chi_1 f\bar{f}$. Assuming that the selectron is much heavier than the Z, the main contribution comes from s-channel Z exchange. For our benchmark point, we calculate the cross section to be

$$\sigma_{e^+e^-\to\chi_1\chi_2} = 1 \times 10^{-5} \text{ pb}, \tag{5.39}$$

while the bound is $\mathcal{O}(0.1)$ pb. A summary of all these bounds is given in Table 5.3.

The light particles are mostly singlet and have very little mixing with the Higgs sector. This make the particles unlikely to be produced at near future experiments. However the heavier sector has a richer phenomenology. For example, heavier scalars are mostly h_u, h_d, h_0, and h_ℓ therefore they have a better chance of being detected in future colliders [175].

5.6 Conclusions

In this chapter, we have presented a supersymmetric model of 7 − 10 GeV dark matter, which is capable of describing the FGST observations. In a recent analysis of FGST data, Hooper and Goodenough found an excess in gamma ray emission from within 1.25° of the Galactic Center. They showed that this can be explained by annihilating dark matter if the dark matter has a mass between $7-10$ GeV, annihilates into τ-pairs most of the time, but into hadronic channels the other $15-40\%$ of the time, and $\langle \sigma v \rangle$ falls within the range $4.6 \times 10^{-27} - 5.3 \times 10^{-26}$ cm^3/s [170]. Our model achieves these requirements by minimally extending the SLHM to include a scalar singlet whose superpartner is the dark matter particle. Due to the Yukawa structure of the SLHM the scalar particles mediating the dark matter annihilation have an enhanced coupling to leptons. This provides a natural means for satisfying the second requirement put forward by Hooper and Goodenough.

We have shown that this model produces the correct dark matter thermal relic density and is consistent with current collider bounds. In addition, we have shown that this model is consistent with the direct detection signals reported by both CoGeNT and DAMA for certain regions of parameter space, while for other regions of parameter space, the model yields a spin independent cross section far below the present CDMS bound, but maintains the right relic density and continues to explain the FGST observations. Thus our model is fully able to accommodate the results reported by CoGeNT and DAMA in the case of their vindication, but it is in no way contingent upon their validity.

CHAPTER 6

Taking a Razor to Dark Matter Parameter Space at the LHC[10]

6.1 Introduction

Through precision cosmological measurements, we have uncovered many of the general properties of dark matter (DM) in the cosmos. However, further determinations of the properties of DM and its distribution throughout the universe will require probing beyond its gravitational interactions. Although there is considerable effort underway to indirectly observe DM through the signatures of DM annihilations in places of high expected density, such as the centers of our galaxy, galaxy clusters and dwarf galaxies, there is no substitute for detection of DM in a controlled lab setting. To this end, there are many experiments presently searching for direct observation of DM scattering off nuclei in underground labs. Intriguingly, both indirect and direct searches are finding interesting anomalies that are consistent with what is expected from DM. Unfortunately, there is also considerable confusion since

---

[10] Preprint arXiv:1203.1662, submitted to Physical Review D.

many of these excesses could also be consistent with backgrounds or systematic effects. Furthermore, both the indirect and direct search techniques rely on inputs from astrophysics, such as the spatial and velocity distribution of the DM in our galaxy, or the spectrum and morphology of high energy gamma and cosmic rays, which are notoriously difficult to estimate.

High energy colliders provide an alternative [53], complementary way to search for DM that is independent of assumptions about astrophysical quantities. If DM is to be found in direct detection experiments then it must couple to quarks or gluons, and thus it is possible to directly produce DM in high energy hadron colliders. Since DM carries no SM charge, it will leave the detector without further interactions, resulting in a missing (transverse) energy signature ($\not{E}_T$). Thus, the observation of an excess of events in channels involving missing energy could provide tantalizing evidence of the production of DM, and from these channels, DM properties such as its mass could be determined. Similarly, if there are no observed excesses, one can place limits on the size of putative DM-quark/gluon couplings. These collider limits can be re-expressed as a limit on DM-nucleon couplings and compared to the limits that come from the absence of events in dedicated direct detection experiments such as CDMS [10] and XENON100 [23].

Many models of beyond the standard model (BSM) physics contain a viable DM candidate, and thus predict events involving $\not{E}_T$. Many ingenious search strategies have been developed within the context of particular models, but these strategies often rely on other unique and unrelated features specific to the model. Furthermore, without independent evidence for any of these models, and armed only with the knowledge that DM exists, it is worthwhile to consider more model independent search strategies. The simplest final state that could involve the production of DM and serve as a limit on its couplings is a monojet/monophoton in association with missing energy. At the Tevatron, a search for $j + \not{E}_T$ that was originally designed to search for large extra dimensions [186, 187] has been recast as a constraint on DM production, both through contact interactions of DM and the SM [54–56], and through the presence of a light mediator particle [55, 188, 189]. These analyses were based on ~ 1 fb^{-1} of data and a simple cut-and-count approach. Recently, CDF has carried out a dedicated search for DM in the monojet channel, using 6.7 fb^{-1} and the full shape information contained in the monojet spectrum [190]. For heavy DM, these bounds can be improved upon by going to the LHC, and analyses of monojets [20, 57, 189] and monophotons [20] have been carried out on ~ 1 fb^{-1} of data. Very recently CMS has released a DM search in the monophoton channel [59]. Constraints from LEP monophoton and missing energy searches have also been calculated [60, 61].

Although the monojet/monophoton is certainly the simplest final state one can expect to find DM, it does not necessarily result in the strongest limits[11]. At the high collision energies typical of the LHC, one expects a hard process to be accompanied by several high p_T jets, and the veto required to fit into the one jet topology may restrict the signal efficiency. In addition, events with multiple jets contain more information, such as inter-jet angles. As we shall see, optimizing searches with respect to these variables may improve the ratio of signal to background efficiencies. There are approaches such as the CMS "monojet" search [192] which allow a second hard jet as long as the topology is sufficiently far from back-to-back that QCD backgrounds are suppressed. We take this philosophy one step further and investigate a more inclusive search approach that allows an arbitrary number of hard jets, as long as there is also considerable missing energy, see also [193]. We base our strategy around that used by the CMS "razor" analysis [194, 195], which was originally employed to search for supersymmetry, and was based on approximately 800 pb^{-1}

---

[11] As has recently been discussed [191], if there is a light mediator coupling the SM to DM, searches for the mediator in the dijet channel are a complementary way to constrain the DM and its couplings.

of data.

This chapter is outlined as follows. In Sec. 6.2, we introduce both the effective theory of DM coupling to quarks through contact operators, and some simplified models which UV complete these by introducing a mediator light enough to be accessible at the LHC. We describe the razor analysis in Sec. 6.3, beginning with a description of the analysis in Sec. 6.3.1. In Sec. 6.3.3, we outline our results for the case of contact operators and in Sec. 6.3.5, we compare the collider bounds with direct detection bounds. Finally, we address the issues that arise with light mediators and the validity of using an effective theory in Sec. 6.4.

6.2 A Simplified Model of Dark Matter Interactions

As mentioned above, searches for DM in many models of BSM physics utilize additional features of the model, such as production of colored states that ultimately decay to DM. Here, we wish to follow an approach that is more model independent and we introduce simplified models [196] that couple DM to the SM. In addition to the SM, these models contain the DM, χ, which we assume to be a Dirac fermion [12], and a mediator particle that couples to the DM and states in the SM. The nature of the mediator will determine the form of the SM-DM coupling and whether the non-relativistic limit is spin-independent (SI) or spin-dependent (SD). We will consider vector, axial-vector, and scalar mediators, which give a representative sample of the different behaviors possible at colliders and direct detection experiments; for a more complete list of possibilities see for example [56, 197].

We start by considering the limit of the simplified model where only the DM

---

[12] This choice has little effect on our results, although the vector coupling would not be allowed for the case of Majorana DM.

is accessible at colliders [193], and the mediator is integrated out. In this limit, with very heavy mediators ($\gtrsim$ few TeV), we can use the framework of effective field theory. The resulting effective operators for each choice of mediator are:

$$\begin{aligned}
\mathcal{O}_V &= \frac{(\bar{\chi}\gamma_\mu\chi)(\bar{q}\gamma^\mu q)}{\Lambda^2}\,, && (6.1)\\
\mathcal{O}_A &= \frac{(\bar{\chi}\gamma_\mu\gamma_5\chi)(\bar{q}\gamma^\mu\gamma_5 q)}{\Lambda^2}\,, && (6.2)\\
\mathcal{O}_G &= \alpha_s\frac{(\bar{\chi}\chi)(G^a_{\mu\nu}G^{a\mu\nu})}{\Lambda^3}\,, && (6.3)
\end{aligned}$$

where q is a SM quark field and $G^a_{\mu\nu}$ is the gluon field strength tensor. Note that in the case of $\mathcal{O}_G$ the coupling between gluons and the scalar mediator comes about at one-loop and involves an additional heavy colored state. In Sec. 6.4, we will discuss whether this effective theory approach is valid and the effects of keeping the mediator in the simplified model. We calculate the bounds for the up and down quarks separately, but the bound for any linear combination of quark flavors can be derived from these bounds [20].

We ultimately want to compare collider bounds to direct detection bounds. Here, the effective theory in equations (6.1)-(6.3) is always valid. In order to match the quark-level operators to nucleon-level operators, the coupling between the SM and DM must be of the form $\mathcal{O}_{SM}\mathcal{O}_\chi$, where $\mathcal{O}_{SM}$ contains only SM fields and $\mathcal{O}_\chi$ involves only DM such that we can extract the matrix element $\langle N|\mathcal{O}_{SM}|N\rangle$ [198]. At colliders, for a Dirac fermion χ, both $\mathcal{O}_V$ and $\mathcal{O}_A$ contribute to χ production with roughly equal rates. However, in direct detection experiments, the spin-independent $\mathcal{O}_V$ dominates over the spin-dependent $\mathcal{O}_A$. $\mathcal{O}_V$ vanishes if we change our assumption to Majorana DM.

6.3 Razor

In this section, we derive bounds on DM operators with the razor analysis. We begin with a description of the general razor analysis as used by CMS [199]. We then compare the shape of signal and background events in the razor variables, M_R and R^2, and identify cuts which are optimal for searching for dark matter. To test the sensitivity of this search we compare the results of such a razor analysis with 800 pb^{-1} to a mono-jet analysis which uses 1 fb^{-1} [20], and show how the bounds from these two complementary analyses can be combined[13].

6.3.1 The Razor Variables

The objective of the razor analysis is to discriminate the kinematics of heavy pair production from those of the SM backgrounds, without making any strong assumptions about the $\not{E}_T$ spectrum or the details of the subsequent decay chains. Furthermore, background events follow very clean exponential distributions in the razor variables which allow for data-driven analyses to be carried out, without heavy use of Monte-Carlo simulations to predict backgrounds.

The baseline selection requires at least two reconstructed objects in the final state, *i.e.* calorimetric jets or electrons and muons that satisfy lepton selection criteria. These objects are combined into two "megajets". In our analysis most events contain only two jets in which case each jet is promoted to a megajet, but in the most general case the megajets are created using a "hemisphere" algorithm described below [200]. The hemispheres are defined by $P_i (i = 1, 2)$ which is the sum of the momenta of high p_T objects in the hemisphere. The high p_T objects k in hemisphere i satisfy $d(p_k, P_i) < d(p_k, P_j)$ where $d(p_k, P_i) \equiv (E_i - |\vec{P}_i| \cos\theta_{ik}) \frac{E_i}{(E_i+E_k)^2}$,

---

[13] We use 800 pb^{-1} of data to match the most recent razor search, but our techniques can easily adapted to upcoming updates to this analysis.

and θ_{ik} is the angle between $\vec{P}_i$ and $\vec{p}_k$. The hemisphere axes, P_i, are defined by the following algorithm.

1. Assign P_1 to the object (jet, lepton, photon) with the highest p_T and P_2 to the object that gives the largest invariant mass as a pair with P_1. The four-momenta P_1, P_2 are the seeds for the hemisphere axes.
2. Go through the rest of the objects in the event, ordered by p_T, and assign p_k to hemisphere 1 if $d(p_k, P_1) < d(p_k, P_2)$, or 2 otherwise.
3. Redefine P_i as the sum of the momenta in the i^{th} hemisphere.
4. Repeat 2-3 until all objects are assigned to a hemisphere.

The two megajet four-momenta are taken to be the two hemisphere axes, P_1 and P_2.

In addition to this hemisphere algorithm for defining the megajets we also considered a simple approach where the n objects in an event are partitioned into two groups in all possible $(2^{n-1} - 1)$ ways and the partition that minimizes the sum of the megajet invariant mass-squared is chosen. The two hemisphere algorithms give similar results.

The razor frame is the frame in which the two megajets are equal and opposite in the $\hat{z}-$ (beam) direction. In this frame, the four-momenta of the megajets are

$$p_{j_1} = \left(\frac{1}{2} \left[M_R - \frac{(\vec{p}_T^{j_1} - \vec{p}_T^{j_2}) \cdot \vec{\not{E}}_T}{M_R} \right], p_T^{j_1}, p_z \right) , \tag{6.4}$$

$$p_{j_2} = \left(\frac{1}{2} \left[M_R + \frac{(\vec{p}_T^{j_1} - \vec{p}_T^{j_2}) \cdot \vec{\not{E}}_T}{M_R} \right], p_T^{j_2}, -p_z \right) , \tag{6.5}$$

where M_R is the longitudinal boost invariant quantity, defined by

$$M_R = \sqrt{(E_{j_1} + E_{j_2})^2 - (p_z^{j_1} + p_z^{j_2})^2} \ . \tag{6.6}$$

The other longitudinally invariant razor observables are

$$M_R^T = \sqrt{\frac{\not{E}_T(p_T^{j_1} + p_T^{j_2}) - \vec{\not{E}}_T \cdot (\vec{p}_T^{j_1} + \vec{p}_T^{j_2})}{2}}\,, \tag{6.7}$$

$$R = \frac{M_R^T}{M_R}\,, \tag{6.8}$$

here $p_T = |\vec{p}_T|$. Note that the missing transverse energy, $\vec{\not{E}}_T$ is calculated from all activity in the calorimeters whereas $\vec{p}_T^{j_{1,2}}$ involve just the jets above our cuts.

M_R provides an estimate of the underlying scale of the event. M_R^T is the transverse observable that also estimates event-by-event the value of the underlying scale. The "razor" variable R^2 is designed to reduce QCD multijet background to manageable levels. R is correlated with the angle between the megajets. Events where the two mega-jets are roughly co-linear have $R^2 \sim 1$ while events with back-to-back megajets have small R^2. In general R^2 has a maximum value of approximately 1, and the QCD multijet background peaks at $R^2 = 0$. Thus, by imposing a cut on R^2, one can essentially eliminate the QCD multijet background.

6.3.2 Analysis

The razor analysis uses a set of dedicated triggers which allow one to apply low thresholds on M_R and R^2. The events that pass the triggers are then classified into six disjoint boxes which correspond to different lepton selection criteria [201]. For our purposes, we consider only the HAD box which contains all the events that fail lepton requirements, described below. After QCD is removed using a strong R^2 cut, the dominant backgrounds to our process are $(Z \to \bar{\nu}\nu)$+jets, $(W \to \ell^{inv}\nu)$+jets, $(W \to \tau^h\nu)$+jets, and $t\bar{t}$, where ℓ^{inv} denotes a lepton that is missed in the reconstruction, and τ^h is a hadronically decaying tau-lepton. We have simulated the dominant SM backgrounds using MadGraph5 [202] at the matrix element level,

TABLE 6.1: Background and signal (for $m_\chi = 100$ GeV and $\Lambda = 644$ GeV) cross sections (in pb) before and after analysis cuts. The matching scale is taken to be 60 GeV, see text for details.

	$n_j = 0$	$n_j = 1$	$n_j = 2$	$n_j = 3$	After cuts
$(Z \to \bar{\nu}\nu)$+jets	3960	470	150	33.7	18×10^{-2}
$(W \to \ell^{inv}\nu)$+jets	10585	836	317	96.5	2.0×10^{-2}
$(W \to \tau^h\nu)$+jets	5245	676	160	48.8	6.8×10^{-2}
$t\bar{t}$	12.4	–	–	–	1.5×10^{-3}
$\bar{\chi}\chi$	5.46	2.31	0.77	0.33	4.3×10^{-2}

Pythia 6.4 [165] for parton showering and hadronization, and PGS [203] as a fast detector simulation. We generate $W/Z+n$ jets, where $n = 1, 2, 3$ for the background, and use MLM matching [14] [204] with a matching scale of 60 GeV. We generate both matched and unmatched samples for our signal, and find that the matched sample gives approximately a 15% increase in the number of events passing our analysis cuts, as compared to the unmatched sample. In what follows, we use unmatched samples for the signal events; using a matched sample will increase our bounds by a few GeV but does not change our conclusions. The cross sections for the dominant backgrounds, and an example signal point, are shown in Table 6.1.

Following [199], in every event we require jets to have $p_T > 60$ GeV, $|\eta| < 3.0$. Electrons(muons) are required to have $p_T > 20(10)$ GeV and $|\eta| < 2.5(2.1)$, and we include τ-leptons, which decay hadronically, in our definition of jets. Only events in which $\Delta\phi$ between the two megajets is less than 2.8 are kept. With these requirements the events will pass the dedicated razor triggers, although they would often fail those for other analyses *e.g.* α_T, H_T. One advantage of the razor analysis lies in the simple shape of the SM background distributions; the M_R and R^2 distributions are simple exponentials for a large portion of the $R^2 - M_R$ plane. By fitting the distributions of the razor variables M_R and R^2 to an exponential function,

---

[14] M.L. Mangano matching scheme.

one can utilize a data-driven description of the background without having to rely on Monte Carlo (MC) estimates. Since we do not have access to the data, we must carry out a MC based analysis. As a check of the validity of our MC analysis we compare our results to the yields found by CMS in different bins of R^2 and M_R. We find that our MC simulations for the background in the HAD box fall within the expected 68% range expected by CMS, and thus are consistent with the CMS simulations (see Fig. 9 of Ref. [199]), which in turn agree well with data.

6.3.3 Signal and Background Shapes

The shape of the M_R and R^2 distributions for the dominant backgrounds and a sample signal are shown in Fig. 6.1. The dependence of the signal shape on dark matter mass is shown in Fig. 6.2. The signal shapes when dark matter couples to sea quarks or to gluons are shown in Fig. 6.3. The shapes depend on the scale and the kinematics of the production process. The location of the M_R distribution peak is determined by the event scale and kinematic cuts. The M_R distributions of $(Z \to \bar{\nu}\nu)$+jets, W+jets, and $\bar{\chi}\chi$+jets all peak at approximately the same value of $M_R \approx 200$ GeV, whereas the M_R peak for $t\bar{t}$ is higher due to the inclusion of tops in the megajets.

The shape of R^2 distribution is affected by the kinematics of the process and is somewhat different for signal and background. Background events are highly peaked at low R^2, where the megajets are more back-to-back, whereas signal events are more evenly distributed in R^2, with a significant population at high R^2. The difference in event shapes, signal events being more likely to produce collinear megajets, originated from different diagrams which dominate production.

The SM backgrounds are dominated by invisible decays of a Z boson, see Table 6.1, for which the dominant production mechanism at the LHC is through quark-

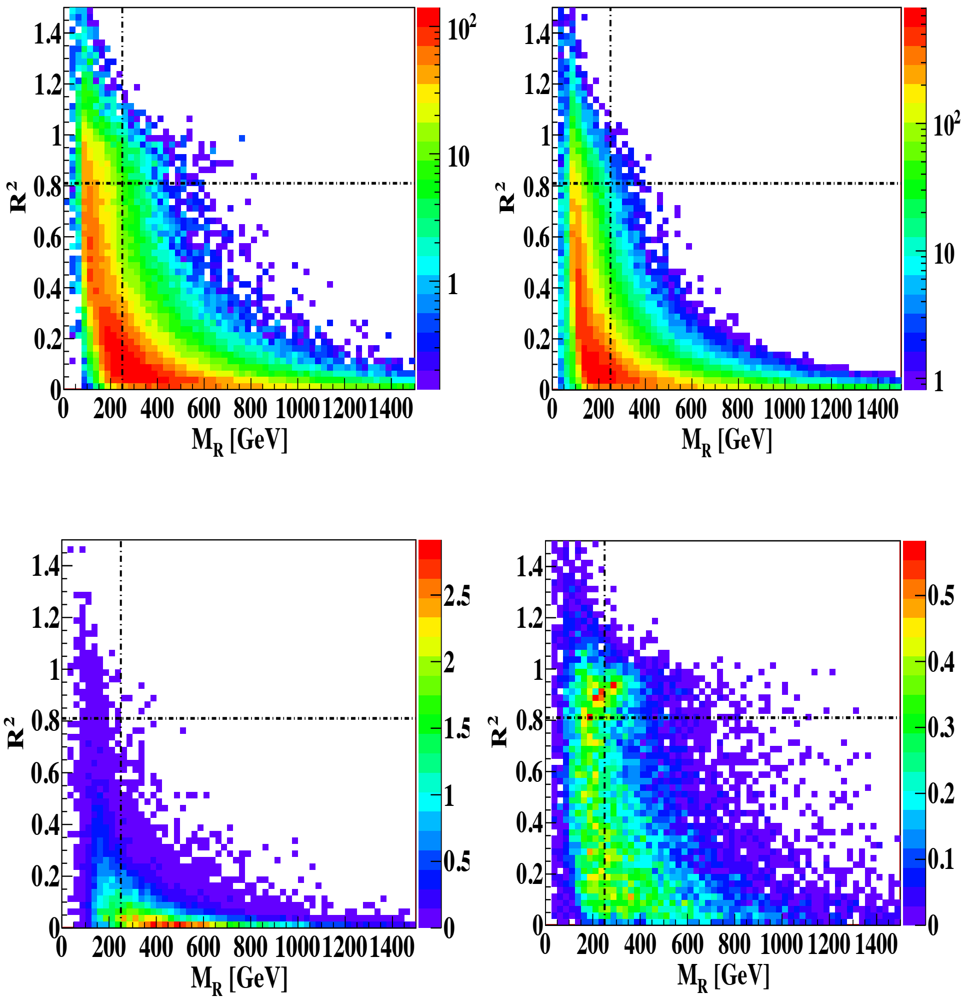

(c) $t\bar{t}$.

(d) Signal (M_χ = 100 GeV, Λ = 644 GeV).

FIG. 6.1: R^2 vs. M_R distribution for SM backgrounds (a) ($Z \to \bar{\nu}\nu$)+jets, (b) W+jets (including decays to both ℓ^{inv} and τ^h, (c) $t\bar{t}$, and (d) DM signal with $M_\chi = 100$ GeV and $\Lambda = 644$ GeV. In all cases the number of events are what is expected after an integrated luminosity of 800 pb^{-1}. The cuts applied in M_R and R^2 are shown by the dashed lines and the "signal" region is the upper right rectangle.

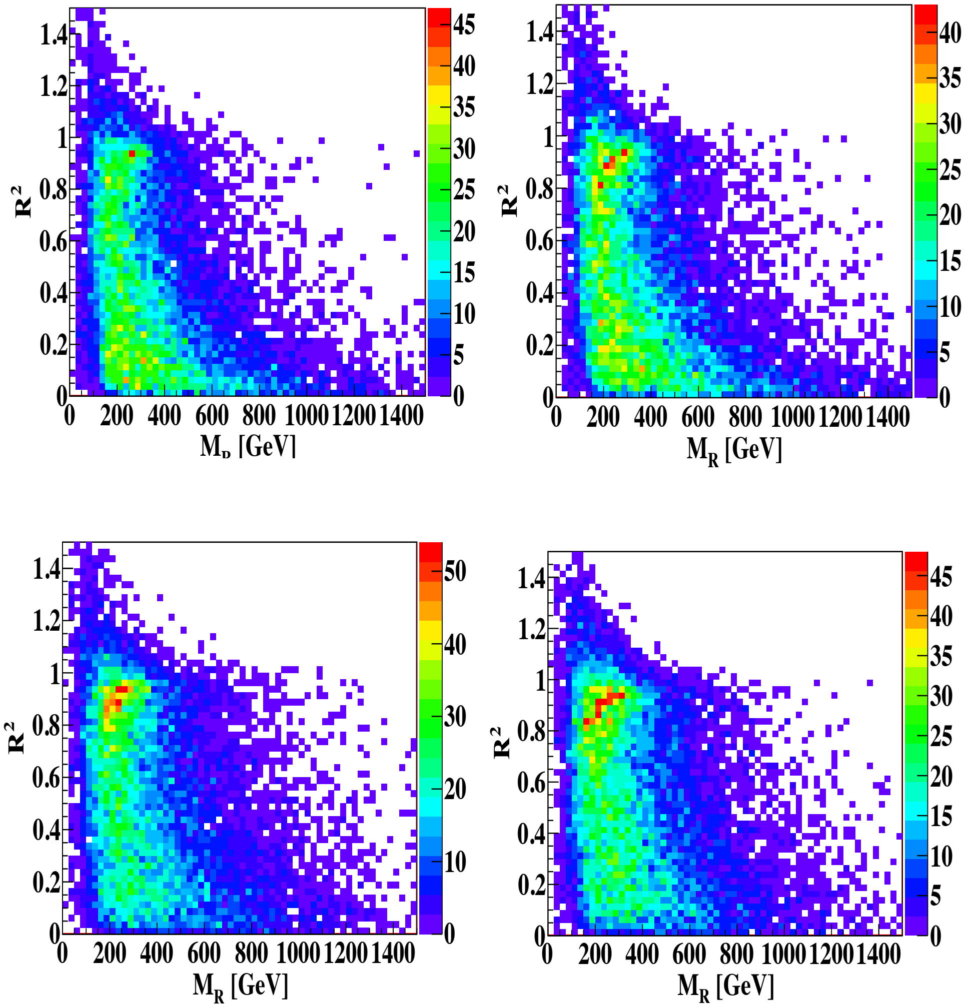

(c) $M_\chi = 800$ GeV.

(d) $M_\chi = 1000$ GeV.

FIG. 6.2: R^2 vs. M_R for various DM masses with u-only vectorial couplings with arbitrary normalization.

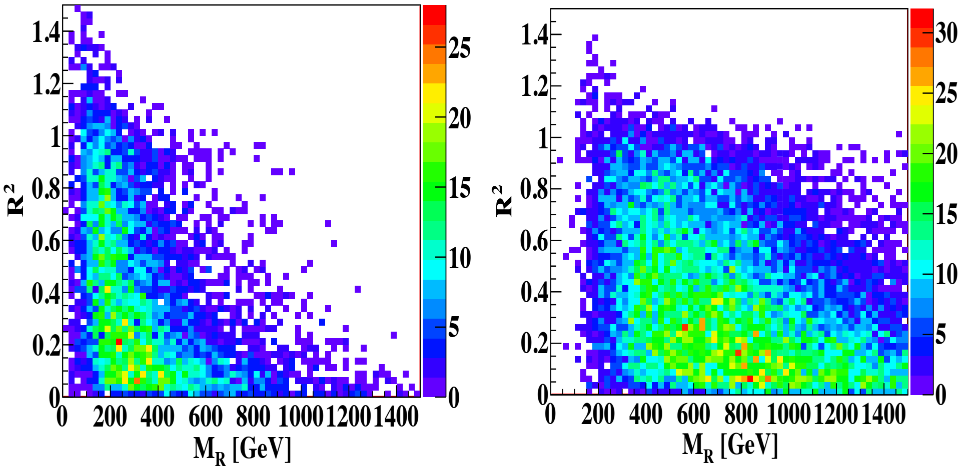

(a) Sea quark couplings.

(b) Gluon couplings.

FIG. 6.3: R^2 vs. M_R for DM coupling to (a) sea quarks (in this case the s-quark) and (b) gluons with arbitrary normalization.

gluon collisions with $q\bar{q}$ collisions giving a much smaller contribution. In quark-gluon collisions the Z tends to be emitted in the backward direction (close to the beam from which the gluon came). This tends to give the Z a lower p_T compared to events which originate in $q\bar{q}$. Due to the high p_T cuts on the individual jets their transverse momenta must largely cancel to balance the Z. Thus, the $\Delta\phi$ distribution is peaked near π for background.

On the other hand, signal events are dominantly produced from the $q\bar{q}$ initial state. This is because $q\bar{q}$ and qg initiated cross sections scale differently with the invariant mass of the dark matter pair. This is reminiscent of the scaling of $Z+j$ at LHC, where the gq-initiated cross section is proportional to m_Z^2 while the $q\bar{q}$-initiated one scales like m_Z^4. If the Z mass were higher, $Z+j$ would have been dominantly $q\bar{q}$-initiated. Similarly in our case DM production is dominatly $q\bar{q}$-initiated because the $\chi\bar{\chi}$ invariant mass (analogous to the Z mass above) is typically far above the weak scale, see Figure 6.8. This difference in production mechanisms results in a more isotropic distribution of the jets and consequently a different distribution in R^2, tending more towards high values. This difference increases as DM mass increases, as the peak in R^2 also moves higher as DM mass increases (Fig. 6.2) while the M_R distribution remains approximately the same. The difference in production mechanisms remains at NLO, which we have checked using MCFM [15] [205, 206].

We also find that the M_R and R^2 distributions for DM coupling to sea quarks, shown in Fig. 6.3, are similar to those of background. This is because for sea quarks the dominant production is qg (as well as $\bar{q}g$) because of their smaller PDF's, which is similar to the dominant background production mechanism. For coupling to gluons, where the gg initial state dominates, the distribution gives a more even coverage of the $M_R - R^2$ plane, as seen in Fig. 6.3.

6.3.4 Results

Based on the distributions shown in Figs. 6.1, 6.2, and 6.3, we find that our optimal signal region is $M_R \geq 250$ GeV and $R^2 \geq 0.81$. We use the number of events in the signal region, the upper right rectangle in Fig. 6.1, to place constraints on the cutoff scale Λ. At 90% exclusion, we require

$$\chi^2 \equiv \frac{N_{DM}(m_\chi, \Lambda)^2}{N_{DM}(m_\chi, \Lambda) + N_{SM} + \sigma_{SM}^2} \leq 2.71\,, \tag{6.9}$$

where N_{DM} is the expected number of signal events for a given DM mass m_χ and scale Λ, N_{SM} is the expected number of background events, and σ_{SM} is the uncertainty in the predicted number of background events. Through our Monte Carlo simulations, we estimate that the number of background events is 144.0 for $(Z \to \bar{\nu}\nu)$+jets, 70.4 for W+jets, and 1.2 for $t\bar{t}$, giving a total of $N_{SM} = 215.6$ for a luminosity of 800 pb^{-1}, the approximate amount used in the Razor analysis [199]. The $t\bar{t}$ background does not give a large contribution since the majority of events

---

[15] Monte Carlo for FeMtobarn processes.

with significant $\not{E}_T$ are vetoed by the presence of leptons in the events and do not pass our cuts. We did not attempt to calculate the QCD background since we expect a negligible number of events from this channel in our signal region. The error σ_{SM} in the razor analysis is statistics dominated which implies $\sigma_{SM} \sim \sqrt{N_{SM}}$. We adopt this value as our default value for the standard model uncertainty, but to be conservative we will also present the limit in the case where there is an additional and equal source of systematic error. The calculated bound for vector and axial couplings of DM to valence quarks is given in Fig. 6.4, where we see that the existing razor analysis gives bounds that are competitive with the monojet results. We present the limit as a band extending between the two assumptions for the uncertainty $\sigma_{SM} = \sqrt{N_{SM}}$ and $\sigma_{SM} = 2\sqrt{N_{SM}}$. In the rest of the chapter we use the $\sqrt{N_{SM}}$ limit which we expect to be realistic. Note that, there is no significant difference between the bounds for vector or axial couplings. This implies that as opposed to direct detection, spin dependent limits will be just as strong as spin independent ones.

The razor analysis requires at least two jets in the final state, so the data set is complementary to that used in the monojet search. Since the bounds are slightly, but not hugely, stronger than those from monojet there is utility in combining the bounds from the razor and monojet analyses. We do this by solving

$$\chi^2_{\text{monojet}}(m_\chi, \Lambda) + \chi^2_{\text{razor}}(m_\chi, \Lambda) = 2.71\,, \tag{6.10}$$

where the χ^2 are defined in Eq. 6.9. We find that the combined bound is a few percent higher than the razor bound alone (Fig. 6.5).

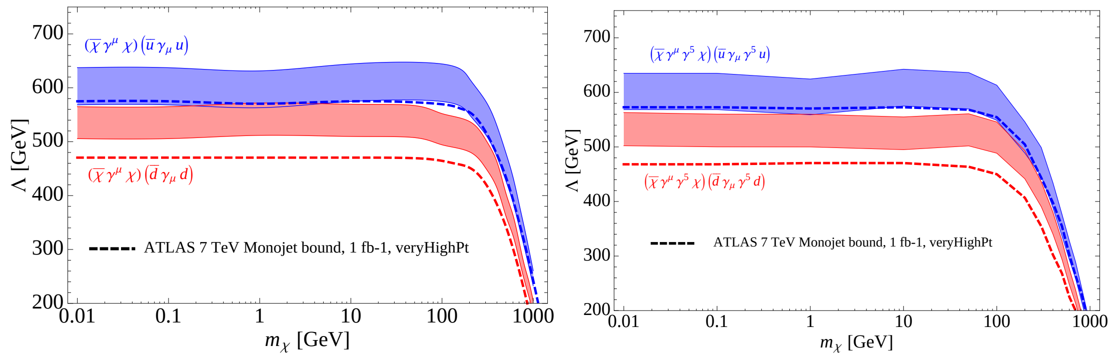

(a) Vector couplings. (b) Axial couplings

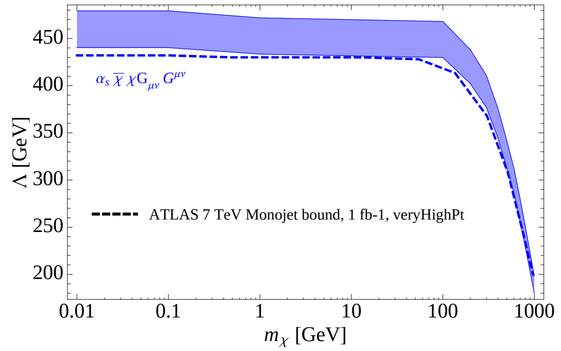

(c) Gluon couplings

FIG. 6.4: Cutoff scale Λ bounds for vector, axial, and gluon couplings. The error band is determined by varying σ_{SM} between $\sqrt{N_{SM}}$ and $\sigma_{SM} = 2\sqrt{N_{SM}}$. The dashed line is the bound determined by the monojet analysis [20].

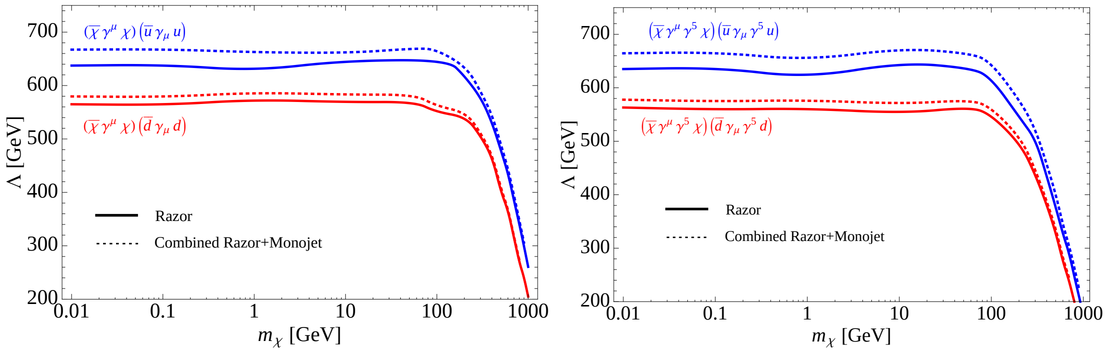

(a) Vector-coupling

(b) Axial-coupling

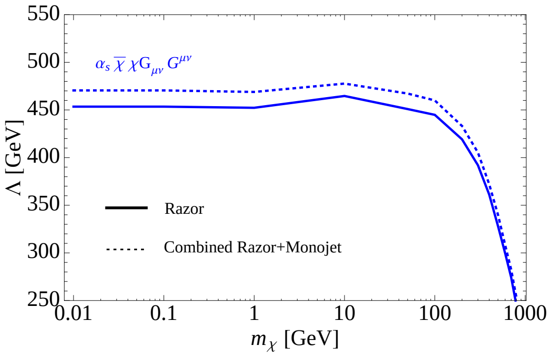

(c) Gluon-coupling

FIG. 6.5: Combined razor and monojet Λ bounds. The solid lines are the razor bounds and the dashed lines are the combined bounds.

6.3.5 Comparison with Direct Detection and Annihilation Cross Section

We now translate the collider bounds found above into constraints on direct detection scattering rates by following the approach of Ref. [20]. This allows us to show the collider limits in the standard $\sigma - m_\chi$ plane. We use the values found in [55] to calculate the coefficients required to translate the quark level matrix elements $\langle N|\bar{q}\gamma^\mu q|N\rangle$ and $\langle N|\bar{q}\gamma^\mu\gamma^5 q|N\rangle$ into the nucleon level matrix elements. For the matrix element of the gluon field strength in the nucleon, $\langle N|\alpha_s G^a_{\mu\nu}G^{a\mu\nu}|N\rangle = -\frac{8\pi}{9}\Big(m_N - \sum_{q=u,d,s}\langle N|m_q\bar{q}q|N\rangle\Big)$, we follow the approach of [207] using an updated value of the pion-nucleon sigma term $\Sigma_{\pi N} = 55$ MeV [208].

We make the simplifying assumption that the effective DM-SM couplings are universal in quark flavor. However, we can account for different u and d couplings (*i.e.* $c_u \neq c_d$, where the couplings to DM are of the form $c_{u(d)}/\Lambda^2$) by rescaling the collider limits on the DM-nucleon cross-section by a factor of $(\Lambda_u^4+\Lambda_d^4)/(c_u^2\Lambda_u^4+c_d^2\Lambda_d^4)$. The bounds on the DM-nucleon cross-sections for various operators can be found in Fig. 6.6. From the figure, we can see that collider experiments can probe DM mass regions below direct detection experiment thresholds. In the case of spin-independent scattering, the cross section bound obtained from $\mathcal{O}_G$ is 2-3 orders of magnitude below the cross-sections required to fit the excesses seen at DAMA, CoGeNT and CRESST. Moreover, the bound for $\mathcal{O}_G$ is competitive with the cross-section bounds obtained from CDMS and XENON experiments. The DM-nucleon spin-dependent scattering is not coherent over the whole nucleus, therefore the cross section bounds from spin-dependent experiments are lower then the bounds from spin-independent experiments. In this case, the collider experiments provide the strongest bound up to DM masses of ~ 1 TeV. The collider bounds weaken rapidly for higher DM mass since the center-of-mass energy required to create a pair of DM is higher.

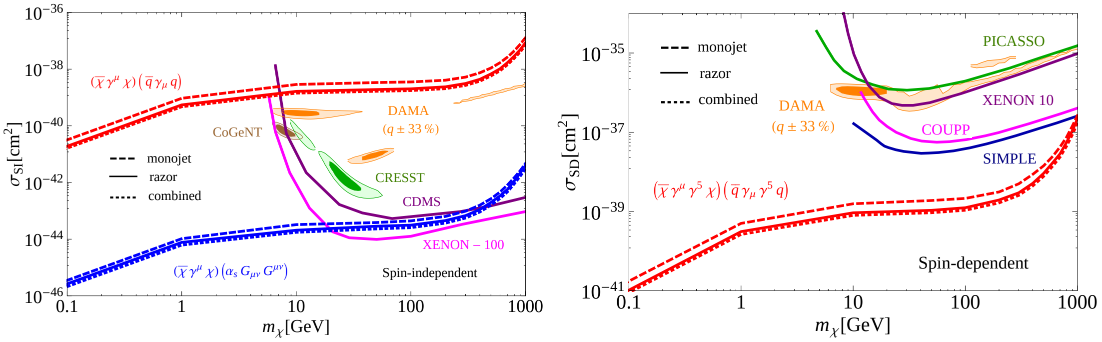

FIG. 6.6: Razor limits on spin-independent (LH plot) and spin-dependent (RH plot) DM-nucleon scattering compared to limits from the direct detection experiments. We also include the monojet limits and the combined razor/monojet limits. We show the constraints on spin-independent scattering from CDMS [10], CoGeNT [21], CRESST [4], DAMA [22], and XENON-100 [23], and the constraints on spin-dependent scattering from COUPP [24], DAMA [22], PICASSO [25], SIMPLE [26], and XENON-10 [27]. We have assumed large systematic uncertainties on the DAMA quenching factors: $q_{\rm Na} = 0.3 \pm 0.1$ for sodium and $q_I = 0.09 \pm 0.03$ for iodine [28], which gives rise to an enlargement of the DAMA allowed regions. All limits are shown at the 90% confidence level. For DAMA and CoGeNT, we show the 90% and 3σ contours based on the fits of [29], and for CRESST, we show the 1σ and 2σ contours.

In addition to the direct detection bounds, we can also convert the collider bounds into a DM annihilation cross-section, which is relevant to DM relic density calculations and indirect detection experiments. The annihilation rate is proportional to the quantity $\langle \sigma v_{rel} \rangle$, where σ is the DM annihilation cross section, $v_{\rm rel}$ is the relative velocity of the annihilating DM and $\langle . \rangle$ is the average over the DM velocity distribution. The quantity $\sigma v_{\rm rel}$ for $\mathcal{O}_V$ and $\mathcal{O}_A$ operators is

$$\begin{aligned}
\sigma_V v_{\rm rel} &= \frac{1}{16\pi\Lambda^4} \sum_q \sqrt{1 - \frac{m_q^2}{m_\chi^2}} \\
&\quad \times \left(24(2m_\chi^2 + m_q^2) + \frac{8m_\chi^4 - 4m_\chi^2 m_q^2 + 5m_q^4}{m_\chi^2 - m_q^2} v_{\rm rel}^2 \right) \qquad (6.11) \\
\sigma_A v_{\rm rel} &= \frac{1}{16\pi\Lambda^4} \sum_q \sqrt{1 - \frac{m_q^2}{m_\chi^2}} \left(24m_q^2 + \frac{8m_\chi^4 - 22m_\chi^2 m_q^2 + 17m_q^4}{m_\chi^2 - m_q^2} v_{\rm rel}^2 \right) \qquad (6.12)
\end{aligned}$$

As in the case of direct detection, we assume universal DM couplings in quark flavor. In Fig. 6.7, we show $\langle \sigma v_{\rm rel} \rangle$ as functions of the DM mass, taking $\langle v_{rel}^2 \rangle = 0.24$, which corresponds to the average DM velocity during the freeze-out epoch. A much smaller average $\langle v_{rel}^2 \rangle$, e.g. in the galactic environment, would lead to stronger bounds. If the DM has additional annihilation modes, the bounds weaken by a factor of $1/\text{BR}(\bar{\chi}\chi \to \bar{q}q)$. Assuming that the effective operator description is still valid during the freeze-out epoch, the thermal relic density cross-section is ruled out at 90 % C.L. for $m_\chi \lesssim 20$ GeV for $\mathcal{O}_V$, and $m_\chi \lesssim 100$ GeV for $\mathcal{O}_A$.

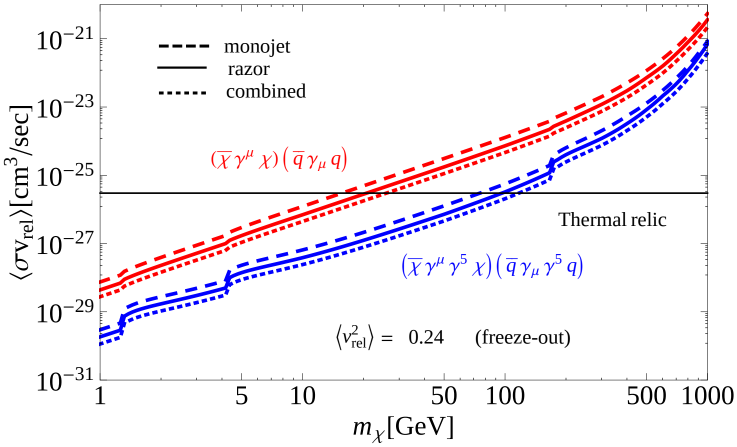

FIG. 6.7: Razor constraints on DM annihilation for flavor-universal vector or axial couplings of DM to quarks. We set $\langle v_{\rm rel}^2 \rangle = 0.24$ which corresponds to the epoch when thermal relic DM freezes out in the early universe. However, $\langle v_{\rm rel}^2 \rangle$ is much smaller in present-day environments (*i.e.* galaxies) which results in improved collider bounds on the annihilation rate. The horizontal black line indicates the value of $\langle v_{\rm rel}^2 \rangle$ required for DM to be a thermal relic.

6.4 Beyond Effective Theory

So far we have made the assumption that the effective theory valid at direct detection experiments, where the typical momentum transfer is of order 100 MeV, is also valid for calculating cross sections at the LHC, where the relevant scales are of order hundreds of GeV to a TeV. Given the large hierarchy between the scales probed at the two classes of experiments it is important to consider the possibility that this assumption is violated. In particular, the presence of new particles at or below the LHC scale can modify the bounds. In fact, the disparity between these scales is so large that it has been argued that due to unitarity limits, new physics beyond the DM particle *must* lie within the LHC's kinematic reach in order to generate direct detection cross sections as large as those discussed in the previous sections [189]. In this section, we will investigate these issues. We shall see that even if a new mediator must be within the LHC's reach, for DM masses below a couple of hundred GeV the mediator can easily be sufficiently heavy that it does not significantly affect the search in question. We will also find that when the new mediator is sufficiently light to modify the bounds the limits derived so far may be either strengthened or weakened, depending on the mass of the mediator relative to the LHC scale and relative to the mass of the DM particle. The issue of light mediators and how they affect mono-jet and mono-photon bounds on DM has also been discussed in [20, 55, 60, 188, 191, 209]. Furthermore, if the mediator is light it can also be searched for directly by looking for a dijet resonance or the dijet angular distribution [191].

6.4.1 Unitarity

In [189], it was shown that unitarity of $q\bar{q}$ forward scattering with a center of mass energy of $\sqrt{\hat{s}}$ places a limit on the production of DM at that energy. In particular, this argument places a lower bound on the cutoff scale Λ

$$\Lambda \gtrsim 0.4\sqrt{\beta(\hat{s})\hat{s}} \tag{6.13}$$

where β is the DM velocity which is always of order one and will hence be ignored. In [189], it was argued that an approximate requirement for the effective theory to be valid at the LHC is that this bound be satisfied at $\sqrt{\hat{s}} = \sqrt{s_*}$ which was set to 5

TeV. However, this requirement is not directly related to the search in question, as both our razor analysis and the monojet searches in [20, 57], do not probe scales of 5 TeV.

We wish to make direct contact between the unitarity limit in Eq. 6.13 and an actual collider search for DM. The first difficulty is that the unitarity argument places a limit on DM pair production at $\sqrt{\hat{s}}$ as opposed to DM plus any number of jets. The former does not yield observable signals at the collider. In order to make contact with more inclusive searches it is useful to interpret the limit in Eq. 6.13 as a limit, not on the energy of the incoming quarks, but on the center of mass energy of the DM system, $m_{\chi\chi}$. For the exclusive process, $q\bar{q} \to \chi\bar{\chi}$, these two scales are obviously the same, but in an inclusive process, $q\bar{q} \to \chi\bar{\chi} + X$, it is not. This amounts to replacing the $\sqrt{\hat{s}}$ by the invariant mass of the DM system $m_{\chi\chi}$, or

$$m_{\chi\chi} < \frac{\Lambda}{0.4}\,. \tag{6.14}$$

This substitution allows us to make contact with any DM production process being probed at the collider.

We can now ask the following question. Assuming a contact interaction of quarks with DM with a cutoff scale Λ right at where we have set our limits, what fraction of the signal events violate Eq. 6.14 ? In Fig. 6.8 we show the invariant mass distribution of events passing our analysis cuts for a few DM masses. We show the unitarity limit of $\Lambda/0.4$ as a dashed vertical line. Events that violate the bound are guaranteed to be sensitive to the physics that mediates the interaction of quarks and DM, and thus are not reliably described by the effective theory. Events that are to the left of the vertical line may be described by the effective theory, (unless the mediator is light, see below). For DM masses of 1 and 100 GeV, the fraction of events that violate the unitarity limit is 8% and 11% respectively. Thus,

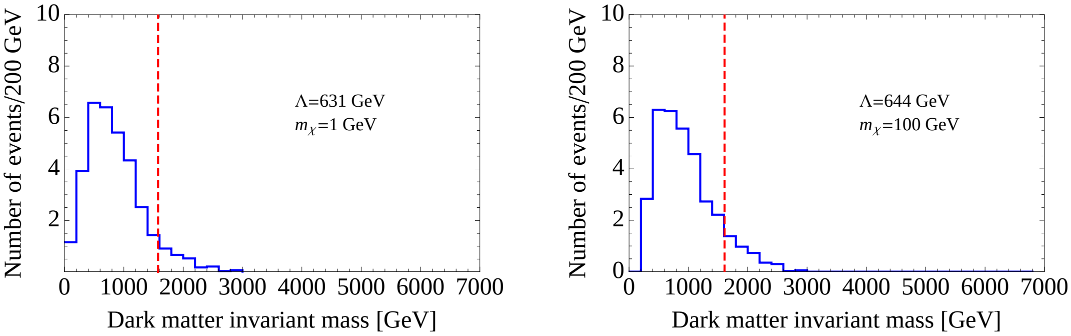

(a) $m_\chi = 1$ GeV (b) $m_\chi = 100$ GeV

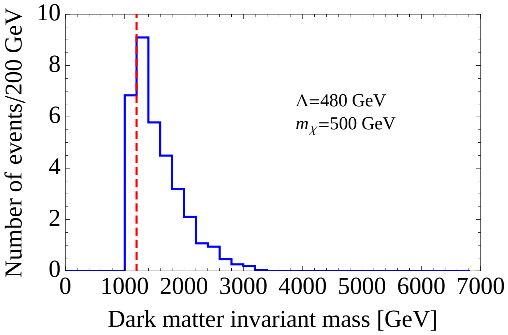

(c) $m_\chi = 500$ GeV

FIG. 6.8: $m_{\chi\chi}$ distribution for signal events with u-quark vector couplings with $R^2 > 0.81$ and $M_R > 250$ GeV. The red dashed line corresponds to the unitarity bound $m_{\chi\chi} = \Lambda/0.4$. The three panels show the distribution for DM masses of (a) 1 GeV, (b) 100 GeV, and (c) 500 GeV. The fractions of events which lie beyond the bound are 8%, 11% and 80% respectively.

the bound derived with the full effective theory may be accurate to within this precision, which we consider acceptable. The situation is different for heavier DM, *e.g.* 500 GeV. Here, the fraction of "unitarity violating" events is high at 80%. This is due to two effects. First, the scale Λ which the analysis constrains (see Figs. 6.4 and 6.5), and hence the unitarity limit, is lower. In addition, the invariant mass distribution is pushed to higher values of $m_{\chi\chi}$ due to the higher threshold.

We thus conclude that the effective theory can be valid for DM masses below a few hundred GeV, where the limit on Λ is still flat. This conclusion is in qualitative agreement with previous analyses [20, 193] which used arguments of perturbativity rather than unitarity. We emphasize that, as we shall see in the next subsection, the cross section can deviate from that derived via effective theory if the mediator is light, within the reach of the analysis. As the mass of the DM becomes heavy enough so that its production is kinematically suppressed by parton distribution functions (PDFs), the effective theory description breaks down and the UV physics must be accounted for in order to get an accurate description of the limits. In the next subsection we will consider a simplified model which includes the mediating particles explicitly and investigate how the bounds are modified. We will also see that requiring perturbative simplified models gives qualitatively similar results to the requirements of unitarity.

6.4.2 Light Mediators

We now replace the effective theory analyzed above for a renormalizable "simplified" model. Consider a neutral vector particle of mass M which couples to DM pairs with a coupling of g_χ and to up-quarks with a coupling of g_q. At low energies, say those relevant for direct detection, this model is described well by an effective theory with a vector operator suppressed by the scale $\Lambda \equiv M/\sqrt{g_\chi g_q}$.

If the mediator is sufficiently light, but still heavier than $2m_\chi$ the mediator may be produced on-shell, and subsequently decay to a pair of Dm particles. This leads to an enhanced production rate proportional to $g_q^2 g_\chi^2/(M\Gamma)$ where Γ is the total width of the mediator particle. If the mediator is much lighter than twice the DM mass, the DM production is proportional to $g_q^2 g_\chi^2/m_{\bar{\chi}\chi}$ and is significantly suppressed.

The presence of a light mediator can also affect the kinematic distribution of the signal. In particular, in the case of on-shell production of a mediator which decays to DM, one would expect the signal to be quite similar to the background of on-shell production of a Z which decays invisibly. Indeed, in Fig. 6.9 we show the distribution of M_R and R^2 for a mediator masses of 100 GeV and 300 GeV, and a DM mass of 50 GeV. One can see that the congregation of events around $R^2 \sim 1$ is absent and the distribution is similar to that of the $Z+$ jets background (see Fig. 6.1(a)). As a result, the cut efficiency for this case will be lower, which will partially counter the gain in overall rate when calculating the ultimate bounds.

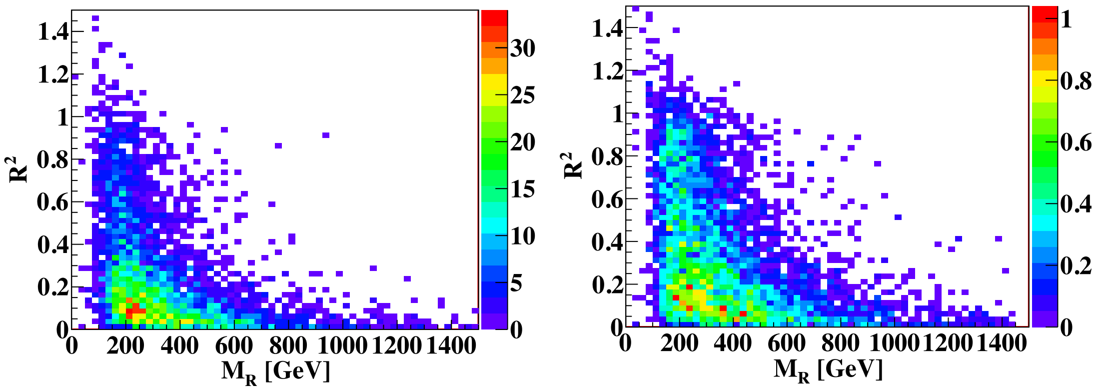

FIG. 6.9: R^2 vs. M_R for light mediators, with arbitrary normalization. The LH plot corresponds to the case of $m_\chi = 50$ GeV, $M_{Z'} = 100$ GeV, $\Gamma_{Z'} = M_{Z'}/3$ and the RH plot to $m_\chi = 50$ GeV, $M_{Z'} = 300$ GeV, $\Gamma_{Z'} = M_{Z'}/3$.

In Fig. 6.10, we show the limits we achieve on $\Lambda \equiv M/\sqrt{g_q g_\chi}$ as a function of the mediator mass M for two fixed DM masses, 50 and 500 GeV. For each case, we consider a range of widths for the mediator between $M/3$ and $M/8\pi$. We consider these two values as extremes of what is possible in general, although the narrow width may not be physically realizable for the DM couplings we consider here. We see that as the mediator mass is lowered the bound improves because DM production proceeds through the production of an on-shell mediator which later decays. The improvement can be substantial, as much as a factor of 5 in the limit on the cross section in the narrow mediator case. As the mediator mass is lowered further and its mass drops below threshold for DM production the limit weakens significantly, as expected.

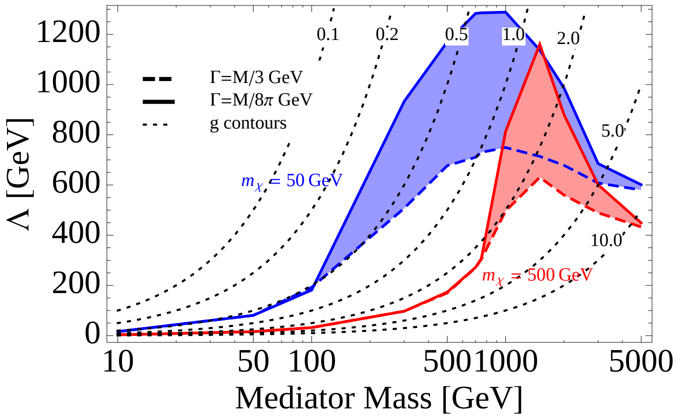

FIG. 6.10: Cutoff scale $\Lambda \equiv M/g$ bounds as a function of mediator mass M, where $g \equiv \sqrt{g_\chi g_q}$. We assume s-channel vector-type interactions and consider DM masses of $m_\chi = 50$ GeV (blue) and $m_\chi = 500$ GeV (red). We vary the width Γ of the mediator between $M/3$ (solid line) and $M/8\pi$ (dashed line).

We conclude that while it is easy for physics beyond the DM effective theory to modify the bounds derived within the effective theory, this modification can either cause bounds to improve in the intermediate mediator mass region or to weaken in the light mediator region.

6.5 Discussion and Future Prospects

In this chapter, we expand on previous work done on DM limits at colliders using monojets by utilizing the razor analysis of CMS. At the LHC, one expects events that contain several high p_T jets, and the monojet requirement may restrict the signal efficiency. By allowing for an arbitrary number of hard jets, we can improve upon the signal efficiency. Furthermore, the razor analysis uses a complementary data set to that of the monojet search, thus allowing one to combine the bounds from the two methods.

Using only the $\sim$ 800 pb^{-1} of data analyzed by CMS for their razor analysis we find that the razor bounds are slightly better than those of the monojet search, which uses $\sim$ 1 fb^{-1} (by about 40% in the direct detection cross-section). The combined limit from the razor and monojet searches is a few percent stronger than the razor bound alone. Since the uncertainties of the razor analysis are dominantly statistical in nature we expect this bound to improve with further updates of the razor analysis employing larger data sets.

We also address the validity of using an effective theory. We find that for light DM masses (below a few hundred GeV), the bound derived using an effective theory is accurate to about 10%. However, the effective theory breaks down at DM masses that are heavy enough such that the DM production is kinematically suppressed by PDFs, and we must take into account the UV physics.

Although originally conceived of as a search tool for squarks/gluinos in supersymmetry we have demonstrated that razor analysis is a powerful technique to also look for production of non-colored states that lead to missing energy in the detector. The ease with which it discriminates between signal and background makes us optimistic for future, dedicated analyses, to search for DM that use this technique. Furthermore, should an excess be observed, the existence of additional observables beyond those available in monojet/monophoton searches may prove beneficial in its interpretation.

APPENDIX A

Mass Mixing Example

In Sec. 2.2, we presented a diagrammatic representation of the mixing that takes the χ states to standard model leptons. Here we study the numerical diagonalization of the corresponding fermion mass matrices, to demonstrate that mixing angles of the size assumed in our analysis are easily obtained. To simplify the discussion, we focus on mixing with standard model leptons of a single generation, which we denote by e and ν. We include (1) Dirac masses for the χ fields:

$$\mathcal{L} \supset \sum_i \Big[a_i \, \overline{\chi}_L^{(i)} \langle H_D \rangle \chi_{uR}^{(i)} + b_i \, \overline{\chi}_L^{(i)} \langle H_D \rangle \chi_{dR}^{(i)} + c_i \, \overline{\chi}_L^{(i)} \langle \widetilde{H}_D \rangle \chi_{uR}^{(i)} + d_i \, \overline{\chi}_L^{(i)} \langle \widetilde{H}_D \rangle \chi_{dR}^{(i)} \Big] + h.c. \; , \tag{A.1}$$

where $\widetilde{H}_D \equiv i\sigma^2 H_D^*$. These terms generate a completely general two-by-two Dirac mass matrix for the χ fermions. (2) Mixing between the χ fields and standard model leptons:

$$\begin{aligned} \mathcal{L} \;\; \supset & \;\; g_1 \langle \eta \rangle \overline{\chi}_{dR}^{(1)} e_R^c + g_2 \langle \eta \rangle \overline{\chi}_{uR}^{(1)} e_R^c + \lambda_e \overline{L} \langle H \rangle e_R \\ + & \;\; g_3 \langle \eta \rangle \overline{\chi}_{dR}^{(2)} \nu_R^c + g_4 \langle \eta \rangle \overline{\chi}_{uR}^{(2)} \nu_R^c + \lambda_\nu \overline{L} \langle \tilde{H} \rangle \nu_R + h.c. \end{aligned} \tag{A.2}$$

(3) Mixing involving the vector-like leptons E_L and E_R:

$$\mathcal{L} \supset g_5 \langle\eta\rangle\, \overline{\chi}^{(3)}_{dR} E_L + g_6 \langle\eta\rangle\, \overline{\chi}^{(3)}_{uR} E_L + M_E\, \overline{E}_L E_R + g_7\, \overline{L}\langle H\rangle E_R + h.c. \tag{A.3}$$

We now write down the mass matrices which follow from Eqs. (A.1,A.2,A.3). For the neutral states, we work in the basis $f^0_L = (\chi^{(2)}_{uL}, \chi^{(2)}_{dL}, \nu^c_R)$ and $f^0_R = (\chi^{(2)}_{uR}, \chi^{(2)}_{dR}, \nu^c_L)$. The neutral mass terms can be written as $\overline{f^0_L} M_0 f^0_R + h.c.$, where

$$M_0 = \frac{1}{\sqrt{2}} \begin{pmatrix} c_2 v_D & d_2 v_D & 0 \\ a_2 v_D & b_2 v_D & 0 \\ g_4 v_\eta & g_3 v_\eta & \sqrt{2} m_\nu \end{pmatrix} , \tag{A.4}$$

assuming, for simplicity, that the vevs and couplings are real. Similarly, the mass terms for the charged states may be written $\overline{f^-_L} M_c f^-_R + h.c.$, where we assume the basis $f^-_L = (\chi^{(1)c}_{uR}, \chi^{(1)c}_{dR}, \chi^{(3)}_{uL}, \chi^{(3)}_{dL}, E_L, e_L)$ and $f^-_R = (\chi^{(1)c}_{uL}, \chi^{(1)c}_{dL}, \chi^{(3)}_{uR}, \chi^{(3)}_{dR}, E_R, e_R)$. In this case,

$$M_c = \frac{1}{\sqrt{2}} \begin{pmatrix} c_1 v_D & a_1 v_D & 0 & 0 & 0 & g_2 v_\eta \\ d_1 v_D & b_1 v_D & 0 & 0 & 0 & g_1 v_\eta \\ 0 & 0 & c_3 v_D & d_3 v_D & 0 & 0 \\ 0 & 0 & a_3 v_D & b_3 v_D & 0 & 0 \\ 0 & 0 & g_6 v_\eta & g_5 v_\eta & \sqrt{2} M_E & 0 \\ 0 & 0 & 0 & 0 & g_7 v & \sqrt{2} m_e \end{pmatrix} . \tag{A.5}$$

Given a choice of parameters, it is now a simple matter to compute the relevant mixing angles numerically. As an example, let us work in units of the dark scale v_D, which we will assume is 4 TeV. In addition we take $v_\eta = v_D$, $M_E = 1.5\, v_D$ and set the standard model lepton masses to zero (the conclusions do not change if we require realistic standard model lepton masses). If one assumes that only the following parameters are nonzero:

$$\{b_1, c_1, b_2, c_2, b_3, c_3, g_1, g_2, g_3, g_4, g_5, g_6, g_7\} = \\ \{1.9, 1.8, 1.8, 1.7, 2.1, 2.0, 0.02, 0.02, 0.02, 0.02, 0.7, 0.6, 1.0\} \ , \tag{A.6}$$

then one finds

$$\begin{aligned} \chi_{uL}^{(1)} &= 0.011\, e_{R0}^c + \cdots & \chi_{dL}^{(1)} &= 0.011\, e_{R0}^c + \cdots \\ \chi_{uL}^{(2)} &= 0.012\, \nu_{R0}^c + \cdots & \chi_{dL}^{(2)} &= 0.011\, \nu_{R0}^c + \cdots \\ \chi_{uL}^{(3)} &= 0.009\, e_{L0} + \cdots & \chi_{dL}^{(3)} &= 0.010\, e_{L0} + \cdots \end{aligned}$$

where the fields on the right represent mass eigenstates. In addition, the non-zero mass eigenvalues are all larger than the ψ mass if $m_\psi < 1.2\, v_D$, so that only decays to standard model leptons via the instanton vertex are kinematically allowed. Given the number of free parameters involved, one sees that the mixing angles are highly model dependent and can be easily set to the values assumed in Sec. 2.2.

APPENDIX B

The Parameters $\xi_\pm$

The parameters $\xi_\pm$ may be expressed in terms of the operator coefficients c_i and c_i' defined in Eq. (4.1),

$$\xi_\pm = 48\,\frac{\mathbf{c}^\dagger N_\pm\,\mathbf{c} + \mathbf{c}'^\dagger N_\pm\,\mathbf{c}'}{\mathbf{c}^\dagger D\,\mathbf{c} + \mathbf{c}'^\dagger D\,\mathbf{c}'}\,, \tag{B.1}$$

where $\mathbf{c} = [c_1, c_2, c_3, c_4, c_5]^T$ and $\mathbf{c}' = [c_1', c_2', c_3', c_4', c_5']^T$. The five-by-five matrices $N_\pm$ and D are given by

$$N_\pm = \begin{pmatrix} 1 & 0 & \mp 2 & 0 & 0 \\ 0 & 6 & 0 & \pm 2 & 0 \\ \mp 2 & 0 & 40 & 0 & \mp 2 \\ 0 & \pm 2 & 0 & 6 & 0 \\ 0 & 0 & \mp 2 & 0 & 1 \end{pmatrix} \quad \text{and} \quad D = \begin{pmatrix} 1 & 0 & 0 & 0 & 0 \\ 0 & 4 & 0 & 0 & 0 \\ 0 & 0 & 24 & 0 & 0 \\ 0 & 0 & 0 & 4 & 0 \\ 0 & 0 & 0 & 0 & 1 \end{pmatrix}\,. \tag{B.2}$$

APPENDIX C

Breaking Terms

In this appendix, we discuss a possible source of the terms in V_{soft} that break the $\mathbb{Z}_2$ symmetry of the superpotential. Generally, one can imagine such breaking terms arising from the F-term of some hidden sector superfield receiving a vacuum expectation value. To be more specific, we consider a possible scenario that results in such breaking terms and also explains the smallness of κ_q and κ_ℓ. In this scenario there is a hidden sector, which contains the six fields $\widehat{X}_{01}$, $\widehat{X}_{02}$, $\widehat{X}_{q1}$, $\widehat{X}_{q2}$, $\widehat{X}_{\ell 1}$ and

TABLE C.1: Transformation rule for the $\mathbb{Z}_{3q} \times \mathbb{Z}_{3\ell}$ symmetry. Each field transforms as $\phi \to X\phi$, where X is the corresponding factor shown in the table. For each case, $\omega^3 = 1$. Other fields not shown in the table are neutral under $\mathbb{Z}_{3q} \times \mathbb{Z}_{3\ell}$.

Field	$\mathbb{Z}_{3q}$	$\mathbb{Z}_{3\ell}$	Field	$\mathbb{Z}_{3q}$	$\mathbb{Z}_{3\ell}$
$\widehat{H}_u$	ω	1	$\widehat{X}_{01}$	1	1
$\widehat{H}_d$	ω	1	$\widehat{X}_{02}$	ω^2	ω^2
$\widehat{H}_0$	1	ω	$\widehat{X}_{q1}$	ω	1
$\widehat{H}_\ell$	1	ω	$\widehat{X}_{q2}$	ω^2	1
$\widehat{E}$	1	ω^2	$\widehat{X}_{\ell 1}$	1	ω
$\widehat{Q}$	ω^2	1	$\widehat{X}_{\ell 2}$	1	ω^2

$\widehat{X}_{\ell 2}$. The F-terms of the fields receive vevs

$$\langle F_{X_i} \rangle \sim \mathcal{O}(10^{11}\text{GeV})^2, \tag{C.1}$$

so that

$$M_{\text{SUSY}} \sim \frac{\langle F_{X_i} \rangle}{M_P} \tag{C.2}$$

is at the TeV scale. The index i denotes 01, 02, $q1$, $q2$, $\ell 1$, and $\ell 2$. A $\mathbb{Z}_{3q} \times \mathbb{Z}_{3\ell}$ symmetry is imposed, under which the fields transform according to Table C.1. The hidden sector fields $\widehat{X}_i$ couple to visible sector fields in a high energy, fundamental theory, and are Planck suppressed in the low energy effective theory. Consequentially, the lagrangian contains terms such as

$$\Delta\mathcal{L} = \frac{f'}{M_P^2} \int d^4\theta \widehat{X}_{01}^{\dagger} \widehat{X}_{02} \widehat{H}_u \widehat{H}_\ell + \frac{m'}{M_P} \int d^2\theta \widehat{X}_{02} \widehat{S} \widehat{H}_u \widehat{H}_\ell + \text{h.c.}, \tag{C.3}$$

where $d^2\theta = d(\theta\theta)$ and $d^4\theta = d(\theta\theta)d(\bar{\theta}\bar{\theta})$ represent integration over Grassmann variables and f' and m' are coupling constants. When the F-terms of $\widehat{X}_{01}$ and $\widehat{X}_{02}$ receive vevs, the terms in Eq. (C.3) give rise to

$$\begin{aligned} \Delta\mathcal{L} &= \frac{f'\langle F_{01}\rangle\langle F_{02}\rangle}{M_P^2} \int d^4\theta (\bar{\theta}\bar{\theta})(\theta\theta) \widehat{H}_u \widehat{H}_\ell + \frac{m'\langle F_{02}\rangle}{M_P} \int d^2\theta (\theta\theta) \widehat{S} \widehat{H}_u \widehat{H}_\ell + \text{h.c.} \\ &= \frac{f'\langle F_{01}\rangle\langle F_{02}\rangle}{M_P^2} H_u H_\ell + \frac{m'\langle F_{02}\rangle}{M_P} S H_u H_\ell + \text{h.c.} \\ &\to \mu_3^2 H_u H_\ell + \mu_c S H_u H_\ell + \text{h.c.}. \end{aligned} \tag{C.4}$$

TABLE C.2: A complete list of superpotential and V_{soft} terms generated by the X_i in this example.

$\frac{a'}{M_P}\int d^4\theta \widehat{X}_{q2}^{\dagger}\widehat{H}_u\widehat{H}_d + \text{h.c.}$	$\int d^2\theta \mu_q \widehat{H}_u\widehat{H}_d + \text{h.c.}$
$\frac{b'}{M_P}\int d^4\theta \widehat{X}_{\ell 2}^{\dagger}\widehat{H}_0\widehat{H}_l + \text{h.c.}$	$\int d^2\theta \mu_\ell \widehat{H}_0\widehat{H}_\ell + \text{h.c.}$
$\frac{c'}{M_P}\int d^4\theta \widehat{X}_{01}^{\dagger}\widehat{S}^2 + \text{h.c.}$	$\int d^2\theta \lambda_2 \widehat{S}^2 + \text{h.c.}$
$\frac{1}{M_P^2}\int d^4\theta \left(d'\widehat{X}_{01}^{\dagger}\widehat{X}_{q1} + d''\widehat{X}_{q2}^{\dagger}\widehat{X}_{01} + d'''\widehat{X}_{02}^{\dagger}\widehat{X}_{\ell 2} + d''''\widehat{X}_{q1}^{\dagger}\widehat{X}_{q2}\right)\widehat{H}_u\widehat{H}_d + \text{h.c.}$	$\mu_1^2 H_u H_d + \text{h.c.}$
$\frac{1}{M_P^2}\int d^4\theta \left(e'\widehat{X}_{01}^{\dagger}\widehat{X}_{\ell 1} + e''\widehat{X}_{\ell 2}^{\dagger}\widehat{X}_{01} + e'''\widehat{X}_{02}^{\dagger}\widehat{X}_{q2} + e''''\widehat{X}_{\ell 1}^{\dagger}\widehat{X}_{\ell 2}\right)\widehat{H}_0\widehat{H}_\ell + \text{h.c.}$	$\mu_2^2 H_0 H_\ell + \text{h.c.}$
$\frac{1}{M_P^2}\int d^4\theta \left(f'\widehat{X}_{01}^{\dagger}\widehat{X}_{02} + f''\widehat{X}_{q1}^{\dagger}\widehat{X}_{\ell 2} + f'''\widehat{X}_{\ell 1}^{\dagger}\widehat{X}_{q2}\right)\widehat{H}_u\widehat{H}_\ell + \text{h.c.}$	$\mu_3^2 H_u H_\ell + \text{h.c.}$
$\frac{1}{M_P^2}\int d^4\theta \left(g'\widehat{X}_{01}^{\dagger}\widehat{X}_{02} + g''\widehat{X}_{q1}^{\dagger}\widehat{X}_{\ell 2} + g'''\widehat{X}_{\ell 1}^{\dagger}\widehat{X}_{q2}\right)\widehat{H}_0\widehat{H}_d + \text{h.c.}$	$\mu_4^2 H_0 H_d + \text{h.c.}$
$\frac{1}{M_P^2}\int d^4\theta \left(h'\widehat{X}_{02}^{\dagger}\widehat{X}_{\ell 1} + h''\widehat{X}_{q1}^{\dagger}\widehat{X}_{02} + h'''\widehat{X}_{q2}^{\dagger}\widehat{X}_{\ell 2} + h''''\widehat{X}_{\ell 1}^{\dagger}\widehat{X}_{q1}\right)\widehat{H}_u^{\dagger}\widehat{H}_0 + \text{h.c.}$	$m_{u0}^2 H_u^{\dagger} H_0 + \text{h.c.}$
$\frac{1}{M_P^2}\int d^4\theta \left(i'\widehat{X}_{02}^{\dagger}\widehat{X}_{\ell 1} + i''\widehat{X}_{q1}^{\dagger}\widehat{X}_{02} + i'''\widehat{X}_{q2}^{\dagger}\widehat{X}_{\ell 2} + i''''\widehat{X}_{\ell 1}^{\dagger}\widehat{X}_{q1}\right)\widehat{H}_d^{\dagger}\widehat{H}_\ell + \text{h.c.}$	$m_{d\ell}^2 H_d^{\dagger} H_\ell + \text{h.c.}$
$\frac{1}{M_P^2}\int d^4\theta \sum_i j^i \widehat{X}_i^{\dagger}\widehat{X}_i\widehat{H}_f^{\dagger}\widehat{H}_f + \text{h.c.}$	$m_f^2 \lvert H_f \rvert^2 + \text{h.c.}$
$\frac{k'}{M_P}\int d^2\theta \widehat{X}_{q1}\widehat{S}\widehat{H}_u\widehat{H}_d + \text{h.c.}$	$\mu_a S H_u H_d + \text{h.c.}$
$\frac{l'}{M_P}\int d^2\theta \widehat{X}_{\ell 1}\widehat{S}\widehat{H}_0\widehat{H}_\ell + \text{h.c.}$	$\mu_b S H_0 H_\ell + \text{h.c.}$
$\frac{m'}{M_P}\int d^2\theta \widehat{X}_{02}\widehat{S}\widehat{H}_u\widehat{H}_\ell + \text{h.c.}$	$\mu_c S H_u H_\ell + \text{h.c.}$
$\frac{n'}{M_P}\int d^2\theta \widehat{X}_{02}\widehat{S}\widehat{H}_0\widehat{H}_d + \text{h.c.}$	$\mu_d S H_0 H_d + \text{h.c.}$
$\frac{1}{M_P^2}\int d^4\theta \sum_i o^i \widehat{X}_i^{\dagger}\widehat{X}_i\widehat{S}^2 + \text{h.c.}$	$b_s^2 S^2 + \text{h.c.}$
$\frac{p'}{M_P}\int d^2\theta \widehat{X}_0\widehat{S}^3 + \text{h.c.}$	$a_s S^3 + \text{h.c.}$

Similarly, the breaking parameters μ_4^2 and μ_d arise from the Planck suppressed terms

$$\begin{aligned}\Delta\mathcal{L} &= \frac{g'}{M_P^2}\int d^4\theta \widehat{X}_{01}^\dagger \widehat{X}_{02}\widehat{H}_0\widehat{H}_d + \frac{n'}{M_P}\int d^2\theta \widehat{X}_{02}\widehat{S}\widehat{H}_0\widehat{H}_d + \text{h.c.}\\ &\to \frac{g'\langle F_{01}\rangle\langle F_{02}\rangle}{M_P^2}H_0H_d + \frac{n'\langle F_{02}\rangle}{M_P}SH_0H_d + \text{h.c.}\\ &\to \mu_4^2 H_0H_d + \mu_d SH_0H_d + \text{h.c.},\end{aligned} \tag{C.5}$$

while the parameters m_{u0}^2 and $m_{d\ell}^2$ arise from

$$\begin{aligned}\Delta\mathcal{L} &= \frac{h'}{M_P^2}\int d^4\theta \widehat{X}_{02}^\dagger \widehat{X}_{\ell 1}\widehat{H}_u^\dagger\widehat{H}_0 + \frac{i'}{M_P^2}\int d^4\theta \widehat{X}_{02}^\dagger \widehat{X}_{\ell 1}\widehat{H}_d^\dagger\widehat{H}_\ell + \text{h.c.}\\ &\to \frac{h'\langle F_{02}\rangle\langle F_{\ell 1}\rangle}{M_P^2}H_u^\dagger H_0 + \frac{i'\langle F_{02}\rangle\langle F_{\ell 1}\rangle}{M_P^2}H_d^\dagger H_\ell + \text{h.c.}\\ &\to m_{u0}^2 H_u^\dagger H_0 + m_{d\ell}^2 H_d^\dagger H_\ell + \text{h.c.}.\end{aligned} \tag{C.6}$$

In this way, all of the $\mathbb{Z}_2$ breaking terms are generated. At this point it should be noted that the $\mathbb{Z}_{3q}\times\mathbb{Z}_{3\ell}$ symmetry actually prohibits the terms $\mu_q\hat{H}_u\hat{H}_d$, $\mu_\ell\hat{H}_0\hat{H}_\ell$, $\kappa_q\hat{S}\hat{H}_u\hat{H}_d$, and $\kappa_\ell\hat{S}\hat{H}_0\hat{H}_\ell$ from appearing in the superpotential [see Eq. (5.1)]. As far as the μ_q and μ_ℓ terms are concerned, this is not a problem since they are generated by the vevs of the $\widehat{X}_{q2}$ and $\widehat{X}_{\ell 2}$ fields in the same manner:

$$\begin{aligned}\Delta\mathcal{L} &= \frac{a'}{M_P}\int d^4\theta \widehat{X}_{q2}^\dagger \widehat{H}_u\widehat{H}_d + \frac{b'}{M_P}\int d^4\theta \widehat{X}_{\ell 2}^\dagger \widehat{H}_0\widehat{H}_\ell\\ &\to \frac{a'\langle F_{q2}\rangle}{M_P}\int d^2\theta d^2\bar{\theta}\,(\bar{\theta}\bar{\theta})\widehat{H}_u\widehat{H}_d + \frac{b'\langle F_{\ell 2}\rangle}{M_P}\int d^2\theta d^2\bar{\theta}\,(\bar{\theta}\bar{\theta})\widehat{H}_0\widehat{H}_\ell\\ &= \frac{a'\langle F_{q2}\rangle}{M_P}\int d^2\theta \widehat{H}_u\widehat{H}_d + \frac{b'\langle F_{\ell 2}\rangle}{M_P}\int d^2\theta \widehat{H}_0\widehat{H}_\ell\\ &\to \mu_q\int d^2\theta \widehat{H}_u\widehat{H}_d + \mu_\ell\int d^2\theta \widehat{H}_0\widehat{H}_\ell.\end{aligned} \tag{C.7}$$

In this UV completion scenario, the terms corresponding to κ_q, κ_ℓ, λ_1 and t are not generated in this way. Because of the $\mathbb{Z}_{3q}\times\mathbb{Z}_{3\ell}$ symmetry, they are entirely absent at tree level. Benchmark points II and V in Table D.1 satisfy $\kappa_q = \kappa_\ell = \lambda_1 = t = 0$

and yield results consistent with our goals. Since we are not committing to this particular UV completion scheme, we consider several other benchmark points that include nonzero values for these parameters. A list of the soft breaking terms relevant to this paper, which are generated by the fields X_i, is given in Table C.2.

APPENDIX D

List of Benchmark Points

In this Appendix, we show several benchmark points given in Table D.1. Benchmarks point I-III lie in the suggested CoGeNT and DAMA range, while benchmarks point IV-V satisfy CDMS bound. Benchmark point I is identical with benchmark point A discussed in the text. Benchmark point IV is identical with benchmark point B. Benchmark points II and V are motivated by mechanism described in Appendix C.

TABLE D.1: Additional benchmark points

Benchmark point	I	II	III	IV	V
κ_q	0.01	0	0.01	0.01	0
κ_l	0.01	0	0.01	0.01	0
κ_s	0.6	0.6	0.5	0.6	0.6
$\tan\alpha$	20	15	30	20	30
$\tan\beta$	50	30	30	50	25
$\tan\beta_\ell$	10	10	5	10	5
v_s (GeV)	50	50	100	50	50
v_u (GeV)	245.6	245.3	245.7	245.6	245.7
v_d (GeV)	4.9	8.2	8.2	4.9	9.8
v_0 (GeV)	12.2	16.2	8.0	12.2	8.0
v_ℓ (GeV)	1.2	1.6	1.6	1.2	1.6
μ_q (GeV)	125	125	200	125	125
μ_ℓ (GeV)	125	125	150	125	150
λ_1^2 (GeV^2)	100^2	0	150^2	100^2	0
λ_2 (GeV)	-35	-35	-63	-35	-35
M_1 (GeV)	500	500	250	500	250
M_2 (GeV)	500	500	500	500	500
m_{u0}^2 (GeV^2)	-100^2	-150^2	-150^2	-100^2	-150^2
$m_{d\ell}^2$ (GeV^2)	100^2	200^2	100^2	100^2	200^2
μ_1^2 (GeV^2)	400^2	300^2	300^2	400^2	400^2
μ_2^2 (GeV^2)	200^2	300^2	250^2	200^2	200^2
μ_3^2 (GeV^2)	200^2	200^2	250^2	200^2	250^2
μ_4^2 (GeV^2)	400^2	200^2	200^2	400^2	400^2
μ_a (GeV)	100	75	75	100	100
μ_b (GeV)	200	150	300	200	250
μ_c (GeV)	200	200	400	200	300
μ_d (GeV)	200	100	100	200	250

Continued on the next page

Benchmark point	I	II	III	IV	V
t^3 (GeV^3)	60.6^3	0	83.9^3	55.0^3	0
b_s^2 (GeV^2)	63.4^2	43.6^2	98.2^2	66.3^2	47.1^2
a_s (GeV)	-42.4	-21.7	-50.2	-42.2	-20.0
m_{χ_1} (GeV)	7.4	7.4	7.7	7.4	7.4
$m_{\chi_1^\pm}$ (GeV)	118	117	151	118	117
m_{h_1} (GeV)	11.3	19.2	12.8	41.5	41.4
m_{a_1} (GeV)	18.7	16.1	18.8	19.3	19.2
$\langle\sigma v\rangle$ ($\frac{\text{cm}^3}{\text{s}}$)	4.0×10^{-26}	3.4×10^{-26}	4.6×10^{-26}	3.0×10^{-26}	3.1×10^{-26}
$\frac{\langle\sigma v\ (\chi_1\chi_1 \to \text{hadrons})\rangle}{\langle\sigma v\rangle}$	23%	38%	32%	23%	24%
σ_{SI}(cm^2)	1.7×10^{-40}	1.2×10^{-40}	1.5×10^{-40}	1.2×10^{-42}	6.1×10^{-42}
$\Gamma_{Z\to\chi_1\chi_1}$ (GeV)	1.4×10^{-9}	0	2.1×10^{-10}	1.4×10^{-9}	0
$\Gamma_{Z\to h_1 a_1}$ (GeV)	1.1×10^{-11}	1.2×10^{-10}	1.4×10^{-10}	4.9×10^{-12}	4.2×10^{-11}
k	8.0×10^{-3}	3.5×10^{-2}	2.2×10^{-2}	1.3×10^{-2}	0.12
$S_{model}(e^+e^- \to h_1 a_1)$	1×10^{-10}	2×10^{-9}	2×10^{-9}	1×10^{-10}	1×10^{-9}
$S_{model}(e^+e^- \to h_2 a_1)$	1×10^{-12}	5×10^{-11}	3×10^{-11}	2×10^{-12}	1×10^{-10}
$\sigma_{e^+e^-\to\chi_1\chi_2}$ (pb)	1×10^{-5}	0	5×10^{-9}	1×10^{-5}	0

BIBLIOGRAPHY

[1] S. Schael et al. (ALEPH Collaboration, DELPHI Collaboration, L3 Collaboration, OPAL Collaborations, LEP Working Group for Higgs Boson Searches), Eur. Phys. J. **C47**, 547 (2006), `hep-ex/0602042`.

[2] D. Larson, J. Dunkley, G. Hinshaw, E. Komatsu, M. Nolta, et al., Astrophys. J. Suppl. **192**, 16 (2011), `1001.4635`.

[3] E. W. Kolb and M. S. Turner, *The Early Universe* (Westview Press, Boulder, Colorado, 1994).

[4] G. Angloher, M. Bauer, I. Bavykina, A. Bento, C. Bucci, et al. (2011), `1109.0702`.

[5] K. Nakamura et al. (Particle Data Group), J. Phys. **G37**, 075021 (2010).

[6] O. Adriani et al. (PAMELA Collaboration), Phys. Rev. Lett. **105**, 121101 (2010), `1007.0821`.

[7] O. Adriani et al. (PAMELA Collaboration), Nature **458**, 607 (2009), `0810.4995`.

[8] M. Ackermann et al. (Fermi LAT Collaboration), Phys. Rev. **D82**, 092004 (2010), `1008.3999`.

[9] `https://twiki.cern.ch/twiki/bin/view/CMSPublic/PhysicsResultsEXO11059Winter2012`.

[10] Z. Ahmed et al. (The CDMS-II Collaboration), Science **327**, 1619 (2010), `0912.3592`.

[11] S. Barwick et al. (HEAT Collaboration), Astrophys. J. **482**, L191 (1997), `astro-ph/9703192`.

[12] M. Aguilar et al. (AMS-01 Collaboration), Phys. Lett. **B646**, 145 (2007), `astro-ph/0703154`.

[13] M. Boezio, P. Carlson, T. Francke, N. Weber, M. Suffert, et al., Astrophys. J. **532**, 653 (2000).

[14] F. Aharonian et al. (H.E.S.S. Collaboration), Phys. Rev. Lett. **101**, 261104 (2008), `0811.3894`.

[15] S. Torii et al. (PPB-BETS Collaboration) (2008), `0809.0760`.

[16] M. DuVernois, S. Barwick, J. Beatty, A. Bhattacharyya, C. Bower, et al., Astrophys. J. **559**, 296 (2001).

[17] M. Boezio et al. (WIZARD Collaboration), Astrophys. J. **487**, 415 (1997).

[18] S. Orito et al. (BESS Collaboration), Phys. Rev. Lett. **84**, 1078 (2000), `astro-ph/9906426`.

[19] J. Mitchell, L. Barbier, E. Christian, J. Krizmanic, K. Krombel, et al., Phys. Rev. Lett. **76**, 3057 (1996).

[20] P. J. Fox, R. Harnik, J. Kopp, and Y. Tsai (2011), `1109.4398`.

[21] C. Aalseth et al. (CoGeNT collaboration), Phys. Rev. Lett. **106**, 131301 (2011), `1002.4703`.

[22] R. Bernabei et al. (DAMA Collaboration), Eur. Phys. J. **C56**, 333 (2008), `0804.2741`.

[23] E. Aprile et al. (XENON100), Phys. Rev. Lett. **107**, 131302 (2011), `1104.2549`.

[24] E. Behnke, J. Behnke, S. Brice, D. Broemmelsiek, J. Collar, et al., Phys. Rev. Lett. **106**, 021303 (2011), `1008.3518`.

[25] M. Barnabe-Heider et al. (PICASSO Collaboration), Phys. Lett. **B624**, 186 (2005), `hep-ex/0502028`.

[26] T. Girard et al. (for the SIMPLE Collaboration), PoS **IDM2010**, 055 (2011), `1101.1885`.

[27] J. Angle, E. Aprile, F. Arneodo, L. Baudis, A. Bernstein, et al., Phys. Rev. Lett. **101**, 091301 (2008), `0805.2939`.

[28] D. Hooper, J. Collar, J. Hall, D. McKinsey, and C. Kelso, Phys. Rev. **D82**, 123509 (2010), `1007.1005`.

[29] J. Kopp, T. Schwetz, and J. Zupan, JCAP **1002**, 014 (2010), `0912.4264`.

[30] V. C. Rubin and J. Ford, W.Kent, Astrophys. J. **159**, 379 (1970).

[31] A. Vikhlinin, A. Kravtsov, W. Forman, C. Jones, M. Markevitch, et al., Astrophys. J. **640**, 691 (2006), `astro-ph/0507092`.

[32] G. Jungman, M. Kamionkowski, and K. Griest, Phys. Rept. **267**, 195 (1996), `hep-ph/9506380`.

[33] G. Servant and T. M. Tait, Nucl. Phys. **B650**, 391 (2003), `hep-ph/0206071`.

[34] A. Birkedal-Hansen and J. G. Wacker, Phys. Rev. **D69**, 065022 (2004), `hep-ph/0306161`.

[35] D. E. Kaplan, M. A. Luty, and K. M. Zurek, Phys. Rev. **D79**, 115016 (2009), `0901.4117`.

[36] M. R. Buckley and L. Randall, JHEP **1109**, 009 (2011), 11 pages, 4 figures, `1009.0270`.

[37] J. Shelton and K. M. Zurek, Phys. Rev. **D82**, 123512 (2010), 20 pages, 2 figures, `1008.1997`.

[38] A. Falkowski, J. T. Ruderman, and T. Volansky, JHEP **1105**, 106 (2011), `1101.4936`.

[39] D. Hooper (2012), `1201.1303`.

[40] M. Boezio et al. (WiZard/CAPRICE Collaboration), Astrophys. J. **561**, 787 (2001), `astro-ph/0103513`.

[41] Y. Asaoka, Y. Shikaze, K. Abe, K. Anraku, M. Fujikawa, et al., Phys. Rev. Lett. **88**, 051101 (2002), `astro-ph/0109007`.

[42] K. Abe, H. Fuke, S. Haino, T. Hams, A. Itazaki, et al., Phys. Lett. **B670**, 103 (2008), `0805.1754`.

[43] M. Aguilar et al. (AMS Collaboration), Phys. Rept. **366**, 331 (2002).

[44] A. Beach, J. Beatty, A. Bhattacharyya, C. Bower, S. Coutu, et al., Phys. Rev. Lett. **87**, 271101 (2001), `astro-ph/0111094`.

[45] M. Ackermann et al. (The Fermi LAT Collaboration), Phys. Rev. Lett. **108**, 011103 (2012), `1109.0521`.

[46] J. Chang, J. Adams, H. Ahn, G. Bashindzhagyan, M. Christl, et al., Nature **456**, 362 (2008).

[47] F. Aharonian et al. (H.E.S.S. Collaboration), Astron. Astrophys. **508**, 561 (2009), `0905.0105`.

[48] S. Torii, T. Tamura, N. Tateyama, K. Yoshida, J. Nishimura, et al., Astrophys. J. **559**, 973 (2001).

[49] N. Arkani-Hamed, D. P. Finkbeiner, T. R. Slatyer, and N. Weiner, Phys. Rev. **D79**, 015014 (2009), `0810.0713`.

[50] D. Feldman, Z. Liu, and P. Nath, Phys. Rev. **D79**, 063509 (2009), `0810.5762`.

[51] A. Ibarra, D. Tran, and C. Weniger, JCAP **1001**, 009 (2010), `0906.1571`.

[52] D. Hooper, P. Blasi, and P. D. Serpico, JCAP **0901**, 025 (2009), `0810.1527`.

[53] A. Birkedal, K. Matchev, and M. Perelstein, Phys. Rev. **D70**, 077701 (2004), `hep-ph/0403004`.

[54] J. Goodman et al., Phys. Lett. **B695**, 185 (2011), `1005.1286`.

[55] Y. Bai, P. J. Fox, and R. Harnik, JHEP **12**, 048 (2010), `1005.3797`.

[56] J. Goodman et al., Phys. Rev. **D82**, 116010 (2010), `1008.1783`.

[57] A. Rajaraman, W. Shepherd, T. M. Tait, and A. M. Wijangco, Phys. Rev. **D84**, 095013 (2011), `1108.1196`.

[58] T. Aaltonen et al. (The CDF Collaboration) (2012), `1203.0742`.

[59] CMS Collaboration, Tech. Rep. CMS-PAS-EXO-11-096, CERN, Geneva (2012).

[60] P. J. Fox, R. Harnik, J. Kopp, and Y. Tsai, Phys. Rev. **D84**, 014028 (2011), `1103.0240`.

[61] J.-F. Fortin and T. M. P. Tait (2011), `1103.3289`.

[62] A. A. Abdo et al. (The Fermi LAT Collaboration), Phys. Rev. Lett. **102**, 181101 (2009), `0905.0025`.

[63] O. Adriani, G. Barbarino, G. Bazilevskaya, R. Bellotti, M. Boezio, et al., Phys. Rev. Lett. **102**, 051101 (2009), `0810.4994`.

[64] H. Yuksel, M. D. Kistler, and T. Stanev, Phys. Rev. Lett. **103**, 051101 (2009), `0810.2784`.

[65] I. Cholis, L. Goodenough, D. Hooper, M. Simet, and N. Weiner, Phys. Rev. **D80**, 123511 (2009), `0809.1683`.

[66] J. D. March-Russell and S. M. West, Phys. Lett. **B676**, 133 (2009), `0812.0559`.

[67] M. Pospelov and A. Ritz, Phys. Lett. **B671**, 391 (2009), `0810.1502`.

[68] M. Ibe, H. Murayama, and T. Yanagida, Phys. Rev. **D79**, 095009 (2009), `0812.0072`.

[69] W.-L. Guo and Y.-L. Wu, Phys. Rev. **D79**, 055012 (2009), `0901.1450`.

[70] W.-L. Guo, Y.-L. Wu, and Y.-F. Zhou, Phys. Rev. **D81**, 075014 (2010), `1001.0307`.

[71] M. Luo, L. Wang, W. Wu, and G. Zhu, Phys. Lett. **B688**, 216 (2010), `0911.3235`.

[72] B. Kyae, Phys. Lett. **B685**, 19 (2010), `0909.3139`.

[73] J.-H. Huh and J. E. Kim, Phys. Rev. **D80**, 075012 (2009), `0908.0152`.

[74] M. R. Buckley, K. Freese, D. Hooper, D. Spolyar, and H. Murayama, Phys. Rev. **D81**, 016006 (2010), `0907.2385`.

[75] D. Aristizabal Sierra, D. Restrepo, and O. Zapata, Phys. Rev. **D80**, 055010 (2009), `0907.0682`.

[76] C.-H. Chen, C.-Q. Geng, and D. V. Zhuridov, JCAP **0910**, 001 (2009), `0906.1646`.

[77] A. Arvanitaki, S. Dimopoulos, S. Dubovsky, P. W. Graham, R. Harnik, et al., Phys. Rev. **D80**, 055011 (2009), `0904.2789`.

[78] S.-L. Chen, R. N. Mohapatra, S. Nussinov, and Y. Zhang, Phys. Lett. **B677**, 311 (2009), `0903.2562`.

[79] K. Ishiwata, S. Matsumoto, and T. Moroi, JHEP **0905**, 110 (2009), `0903.0242`.

[80] S. Shirai, F. Takahashi, and T. Yanagida, Phys. Lett. **B675**, 73 (2009), `0902.4770`.

[81] X. Chen, JCAP **0909**, 029 (2009), `0902.0008`.

[82] C.-H. Chen, C.-Q. Geng, and D. V. Zhuridov, Phys. Lett. **B675**, 77 (2009), `0901.2681`.

[83] K. Hamaguchi, F. Takahashi, and T. Yanagida, Phys. Lett. **B677**, 59 (2009), `0901.2168`.

[84] E. Nardi, F. Sannino, and A. Strumia, JCAP **0901**, 043 (2009), `0811.4153`.

[85] C.-R. Chen, M. M. Nojiri, F. Takahashi, and T. Yanagida, Prog. Theor. Phys. **122**, 553 (2009), `0811.3357`.

[86] K. Hamaguchi, E. Nakamura, S. Shirai, and T. Yanagida, Phys. Lett. **B674**, 299 (2009), `0811.0737`.

[87] P.-f. Yin, Q. Yuan, J. Liu, J. Zhang, X.-j. Bi, et al., Phys. Rev. **D79**, 023512 (2009), `0811.0176`.

[88] C.-R. Chen, F. Takahashi, and T. Yanagida, Phys. Lett. **B671**, 71 (2009), `0809.0792`.

[89] I. Gogoladze, R. Khalid, Q. Shafi, and H. Yuksel, Phys. Rev. **D79**, 055019 (2009), `0901.0923`.

[90] A. Ibarra and D. Tran, JCAP **0902**, 021 (2009), `0811.1555`.

[91] V. Kuzmin and V. Rubakov, Phys. Atom. Nucl. **61**, 1028 (1998), `astro-ph/9709187`.

[92] H. Fukuoka, J. Kubo, and D. Suematsu, Phys. Lett. **B678**, 401 (2009), `0905.2847`.

[93] G. 't Hooft, Phys. Rev. Lett. **37**, 8 (1976).

[94] G. 't Hooft, Phys. Rev. **D14**, 3432 (1976).

[95] R. Noble, Phys. Rev. **D25**, 825 (1982).

[96] B. Patt and F. Wilczek (2006), `hep-ph/0605188`.

[97] P. Gondolo and G. Gelmini, Nucl. Phys. **B360**, 145 (1991).

[98] K. Griest and D. Seckel, Phys. Rev. **D43**, 3191 (1991).

[99] C. Munoz, Int. J. Mod. Phys. **A19**, 3093 (2004), `hep-ph/0309346`.

[100] J. R. Ellis, A. Ferstl, and K. A. Olive, Phys. Lett. **B481**, 304 (2000), `hep-ph/0001005`.

[101] D. McKinsey, D. Akerib, S. Bedikian, A. Bernstein, A. Bolozdynya, et al., J. Phys. Conf. Ser. **203**, 012026 (2010).

[102] S. Fiorucci, D. Akerib, S. Bedikian, A. Bernstein, A. Bolozdynya, et al., AIP Conf. Proc. **1200**, 977 (2010), `0912.0482`.

[103] J. Diaz-Cruz and E. Ma, Phys. Lett. **B695**, 264 (2011), `1007.2631`.

[104] H. Zhang, C. S. Li, Q.-H. Cao, and Z. Li, Phys. Rev. **D82**, 075003 (2010), `0910.2831`.

[105] F. Chen, J. M. Cline, and A. R. Frey, Phys. Rev. **D80**, 083516 (2009), `0907.4746`.

[106] M. Baumgart, C. Cheung, J. T. Ruderman, L.-T. Wang, and I. Yavin, JHEP **0904**, 014 (2009), `0901.0283`.

[107] D. G. Walker (2009), `0907.3146`.

[108] R. Essig, N. Sehgal, and L. E. Strigari, Phys. Rev. **D80**, 023506 (2009), `0902.4750`.

[109] D. Malyshev, I. Cholis, and J. Gelfand, Phys. Rev. **D80**, 063005 (2009), `0903.1310`.

[110] V. Barger, Y. Gao, W. Y. Keung, D. Marfatia, and G. Shaughnessy, Phys. Lett. **B678**, 283 (2009), `0904.2001`.

[111] P. Meade, M. Papucci, A. Strumia, and T. Volansky, Nucl. Phys. **B831**, 178 (2010), `0905.0480`.

[112] L. Zhang, J. Redondo, and G. Sigl, JCAP **0909**, 012 (2009), `0905.4952`.

[113] M. Cirelli, P. Panci, and P. D. Serpico, Nucl. Phys. **B840**, 284 (2010), `0912.0663`.

[114] L. Covi, M. Grefe, A. Ibarra, and D. Tran, JCAP **1004**, 017 (2010), `0912.3521`.

[115] L. Zhang, C. Weniger, L. Maccione, J. Redondo, and G. Sigl, JCAP **1006**, 027 (2010), `0912.4504`.

[116] G. Hutsi, A. Hektor, and M. Raidal, JCAP **1007**, 008 (2010), `1004.2036`.

[117] J. Ke, M. Luo, L. Wang, and G. Zhu, Phys. Lett. **B698**, 44 (2011), `1101.5878`.

[118] M. Garny, A. Ibarra, D. Tran, and C. Weniger, JCAP **1101**, 032 (2011), `1011.3786`.

[119] L. Dugger, T. E. Jeltema, and S. Profumo, JCAP **1012**, 015 (2010), `1009.5988`.

[120] C. D. Carone, J. Erlich, and R. Primulando, Phys. Rev. **D82**, 055028 (2010), `1008.0642`.

[121] A. Arvanitaki, S. Dimopoulos, S. Dubovsky, P. W. Graham, R. Harnik, et al., Phys. Rev. **D79**, 105022 (2009), `0812.2075`.

[122] H.-S. Goh, L. J. Hall, and P. Kumar, JHEP **0905**, 097 (2009), `0902.0814`.

[123] C.-R. Chen and F. Takahashi, JCAP **0902**, 004 (2009), `0810.4110`.

[124] Y. Nomura and J. Thaler, Phys. Rev. **D79**, 075008 (2009), `0810.5397`.

[125] K. Ishiwata, S. Matsumoto, and T. Moroi, Phys. Lett. **B675**, 446 (2009), `0811.0250`.

[126] M. Endo and T. Shindou, JHEP **0909**, 037 (2009), `0903.1813`.

[127] A. Ibarra, A. Ringwald, D. Tran, and C. Weniger, JCAP **0908**, 017 (2009), `0903.3625`.

[128] S. Shirai, F. Takahashi, and T. Yanagida, Phys. Lett. **B680**, 485 (2009), 11 pages, 4 figures, `0905.0388`.

[129] C.-H. Chen, C.-Q. Geng, and D. V. Zhuridov, Eur. Phys. J. **C67**, 479 (2010), `0905.0652`.

[130] J. Mardon, Y. Nomura, and J. Thaler, Phys. Rev. **D80**, 035013 (2009), `0905.3749`.

[131] K.-Y. Choi, D. E. Lopez-Fogliani, C. Munoz, and R. R. de Austri, JCAP **1003**, 028 (2010), `0906.3681`.

[132] X. Gao, Z. Kang, and T. Li, Eur. Phys. J. **C69**, 467 (2010), `1001.3278`.

[133] S. Matsumoto and K. Yoshioka, Phys. Rev. **D82**, 053009 (2010), `1006.1688`.

[134] K.-Y. Choi, D. Restrepo, C. E. Yaguna, and O. Zapata, JCAP **1010**, 033 (2010), `1007.1728`.

[135] K. Ishiwata, S. Matsumoto, and T. Moroi, JHEP **1012**, 006 (2010), `1008.3636`.

[136] K. Hamaguchi, S. Shirai, and T. Yanagida, Phys. Lett. **B673**, 247 (2009), `0812.2374`.

[137] B. Kyae, JCAP **0907**, 028 (2009), `0902.0071`.

[138] P. H. Frampton and P. Q. Hung, Phys. Lett. **B675**, 411 (2009), `0903.0358`.

[139] M. Kadastik, K. Kannike, and M. Raidal, Phys. Rev. **D81**, 015002 (2010), `0903.2475`.

[140] M. Kadastik, K. Kannike, and M. Raidal, Phys. Rev. **D80**, 085020 (2009), `0907.1894`.

[141] Q.-H. Cao, E. Ma, and G. Shaughnessy, Phys. Lett. **B673**, 152 (2009), `0901.1334`.

[142] C. Arina, T. Hambye, A. Ibarra, and C. Weniger, JCAP **1003**, 024 (2010), `0912.4496`.

[143] J. Schmidt, C. Weniger, and T. T. Yanagida, Phys. Rev. **D82**, 103517 (2010), `1008.0398`.

[144] Y. Kajiyama and H. Okada, Nucl. Phys. **B848**, 303 (2011), `1011.5753`.

[145] N. Haba, Y. Kajiyama, S. Matsumoto, H. Okada, and K. Yoshioka, Phys. Lett. **B695**, 476 (2011), `1008.4777`.

[146] C. Froggatt and H. B. Nielsen, Nucl. Phys. **B147**, 277 (1979).

[147] T. Banks and M. Dine, Phys. Rev. **D45**, 1424 (1992), revised version, `hep-th/9109045`.

[148] T. Delahaye, R. Lineros, F. Donato, N. Fornengo, and P. Salati, Phys. Rev. **D77**, 063527 (2008), `0712.2312`.

[149] T. Sjostrand, S. Mrenna, and P. Z. Skands, Comput. Phys. Commun. **178**, 852 (2008), `0710.3820`.

[150] J. F. Navarro, C. S. Frenk, and S. D. White, Astrophys. J. **462**, 563 (1996), `astro-ph/9508025`.

[151] A. Ibarra and D. Tran, JCAP **0807**, 002 (2008), `0804.4596`.

[152] V. Ptuskin, I. V. Moskalenko, F. Jones, A. Strong, and V. Zirakashvili, Astrophys. J. **642**, 902 (2006), `astro-ph/0510335`.

[153] J. McDonald, Phys. Rev. **D50**, 3637 (1994), `hep-ph/0702143`.

[154] M. Cirelli, M. Kadastik, M. Raidal, and A. Strumia, Nucl. Phys. **B813**, 1 (2009), `0809.2409`.

[155] Y.-Z. Fan, B. Zhang, and J. Chang, Int. J. Mod. Phys. **D19**, 2011 (2010), `1008.4646`.

[156] M. T. Frandsen, I. Masina, and F. Sannino, Phys. Rev. **D83**, 127301 (2011), `1011.0013`.

[157] S. Chang and L. Goodenough, Phys. Rev. **D84**, 023524 (2011), `1105.3976`.

[158] I. Masina and F. Sannino, JCAP **1109**, 021 (2011), `1106.3353`.

[159] J. T. Ruderman and T. Volansky (2009), `0907.4373`.

[160] A. Falkowski, J. Juknevich, and J. Shelton (2009), `0908.1790`.

[161] A. Kounine (2010), `1009.5349`.

[162] H.-C. Cheng, W.-C. Huang, I. Low, and A. Menon, JHEP **1103**, 019 (2011), `1012.5300`.

[163] E. Commins and P. Bucksbaum (1983).

[164] R. Mertig, M. Bohm, and A. Denner, Comput. Phys. Commun. **64**, 345 (1991).

[165] T. Sjostrand, S. Mrenna, and P. Z. Skands, JHEP **0605**, 026 (2006), `hep-ph/0603175`.

[166] D. Hooper and J. Silk, Phys. Rev. **D71**, 083503 (2005), `hep-ph/0409104`.

[167] E. A. Baltz and J. Edsjo, Phys. Rev. **D59**, 023511 (1998), `astro-ph/9808243`.

[168] F. Donato, N. Fornengo, D. Maurin, and P. Salati, Phys. Rev. **D69**, 063501 (2004), `astro-ph/0306207`.

[169] D. Grasso et al. (FERMI-LAT Collaboration), Astropart. Phys. **32**, 140 (2009), `0905.0636`.

[170] D. Hooper and L. Goodenough, Phys. Lett. **B697**, 412 (2011), `1010.2752`.

[171] A. Boyarsky, D. Malyshev, and O. Ruchayskiy, Phys. Lett. **B705**, 165 (2011), `1012.5839`.

[172] K. N. Abazajian, JCAP **1103**, 010 (2011), `1011.4275`.

[173] J. Kopp, V. Niro, T. Schwetz, and J. Zupan, PoS **IDM2010**, 118 (2011), `1011.1398`.

[174] C. Kelso and D. Hooper, JCAP **1102**, 002 (2011), `1011.3076`.

[175] G. Marshall and M. Sher, Phys. Rev. **D83**, 015005 (2011), `1011.3016`.

[176] H. E. Logan, Phys. Rev. **D83**, 035022 (2011), `1010.4214`.

[177] E. Aprile et al. (XENON100 Collaboration), Phys. Rev. Lett. **105**, 131302 (2010), `1005.0380`.

[178] Z. Ahmed et al. (CDMS-II Collaboration), Phys. Rev. Lett. **106**, 131302 (2011), `1011.2482`.

[179] R. Kappl, M. Ratz, and M. W. Winkler, Phys. Lett. **B695**, 169 (2011), `1010.0553`.

[180] J. Espinosa and M. Quiros, Phys. Lett. **B279**, 92 (1992).

[181] J. Espinosa and M. Quiros, Phys. Lett. **B302**, 51 (1993), `hep-ph/9212305`.

[182] G. L. Kane, C. F. Kolda, and J. D. Wells, Phys. Rev. Lett. **70**, 2686 (1993), `hep-ph/9210242`.

[183] E. Komatsu et al. (WMAP Collaboration), Astrophys. J. Suppl. **180**, 330 (2009), `0803.0547`.

[184] G. Abbiendi et al. (OPAL Collaboration), Eur. Phys. J. **C27**, 311 (2003), 36 pages, 14 figures, `hep-ex/0206022`.

[185] J. Abdallah et al. (DELPHI Collaboration), Eur. Phys. J. **C31**, 421 (2003), `hep-ex/0311019`.

[186] `http://www-cdf.fnal.gov/physics/exotic/r2a/20070322.monojet/public/ykk.html`.

[187] T. Aaltonen et al. (CDF), Phys. Rev. Lett. **101**, 181602 (2008), `0807.3132`.

[188] J. Goodman and W. Shepherd (2011), `1111.2359`.

[189] I. M. Shoemaker and L. Vecchi (2011), `1112.5457`.

[190] T. Aaltonen et al. (The CDF Collaboration) (2012), `1203.0742`.

[191] H. An, X. Ji, and L.-T. Wang (2012), `1202.2894`.

[192] CMS Collaboration, Tech. Rep. CMS-PAS-EXO-11-059, CERN, Geneva (2011).

[193] M. Beltran, D. Hooper, E. W. Kolb, Z. A. C. Krusberg, and T. M. P. Tait, JHEP **09**, 037 (2010), `1002.4137`.

[194] C. Rogan (2010), `1006.2727`.

[195] S. Chatrchyan et al. (CMS Collaboration) (2011), `1107.1279`.

[196] D. Alves et al. (LHC New Physics Working Group) (2011), `1105.2838`.

[197] K. Cheung, P.-Y. Tseng, Y.-L. S. Tsai, and T.-C. Yuan (2012), `1201.3402`.

[198] J. Fan, M. Reece, and L.-T. Wang, JCAP **1011**, 042 (2010), `1008.1591`.

[199] CMS, `https://cdsweb.cern.ch/record/1404167/files/SUS-11-008-pas.pdf`.

[200] Moortgat, F. and Pape, L., Tech. Rep. CERN-LHCC-2006-021, CERN, Geneva (2006).

[201] CMS, `http://cdsweb.cern.ch/record/1279615/files/EWK-10-002-pas.pdf`.

[202] J. Alwall, M. Herquet, F. Maltoni, O. Mattelaer, and T. Stelzer, JHEP **1106**, 128 (2011), `1106.0522`.

[203] J. Conway et al., *PGS—Pretty Good Simulation* (2009), `http://physics.ucdavis.edu/ conway/research/software/pgs/pgs4-general.htm`.

[204] S. Hoeche, F. Krauss, N. Lavesson, L. Lonnblad, M. Mangano, et al. (2006), `hep-ph/0602031`.

[205] J. M. Campbell, R. Ellis, and C. Williams, JHEP **1107**, 018 (2011), `1105.0020`.

[206] J. Campbell, K. Ellis, and C. Williams, *MCFM*, `http://mcfm.fnal.gov`.

[207] J. R. Ellis, K. A. Olive, and C. Savage, Phys. Rev. **D77**, 065026 (2008), `0801.3656`.

[208] R. D. Young and A. W. Thomas, Nucl. Phys. **A844**, 266C (2010), `0911.1757`.

[209] A. Friedland, M. L. Graesser, I. M. Shoemaker, and L. Vecchi (2011), `1111.5331`.

VITA

Reinard Primulando

Reinard Primulando [redacted] graduated Cum Laude from the Institut Teknologi Bandung, Indonesia in 2006 with a bachelor degree in Physics. He entered the graduate program at The College of William and Mary, Williamsburg, Virginia in August 2007. He was a Fermilab Fellow in Theoretical Physics over the 2011-2012 academic year.